Faculty of Physics and Astronomy

University of Heidelberg

Master thesis in Physics, submitted by

Axel Donath

born in Landau/Pfalz, Germany

March 2014

Towards the H.E.S.S. Galactic Plane Survey Gamma-Ray Source Catalog

This master thesis has been carried out by Axel Donath
at the Max-Planck Institut für Kernphysik in Heidelberg
under the supervision of Prof. Werner Hofmann

Abstract

This thesis deals with the creation of a catalog of Galactic gamma-ray sources using a multi-scale detection and morphology characterisation method. The analysis is based on maps of the H.E.S.S. Galactic Plane Survey (HGPS), generated from observations between 2004 and 2013. The emission of the Galactic plane is modelled with a Likelihood-Fit procedure, assuming a Gaussian source morphology. The identified shell-type supernova remnants *Vela Junior*, *HESS J1731-347* and *RX J1713.7-3946* are excluded from the analysis. Applying a detection threshold of $TS = 30$ a total number of 112 source components is obtained. The existence of large, low surface brightness emission underneath known sources is revealed. The origin of this unresolved emission is not known. Furthermore it is observed, that bright extended sources decompose into multiple components, because the morphology assumption does not match the data well enough. First a reference catalog is defined, dealing with these issues by manually classifying and merging source components, using previous H.E.S.S. publications as guidance. A total number of 78 sources in the survey region is found. For all sources the position, extension and flux with uncertainties are determined. The brightness of the sources varies between 0.7% Crab and 80% Crab. The size of the source ranges between $\sigma = 0.006^\circ$ and $\sigma = 0.64^\circ$. In a second step automatic methods are developed and examined to classify unresolved components by simple cuts in size and significance and to merge components into sources by defining a suitable overlap criterion. The reference catalog can be reproduced except for a few cases, which are discussed in detail.

Zusammenfassung

Die vorliegende Arbeit beschäftigt sich mit der Erstellung eine Katalogs von Quellen galaktischer Gammastrahlung. Als Basis dienen Karten des H.E.S.S. Galactic Plane Survey (HGPS), die aus Beobachtungen von 2004 bis 2013 generiert wurden. Die Emission der galaktischen Ebene wird unter Annahme einer Gauss'schen Quellmorphologie mit einer Likelihood-Fit Prozedur modelliert. Die identifizierten schallenförmigen Supernovaüberreste *Vela Junior*, *HESS J1731-347* and *RX J1713.7-3946* werden von der Analyse ausgeschlossen. Bei einer Detektionsgrenze von $TS = 30$ werden insgesamt 112 Quell-Komponenten erhalten. Es wird die Existenz ausgedehnter, wenig signifikanter Emission unterhalb von bekannten Quellen beobachtet. Der Ursprung dieser unaufgelösten Emission ist nicht bekannt. Darüber hinaus zeigt sich, dass helle ausgedehnte Quellen in mehrere Komponenten zerfallen. Durch manuelle Klassifizierung und Wiedervereinigung von Komponenten zu Quellen auf Basis vorheriger H.E.S.S. Publikationen, wird zunächst ein Referenzkatalog definiert. Die Gesamtzahl der Quellen in der Survey Region wird dabei auf 78 bestimmt. Davon zerfallen 13 in mehr als eine Komponente. Für alle Quellen werden Position, Größe und Fluss mit Fehlern bestimmt. Die Helligkeiten varieren zwischen 0.7% Crab und 80% Crab, die Größen liegen zwischen $\sigma = 0.006^\circ$ und $\sigma = 0.64^\circ$. In einem zweiten Schritt werden Methoden entwickelt und beurteilt, Komponenten unaufgelöster Emission durch Schnitte in Größe und Signifikanz automatisch zu klassifizieren und Komponenten durch die Definition eines Überlapp-Kriteriums wieder zu Quellen zu vereinigen. Der Referenzkatalog kann dabei bis auf wenige, im Detail diskutierte Ausnahmen reproduziert werden.

Contents

List of Figures

List of Tables

1. Introduction

The first detection of TeV gamma-rays from a Galactic object, the Crab pulsar wind nebula, with an imaging air Cherenkov telescope was made by the Whipple telescope in 1989 (Weekes et al., 1989). Since that time the ground based observation of gamma rays has been established as a field of its own in astronomy.

1.1. The Gamma-Ray Milky Way

Cosmic gamma rays have a non-thermal origin. They are mainly produced in the interaction of accelerated charged particles with ambient matter or radiation fields. Currently one assumes that mainly two processes are relevant for the production of gamma-rays. At first Inverse Compton (IC) scattering, where target photons such as microwave backround, infrared or optical photons are upscattered by relativistic electrons and secondly the decay of π_0 mesons, that are produced in pp interactions. As these processes require primary particles of very high energies, one assumes the existence of cosmic particle accelerators. One likely mechanism is the so called diffuse shock acceleration in propagating shock fronts of supernova remnants (SNR) or pulsar winds. Charged particles, such as electrons, protons or nuclei are scattered due to turbulent magnetic fields on both sides of the shock and gain energy, every time they cross diffusively the shock.

1.1.1. The H.E.S.S. Galactic Plane Survey

Most Galactic gamma-ray sources are associated with remnants of massive stars, which results in a concentration of sources along the Galactic plane. For this reason H.E.S.S. started a systematic survey of the Galactic plane in 2004 and released the first results in Aharonian et al., 2006. One of the main findings was that pulsar wind nebulae (PWN) represent a very prominent class of Galactic gamma-rays sources. Before 2004 only few Galactic sources were known, but until now the total number has grown to ≈ 70 sources. Figure 1.1 shows a recent significance map of the HGPS region, with sources detected by H.E.S.S. labeled.

Source Classes

Roughly one third of the sources in the HGPS region are identified PWN. Another third is made up of shell-type SNR, SNRs interacting with molecular clouds, binaries, stellar clusters or other objects. The last third remains unidentified up to now. Most of the Galactic sources show significant extension ranging from a radius of 0.01° up to 1°, for the largest shell type SNR and PWN. The gamma-ray emission of extended sources varies spatially across the region of the source, resulting in a diversity of source morphologies. Figure 1.2 show a few examples of the morphology of SNRs. One of the most prominent examples is *Vela Junior* with a very distinct shell type structure and a radius of $\sim 1°$.

Figure 1.3 show a few examples of the morphology of PWN in the X-ray and TeV range. With a radius of $\sim 0.5°$, *Vela X* a very prominent PWN on the TeV sky. It shows a distinct elongation and surrounding halo emission. A similar morphology is observed for the PWN *MSH 15.52* (*HESS J1514-591*), but with a smaller size of 0.14°. Another interesting case is *HESS J1420-607* and *HESS J1418-6048*, which are two small (each $\sim 0.1°$) close-by PWNs. Both PWNs show a center-filled Gaussian-like morphology. A last special case is the PWN *HESS J1825-137*, which is the largest PWN ($\sim 1°$) observed by H.E.S.S. . The PWN shows a very bright core and a lot of surrounding substructure.

Unresolved Emission

Excluding all the sources from the HGPS region a band of emission along the Galactic Plane remains, which can't be assigned to any (known) sources. It is expected that this emission band is composed of unresolved sources, which are below the sensitivity of H.E.S.S. , true (interstellar) diffuse emission or even systematics in the background estimation. The first two aspects are addressed in Egberts et al., 2013, with the conclusion that a larger fraction of this emission (less than 75%) is due to unresolved sources. The minor part is contributed by true Galactic diffuse emission, which is mainly produced by hadronic cosmic-ray interactions with the interstellar medium.

1.2. H.E.S.S. Catalog Motivation and Challenges

The HGPS has up to now accumulated approximately ten years of science data. Since the first H.E.S.S. survey paper from 2006 (Aharonian et al., 2006) the exposure has considerably increased and a good overall sensitivity across the survey region could be achieved (see Carrigan et al., 2013 for a sensitivity map). Beside the upcoming publication of the most recent HGPS dataset as high level survey maps including flux, significance etc., a catalog of Galactic gamma-ray sources will be published. Several reasons motivate the creation of this H.E.S.S. source catalog.

So far all H.E.S.S. sources have been published as single source analysis and no uniform

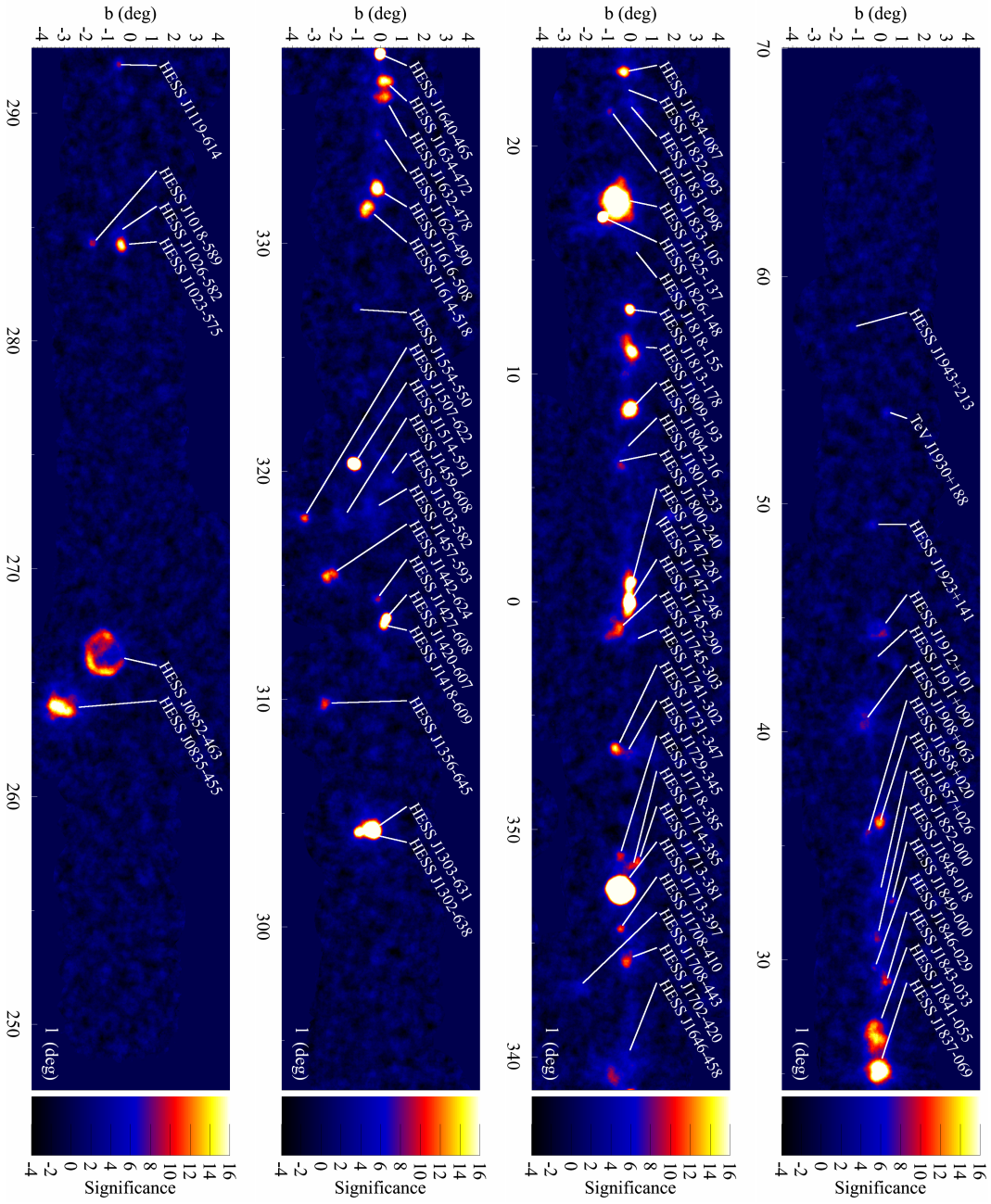

Figure 1.1.: Significance map of the H.E.S.S. Galactic Plane Survey with source labels. In total there are 70 sources. Taken from Carrigan et al., 2013.

characterisation of all Galactic H.E.S.S. sources was available. By the creation of the catalog the full dataset is re-analysed and summarized as a uniform list of Galactic TeV sources. Furthermore a few hotspots and new sources will be included in the catalog, that have not been published before. The standardized characterisation of the sources is required e.g. for subsequent population studies of PWN. A further goal for the catalog is to have an almost complete representation of the measured emission in the Galactic plane as a number of well defined sources, which may be associated to objects known from other wavelength ranges. The assignment of gamma-ray emission to sources, can be useful e.g. for the study of diffuse emission and unresolved sources using *Log N - Log S* distributions.

The creation of a source catalog mainly involves two steps: First the detection of sources and subsequently the measurement of their characteristics, mainly position, size and flux. For Galactic gamma-ray sources both steps are challenging. The first problem is the nature of the sources itself. Even if the number of gamma-ray emitting objects can be assigned to only a few object classes, the appearance of the sources is manifold. The first demand on a reliable detection of sources for the catalog is the robustness against the assumed morphology of the sources. This goes along with the ability to detect sources on many scales (in order of 0.01° to 1°). The difficulty is the correct estimation of the source's significance, which depends on the scale that is considered. For this reason a multi-scale detection approach is necessary. A further problem that is related to the extension of the sources, is source confusion. Because of the high source density in the Galactic plane, sources can be strongly overlapping. Examples are *HESS J1420-607* and *HESS J1418-609* or *HESS J1303-631* and *HESS J1302-638*. A good detection method has to be able to separate nearby sources properly. In contrast, if the ability of the method to separate sources is too strong, sources will decompose, because of substructures in their morphology. This effect showed up in early studies and was already reported in C. Deil, 2011. This decomposition of sources into several components will be one of the major issues handled in this thesis. A last challenge for the catalog of Galactic gamma-ray sources is diffuse or unresolved emission along the Galactic Plane, which can appear as significant detections on very large scales and additionally hampers the detection and estimation of source parameters of superimposed sources.

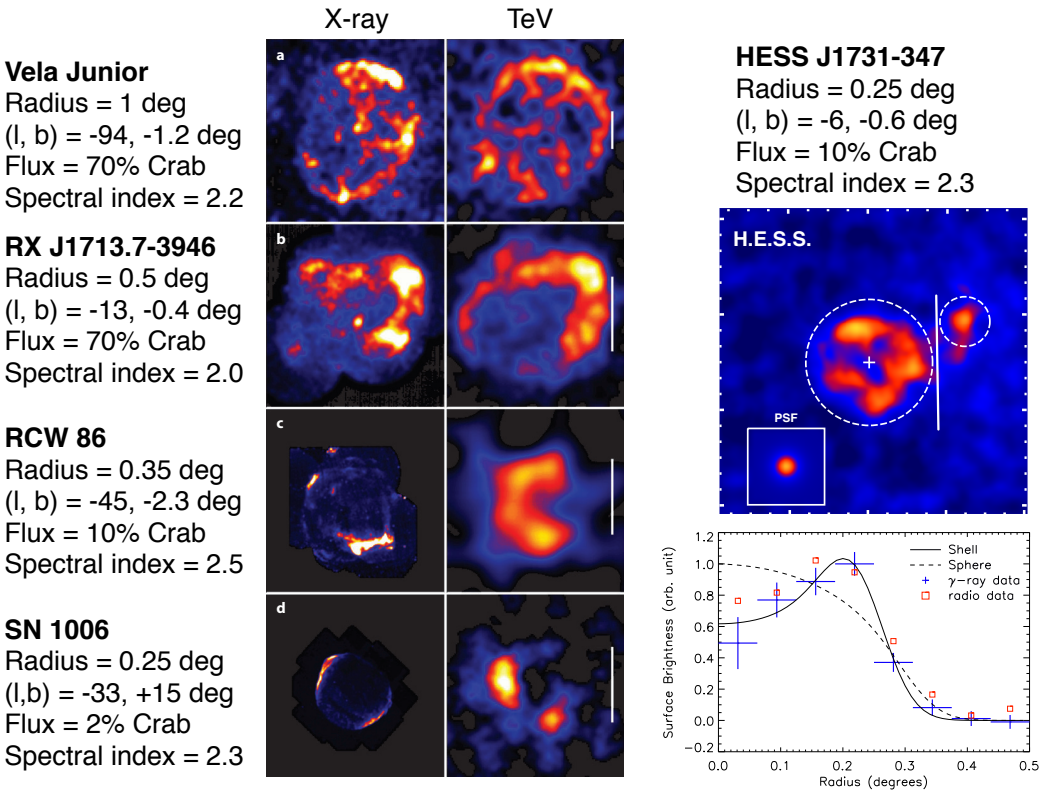

Figure 1.2.: Typical morphologies of SNRs seen by H.E.S.S. . Taken from C. Deil, 2011

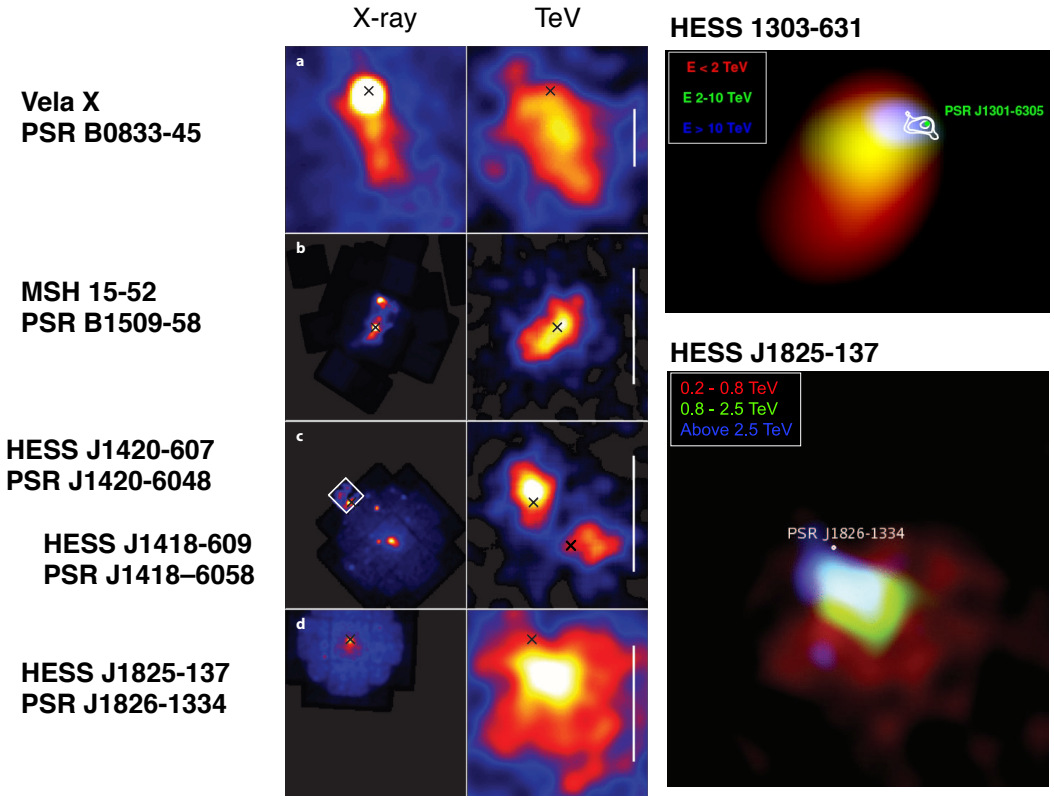

Figure 1.3.: Typical morphologies of PWNs seen by H.E.S.S. . Taken from C. Deil, 2011

2. H.E.S.S. Survey Dataset

In the first part of this chapter we will introduce the H.E.S.S. instrument and the low-level H.E.S.S. data reconstruction method. The second part is dedicated to the description of the dataset and the creation of high-level survey maps, which will be the basis for the data analysis in subsequent chapters. The last part of this chapter contains a more detailed description of the H.E.S.S. point spread function model.

2.1. The H.E.S.S. Telescope Array

The High Energy Stereoscopic System (H.E.S.S.) is an array of four imaging atmospheric Cherenkov telescopes observing the universe at the highest energies between 100 GeV and 10 TeV. The array makes use of the air Cherenkov effect: primary cosmic gamma particles enter the upper layers of the Earth's atmosphere and trigger a cascade of secondary particles, so called air showers, which in turn produce short flashes of optical Cherenkov light, that can be observed from the ground. The stereoscopic alignment of the telescopes allows to reconstruct the direction of the primary gamma particles with an accuracy of $\sim 0.1^\circ$ and the energy of the particle, which effects the shape and brightness of the shower, with an accuracy of $\sim 15\%$.

The four telescopes are placed on the corners of a square with a side length of 120 m, yielding a total effective area of $\sim 10^5$ m^2. This corresponds roughly to the area of the light cone a particle shower sheds on the ground. Each of the telescopes has an effective mirror area of ~ 108 m^2, and in the focus a Cherencov camera consisting of 960 photomultiplier tubes (PMTs). The telescope array in total has a field of view of 5° in diameter. Combined with the placement of the array in the Khomas Highland in Namibia, which assures excellent observation conditions and allows the all-year observation of the Milky Way, the instrument is well suited for survey observations of the Galactic Plane.

Since July 2012 a fifth, much larger telescope with an equivalent mirror area of 614 m^2 is in operation, which reduces the energy threshold of the overall array to a few 10 GeV. Figure 2.1 shows a picture of the five H.E.S.S. telescopes at the operation site in Namibia.

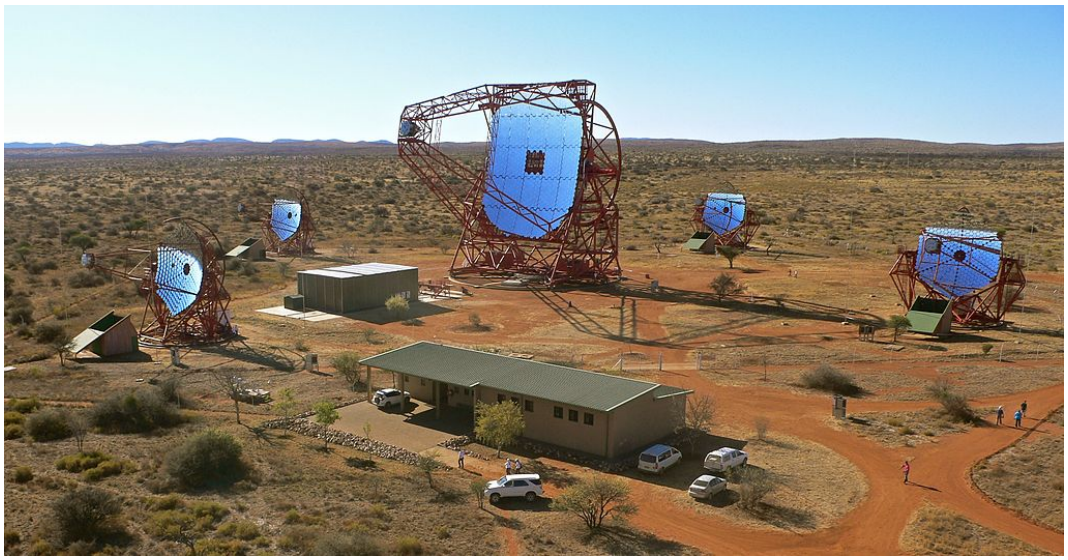

Figure 2.1.: View on the H.E.S.S. telescope array at the operation site in the Khomas Highlands in Namibia. The four 12 m H.E.S.S. I telescopes are placed on the corners of a square with side length of 120 m. In the middle the new 28 m H.E.S.S. II telescope can be seen, which is in operation since 2012. The control building is located in the foreground (Credit: H.E.S.S. Collaboration, Clementina Medina).

2.2. Description of the HGPS Dataset

The data used for the subsequent analysis and catalog production was collected with the H.E.S.S. I instrument between January 2004 and January 2013. It consists of single observations intervals of length 28 min., so called *runs*. The dataset includes all runs with observation positions between $244.5° < l < 77.5°$ and $-7.5° < b < 7.5°$. To assure reliable data quality, only runs are taken, that pass strict selection criteria e.g.: Constant trigger rate, at least 95% of the camera pixels working and no hardware errors. Runs with less than 10 min. duration and with less than 3 telescopes involved are also rejected. Details are given in C. Deil, 2011. After applying these selection cuts the dataset includes about 5700 observation runs with an overall observation time of $\sim$ 2800 h.

The runs are not distributed uniformly across the survey region, but consist of observations, made with different intentions:

(a) Scan observations of the Galactic plane, taken in different latitude bands and defined longitude ranges

(b) Follow-up observations of source candidates, discovered in scan observations

(c) Observation of astrophysical objects in the survey region, which are likely candidates

for Gamma-ray emission

For this reason the observation time across the survey region is not uniform, but shows regions of high and low exposure, yielding a position-depended sensitivity. A detailed sensitivity map is shown in Carrigan et al., 2013. Compared to the first survey dataset which was used in Aharonian et al., 2006 and included mainly the region between $300° < l < 30°$ and $-3° < b < 3°$, the observations were considerably extended.

2.3. Survey Maps

The whole survey data is stored in a set of maps, which are illustrated in Figure 2.2. The following section gives a brief description of the most important maps and more detailed information on the parameters, that were used for the production. The name in parentheses corresponds to the designation which is internally used in the H.E.S.S. collaboration and the illustration.

Counts (On) For every shower event of the observation run, the direction and energy is reconstructed and all events are binned into a sky-map, where every single pixel contains the number of events coming from this direction, respectively solid angle of the sky. To separate Gamma from hadronic background events, additional cuts are applied to the shape of the shower images. A further cut is applied to the offset of the event to the telescope's pointing axis, because the acceptance of the instrument is not well known for high offset values, here *Hard Zeta* cuts were applied. A last cut was made to the energy of the events by applying a *Safe Energy Threshold*.

Exposure (ExpGammaMap) The exposure map is computed from the time and energy integrated effective area of the H.E.S.S. instrument, weighted with the spectral distribution of events. By definition it corresponds to the expected number of counts per area, energy and time-interval:

$$\text{Exposure}(l, b) = \int\int A(E, l, b, t) \left(\frac{E}{E_0}\right)^{-\Gamma} dEdt \tag{2.1}$$

Where A is the effective area, l and b the pointing position of the telescope. The spectral distribution is assumed to be a power law with indexes between 2 and 3. For the exposure maps used in this thesis, a spectral index of $\Gamma = 2.3$ and a pivot energy of $E_0 = 1$ TeV was assumed. The exposure usually has the unit $\text{m}^2\ \text{s}^1\ \text{TeV}^1$.

Background and Off counts (Background and Off) The *Off* map is created using the adaptive ring background method. For every pixel the number of background events is estimated from a ring of fixed thickness of 0.44° outside exclusion regions. If a too large fraction of the ring is contained in an exclusion region, the ring is adaptively enlarged. The

minimal inner radius of the ring was set to 0.6°, the maximal inner radius to 1.7°. For the background estimation *STANDARD* exclusion region were used. The actual background map is given by $\alpha \cdot N_{off}$. A detailed overview of different background modelling methods in gamma-ray astronomy is given in Berge, Funk and Hinton, 2007.

Excess and Flux (Excess and SurfaceBrightness) The excess maps corresponds to the counts map, with the background subtracted. The flux map is computed from the excess and exposure by:

$$\text{Flux} = \frac{\text{Excess}}{\text{Exposure}} \tag{2.2}$$

Because of the division by the exposure, low exposure regions usually show large flux errors. The surface brightness map is computed from the flux map divided by the area of the pixel.

Significance (Significance) Significance maps are computed using the formula of Li and Ma, 1983. Therefore the counts map is correlated with a tophat filter of a given radius, where the area of the tophat filter corresponds to the *On* region. The *Off* count map is given by the ring correlated counts map, where the area of the ring corresponds to the *Off* region. Throughout this work significance maps were computed using correlation radii of 0.1°, 0.2° and 0.4°.

Alpha In order to estimate the significance, the ratio between On and Off exposure must be known. The On exposure is computed from the tophat correlated exposure map and the off exposure from the ring correlated exposure map.

All survey maps were were produced with a binning of 0.02°/Pixel and stored in the flexible image transport format (*FITS*) [1]. A copy of the WCS specification used in the *FITS*-Header is provided at beginning of Appendix C.

2.4. Point Spread Function

The angular resolution of the H.E.S.S. telescope array is approximately $\sim 0.1°$. For proper analysis of the observational data a more detailed modelling of the instrument's characteristics is required. The spatial resolution of any optical instrument can be described by its point spread function (PSF). A point source will not be imaged as a single, well defined point on the focal plane but rather as a blurred blob, with tails of decreasing brightness. This causes e.g. slightly extended sources (Where the extension is on the same scale as the PSF) to be widened out considerably, or in case of two close by sources, a confusion of the sources. The effect of the PSF on largely extended sources (About ten times the scale of the PSF) can be neglected most times, except that details of the morphology are lost. The

[1] `http://fits.gsfc.nasa.gov/fits_documentation.html`

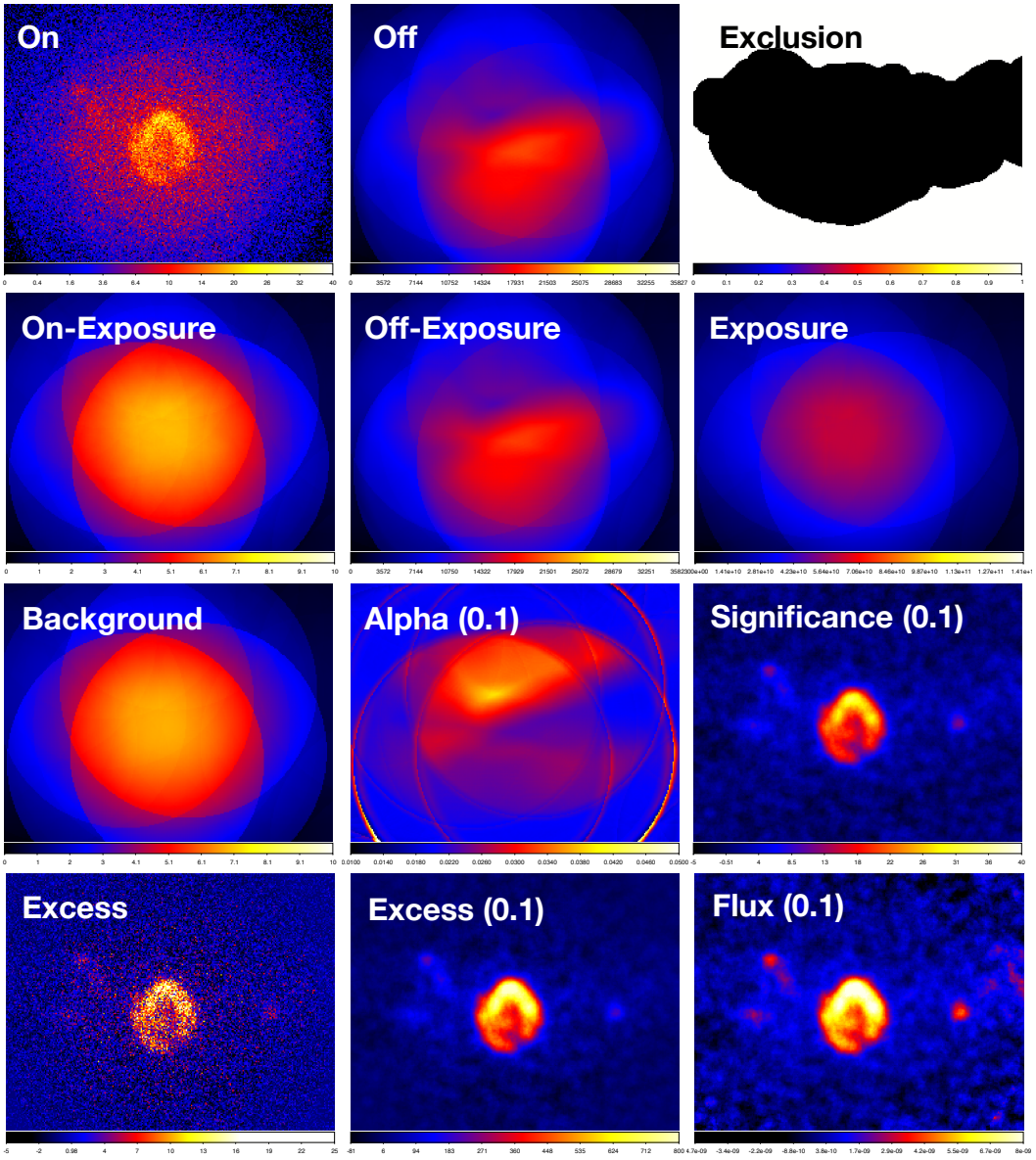

Figure 2.2.: Example survey maps types

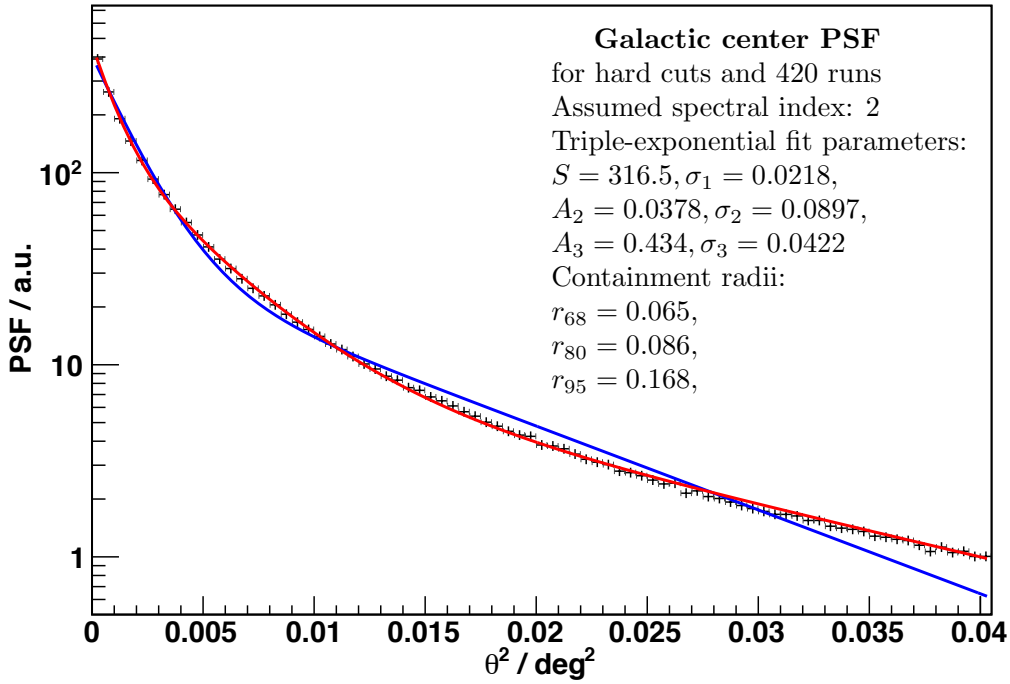

Figure 2.3.: Profile of the H.E.S.S. PSF at the Galactic center. The triple-Gaussian parametric model is shown by the red line. The corresponding parameters are given in the legend. It shows a distinct peak at the center and large tails.From C. Deil, 2011.

knowledge of the PSF is therefore an important requirement for obtaining reliable position, extension and spectra of point-like and very small sources.

The PSF of the H.E.S.S. instrument is not determined by the optical properties of the telescopes itself, but mostly determined by the uncertainty in the reconstructed direction of the particle shower events. It is determined with Monte Carlo simulation.

The radial brightness distribution of the PSF can be modelled well by the weighted sum of three Gaussian functions:

$$\frac{dP}{d\theta^2} = A_1 \exp\left(-\frac{\theta^2}{2\sigma_1^2}\right) + A_2 \exp\left(-\frac{\theta^2}{2\sigma_2^2}\right) + A_3 \exp\left(-\frac{\theta^2}{2\sigma_3^2}\right) \tag{2.3}$$

The PSF typically shows a distinct core and large tail components. It varies across the field of view by a few percent. Figure 2.3 shows the radial profile of the H.E.S.S. PSF at the galactic center with the corresponding values for the parameters A_i and σ_i.

3. Catalog Construction Methods

3.1. Existing Source Detection and Catalog Tools

In optical and X-Ray astronomy established software tools exits, which create catalogs from image data. In the following section the underlying algorithms of two of this tools shall be introduced and compared regarding to their applicability to γ-ray data.

3.1.1. SExtractor

SExtractor is a source extraction tool which is widely used in optical astronomy. Based on a multi-isophotal approach it is able to detect sources of different sizes and shapes. It also estimates position, size, ellipticity and brightness of the sources. The algorithm is described in detail in Bertin and Arnouts, 1996. Mainly it includes the following steps:

Background estimation The *SExtractor* algorithm estimates the background level locally. Therefore the image is divided into patches of size 32x32 to 128x128 pixel. Afterwards the local histogram is iteratively clipped at $\pm 3\sigma$ around the median until the result converges. If during this procedure the new σ has not changed by more than 20%, the patch is considered as uncrowded and the mean of the histogram is taken as a background estimation. This approach differs considerably from the adaptive ring background method used for the survey dataset and is not expected to deliver any reasonable results on a H.E.S.S. counts map. The main reason is that the source density in the Galactic Plane is very high and a much larger region has to be chosen for the background estimation. Furthermore instrument specific characteristics like acceptance are not taken into account.

Thresholding and Detection Given the local background estimate, the background is subtracted from the image and a detection threshold is applied. From the binary mask, defining the regions above the detection threshold, so called eight-connected pixel regions are extracted. Every extracted region is re-thresholded at 30 levels, which decomposes the region into so called *isophotals*, i.e. smaller regions which have the same surface brightness level. The structure of this decomposition is stored for every region in a binary tree, a so called *dendrogram*.

Deblending Based on the dendrogram *SExtractor* performs a *deplending* of sources by checking the flux which is contained in the subregion that belongs to one branch of the dendrogram. It the flux exceeds a certain fraction of the total flux in the whole region, the branch is considered as an own source, with the source region defined by the subregion. In order to separate two nearby or confused sources this multi isophotal technique requires a saddle point or a valley present in the surface brightness level profile between two sources. This is not necessarily given in for H.E.S.S. data.

Estimating source parameters After the deblending step a uniform segmentation of the input image is obtained, where every pixel is assigned to **one** source, source region respectively. Photometry and the estimation of source parameters is done by computing the 0th, 1st and 2nd moment of the surface brightness image in this source regions.

SExtractor offers additional functionality e.g. to separate stars from Galaxies or model fitting. But the application is limited to PSF and Galaxy Models in presence of Gaussian noise and therefore not applicable to H.E.S.S. data.

3.1.2. Wavdetect

Wavedetect is a source detection tool developed for *Chandra* X-ray data, the underlying algorithm is described in Freeman et al., 2002. The authors state that the algorithm was designed to work on low count data, which could make it suitable also for H.E.S.S. γ-ray data. The algorithm uses an wavelet transform approach, based on a *Mexican Hat* wavelet. The main steps of the algorithm shall be shortly described:

Wavelet Transformation As a first step the input image is convolved with a two dimensional *Mexican Hat* filter of increasing size. Typically a logarithmic spacing of scales is chosen, because sources shall be detected on many different scales.

Background estimation The background is estimated from the negative annulus of the wavelet function on each scale of the wavelet transform. To account for exposure variations and because other sources can be present in the background region, an iterative procedure is used. A brief comparison showed that the background estimate of *Wavedetect* on H.E.S.S. counts maps differed considerably from the background estimated with the H.E.S.S. standard ring background analysis.

Source Detection and Estimating Source Parameters Given the local background estimate on each scale, the significance of every pixel is determined from Monte Carlo lookup tables. A threshold on the significance on each scale is applied, to keep only pixels associated likely with sources. In the next step on every scale the background estimate is subtracted from the smoothed counts image, yielding an image which is widely zero, except for small

regions, where source are present. On this image peaks are detected. As peaks associated to sources are detected on many scales, an extensive selection is done across the scales, finally arriving at one single scale for every detected source. The connected region, which is larger than zero around the corresponding peak, is defined as the source region. The source parameters are estimated by computing the 0th, 1st and 2nd moment of the unsmoothed counts image in the defined source region.

Figure 3.1 illustrates the result of both source detection tools applied to a counts map of the region around *HESS J1825-137*. The bright sources are detected qualitatively correct, but both tools missed the source *HESS J1818-154*, which is most likely due to their method of background estimation. Lowering the detection threshold led to unstable detections and triggering on noise. The defined source regions are different for both tools, leading to different estimates of the source size and position. The source extension found by *SExtractor* for *HESS J1825-137* is considerably elongated towards *HESS J1826-148*, indicating that both source are not separated very well and parts of the emission from *HESS J1826-148* are assigned to *HESS J1825-137*. As the tools directly estimate the source size from the counts map, no PSF effects are taken into account. *Wavdetect* can correct for this, if an image of the PSF is provided.

3.1.3. Image-based Characterization of Sources

The catalog tools described in the previous section obtain brightness, position and extension of the source by computing the 0th, 1st and 2nd moment of the input map in a well defined source region. Assuming we have flux map f and source region, which is defined by a mask $\mathcal{S}$, we have the following formulae:

0th Moment, Total flux

The total flux of the source is given by the sum of all pixels contained in the source region:

$$F_\Sigma = \sum_{i,j \in \mathcal{S}} f_{ij} \tag{3.1}$$

If a background model or estimate is available it has to subtracted first.

1st Moment, Position

The x_Σ and y_Σ position of the source is computed by weighting the pixel value, with pixel position x_{ij} and y_{ij}:

$$x_\Sigma = \frac{1}{F_\Sigma} \sum_{i,j \in \mathcal{S}} x_{ij} f_{ij} \qquad \text{and} \qquad y_\Sigma = \frac{1}{F_\Sigma} \sum_{i,j \in \mathcal{S}} y_{ij} f_{ij} \tag{3.2}$$

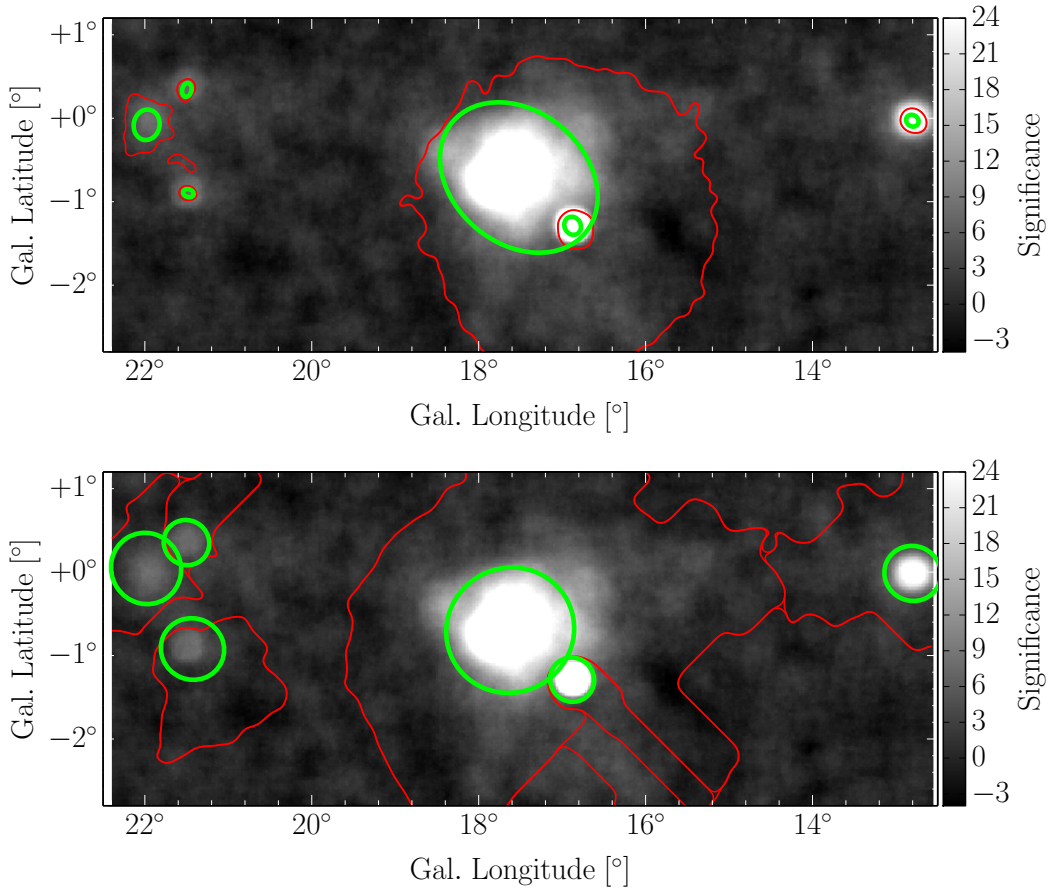

Figure 3.1.: Example detection results of *SExtractor* and *Wavdetect* on the Region around *HESS J1825-137*. Detected source extension and position, which are computed from the 1st and 2nd moment of the excess map in the source region, are marked with green ellipses. The corresponding source region is drawn as a red contour around. The bright sources are detected qualitatively correct, but both tools missed the source *HESS J1818-154* to the upper right of *HESS J1825-137*.

It is important to take care of the different pixel position conventions and whether the pixel value is given at the center or the corner of a pixel, which may introduce a shift by half a pixel.

2nd Moment, Extension

The extension is determined by computing the second moment in the source region.

$$\sigma^2_{\Sigma,x} = \frac{1}{F_\Sigma} \sum_{i,j \in \mathcal{S}} (x_{ij} - x_\Sigma)^2 f_{ij} \qquad \text{and} \qquad \sigma^2_{\Sigma,y} = \frac{1}{F_\Sigma} \sum_{i,j \in \mathcal{S}} (y_{ij} - y_\Sigma)^2 f_{ij} \tag{3.3}$$

As the source properties are computed on an image base it is in general quite complex to estimate uncertainties on this quantities.

3.2. The H.E.S.S. Catalog Pipeline

As outlined in the previous section it is not expected to get reliable results from already existing, image processing based, software tools. The main issues that limit the application to H.E.S.S. data are the background estimation and the fact that these tools deliver a uniform segmentation of the input image, where every pixel is assigned to only one single source. As sources in the HGPS survey region are extended and partly strongly overlapping, a parametric modelling approach will be chosen to create the H.E.S.S. catalog. In the first section the statistical background for proper modelling of low counts data shall be presented, followed by the description of the software pipeline, which was used for the subsequent modelling.

3.2.1. Statistics

Significance

An ideal particle detector which points to a region at the sky, where a source is expected (the so called *On* region), will count a certain number of events N_{On}. In order to estimate the number of background events, a close region where no source is expected is selected (the so called *Off* region) and the number of events N_{Off} in this region is counted. To account for different exposure times or instrument related differences in sensitivity, the ratio of exposures $\mathcal{E}_{On}$ and $\mathcal{E}_{Off}$ is defined:

$$\alpha = \frac{\mathcal{E}_{On}}{\mathcal{E}_{Off}} \tag{3.4}$$

Using the method of a likelihood ratio test Li and Ma, 1983 derived a formula to correctly estimate significance for such a setup, which is valid also in the low counts regime:

$$S = \sqrt{2}\left\{N_{On}\ln\left[\frac{1+\alpha}{\alpha}\left(\frac{N_{On}}{N_{On}+N_{Off}}\right)\right] + N_{Off}\ln\left[(1+\alpha)\left(\frac{N_{Off}}{N_{On}+N_{Off}}\right)\right]\right\}^{1/2} \tag{3.5}$$

In the limit $\alpha \to 0$, i.e. if the *Off* exposure time is much larger than the *On* exposure time, the background level is known and the formula simplifies to

$$S = \sqrt{2}\left[N_{On}\ln\left(\frac{N_{On}}{n_B}\right) - N_{On} + n_B\right]^{1/2} \tag{3.6}$$

with known background level $n_B = \alpha N_{Off}$. This formula will be used throughout this work to estimate model and model residual significances, where the model residual significance can be determined by including the model of sources in the background estimation. The effect of neglecting background fluctuations is briefly discussed in Section 3.2.3.

Poisson Maximum Likelihood Fitting

For the modelling of the survey data a binned Poisson maximum likelihood procedure will be used, which is based on Cash, 1979. Given a set of binned real measured values D_i of counts, the likelihood that the data is described by a model M is described by the product of the Poisson likelihoods per bin:

$$\mathcal{L} = \prod_i \frac{M_i^{D_i}}{D_i!}\exp(-M_i) \tag{3.7}$$

Where the model counts M_i consists of signal and background events $M_i = B_i + S_i$ in a each bin i. In order to fit the model to the data, this likelihood must be maximised. Therefore the logarithm of Equation 3.7 is taken, the sign is changed and the factorial term is dropped, because it remains constant during the fit to the same dataset. Multiplying by a factor of 2 the so-called *Cash statistic* is obtained:

$$\mathcal{C} = 2\sum_i [M_i - D_i \log M_i] \tag{3.8}$$

The *Cash statistic* was used throughout this work. The significance of a single component, which is part of more complex model, can be estimated using the so called TS value. It can be defined in two ways:

- Difference in test statistic between the model component C only and the null hypothesis model (hadronic background only): $TS_0 = \mathcal{C}_C - \mathcal{C}_0$
- Difference in test statistic between the complete model M and the component C removed from the model: $TS = \mathcal{C}_M - \mathcal{C}_{M-C}$

In the latter case all individual TS values of components add up to the total TS of the model. In case of non-overlapping source components, both TS values are the same. TS will be later used as the main source detection criterion.

The TS value can be approximately related to the classical significance value S:

$$S \approx \sqrt{\mathrm{TS}} \tag{3.9}$$

3.2.2. Software

The fitting pipeline uses the *Sherpa* modelling and fitting package (Freeman et al., 2011) and was implemented as part of C. Deil, 2011. It consists of several command-line tools, whose functionality shall be shortly described:

- `morph_cutout`: Takes a text file (`roi.reg`) as input, which specifies the region of interest (ROI) according to the ds9 region file format [1]. It cuts out the ROI region from the counts, exposure and background survey maps. Additionally the significance maps on the 0.1, 0.2 and 0.4 are cut out, which serve as a guidance for the definition of starting values for the fit. The cut out survey maps are stored in the `FITS` file format.

- `morph_pre`: Takes an input configuration file (`input.cfg`), where the model type and starting values for the fit are defined in world coordinates. The world coordinates are converted to pixel coordinates using a `WCS` transformation, which is set up according to the information in the header of the `exposure.fits` file. The converted input parameters are stored in `input_sherpa.cfg`. Additionally the tool looks up the PSF information at the position of the first source in the `input.cfg` file and stores the parameters (width and amplitude) for the triple Gaussian PSF model in a `psf.json` file.

- `morph_fit -scf`: Given the model definition and starting values in `input_sherpa.cfg` the tool performs a Poisson maximum likelihood fit to the data. Additionally with the option `-c` the covariance matrix of the fit parameters is computed. With the option `-s` images of the best fit model are saved (including PSF convolution) which are needed for the subsequent `morph_overlap` step. The fit results are stored with additional information about test statistics and covariance in a `fit.json` file.

- `morph_post -ctfi`: Given the information in the `fit.json` file, the tool converts the fit results back into world coordinates and stores the values in a `fit.cfg` file. With the `-t` option the containment radii R_{50}, R_{80} and R_{90} are computed and stored in `theta.cfg`. With the `-f` option residual significance images are computed with 0.1° , 0.2° and 0.4° correlation radii and stored in the `FITS` format. Additionally with the `-i` option, image files of significance and residual significance can be produced in `PNG` od `PDF` format.

[1] `http://ds9.si.edu/doc/ref/region.html`

Additionally the following helper tools are available:

- `morph_ts`: Compute and compare TS values for all available models of an ROI. It determines the difference in total TS to the best solution (highest value of the test statistics) with one component less.
- `morph_overlap`: Computes the pairwise overlap Q-factor and contamination of the components in the ROI. The values are stored in the `overlap.json` file. Details on how this values are computed are given in Section 5.3.
- `morph_gather`: Collect information of all ROIs and ROI models in three `FITS` tables:
  - `HGPS_MORPH_ROI.fits` contains the information about the defined ROIs e.g. position and size.
  - `HGPS_MORPH_Solution.fits` contains all the information about the available ROI models.
  - `HGPS_MORPH_Sources.fits` contains all the information about the source an source components, like best-fit position, size, flux and TS value.
- `morph_scatter`: Scatter all information from the summary `FITS` files to set up the folder structure and input configuration files for ROIs and ROI models, that the analysis can be run again e.g. on different input maps.

3.2.3. Known Caveats

During the work on this thesis it was revealed that due to a bug in the current version of *Sherpa(4.6)* no integration over pixels can be used. The bug was officially confirmed by the *Sherpa* developers[2].

To illustrate why not integrating the source model during the evaluation of the fit statistic can lead to a bias of the size of small sources Figure 3.2 was made. It shows the fraction of the total flux that is contained in every pixel for a Gaussian of width $\sigma = 0.5$ pixel (Corresponding to a width of 0.01° for data with binning 0.02°pixel) with and without integration over pixels. On the right the flux distribution is shown, when the Gaussian model is integrated over the area of the pixel. The central pixel contains 47% of the total flux, the remaining flux is distributed in the eight surrounding pixels. All pixels sum up to 100%. On the left the flux distribution is shown, when the Gaussian function is only evaluated at the center of the pixel. Now 64% of the total flux is contained in the center pixel and considerably less flux is assigned to the surrounding pixels. The Gaussian appears smaller by $\approx$ 20%. This overestimation of the size of small sources was observed, when checking the pipeline results on simulated sources (See Section 4.2.2). All pixels sum up to 103%, which can lead to a slight, but most likely negligible underestimation of the flux.

[2] `http://cxc.harvard.edu/sherpa/bugs/`

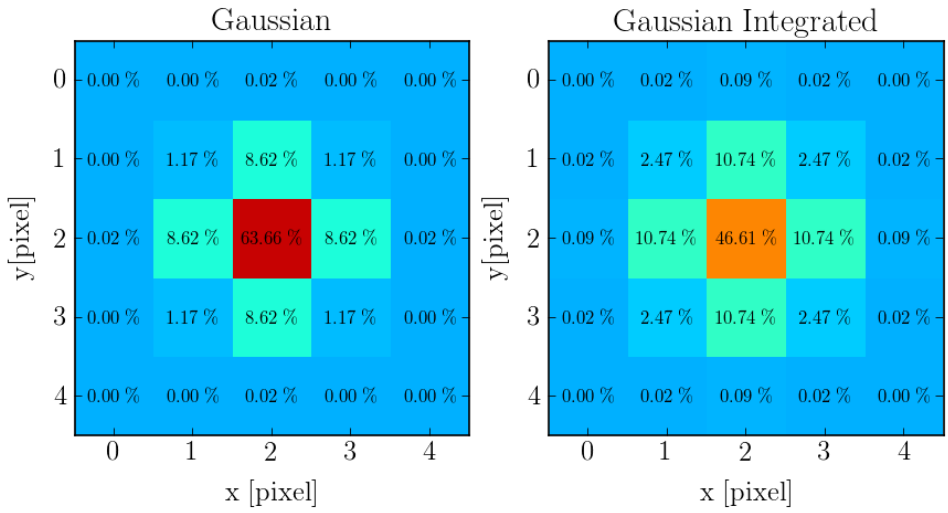

Figure 3.2.: Flux distribution of a Gaussian with and without pixel integration for Gaussian of width $\sigma = 0.5$ pixel discretized on a 5x5 grid. On the right the flux distribution is shown, when the Gaussian model is integrated over the area of the pixel. The central pixel contains 47% of the total flux, the remaining flux is distributed in the eight surrounding pixels. All pixels sum up to 100%. On the left the flux distribution is shown, when the Gaussian function is evaluated at the center of the pixel. Now 64% of the total flux is contained in the center pixel and considerably less flux is assigned to the surrounding pixels. The Gaussian appears smaller by $\approx 20\%$ and all pixels sum up to 103%.

Which was also observed in Section 4.2.2.

A further caveat in the software is that only the *Cash* statistics is available for fitting, which neglects fluctuations in the background. The assumption of a known background can only be made, when the *On* exposure time is much larger than the *Off* exposure time, which is not fulfilled for large sources. The effect is an overestimation of the significance of large sources. To account properly for background fluctuations in the fit, a different fit statistic, namely the *wstat*[3] fit statistic has to be used, but this would require pixel-wise non correlated background modelling.

[3] `http://heasarc.nasa.gov/xanadu/xspec/manual/XSappendixStatistics.html`

4. Multi-Gauss Representation of the Survey Excess

One of the motivations creating the catalog was to reach a uniform representation of the entire survey excess as a collection of sources. Such a uniform analysis shall be presented in the following chapter.

4.1. Method

4.1.1. General Morphology Assumption

As outlined in the introduction most of the Galactic H.E.S.S. sources show significant extension and various morphologies. Even if more complex source morphology models could have been used, e.g. elongated models or uniform shell-type models for some SNRs, the assumption of a Gaussian morphology model was made. The main reason for this restriction was, that in previous studies other morphology assumptions proved to be unstable during the fitting process because of the larger number of free and possibly badly constrained parameters. Also the amount of work would be considerably increased, as for every source many different morphology models would have to be tested. Furthermore the Gaussian morphology assumption allows to compute certain quantities analytically, e.g. convolution with the PSF and parameters of merged sources (see Section B). A last argument in favour of the Gaussian model is that many Galactic H.E.S.S. sources show at least a Gaussian-like morphology. The bias which is introduced by the Gaussian morphology assumption was investigated in detail in an own study presented in Appendix A.

The surface brightness of the Gaussian morphology model is described by:

$$f(r) = F\frac{1}{2\pi\sigma^2}\exp\left(-\frac{r^2}{2\sigma^2}\right) \tag{4.1}$$

Where $r^2 = (x - x_0)^2 + (y - y_0)^2$ and x_0 and y_0 denote the position of the source (source component) in Galactic longitude and latitude, F the total integrated flux and σ the size of the source. The 80% containment radius for the symmetric Gaussian model is related to its width by $R_{80} = \sigma\sqrt{2\log(5)} \approx 1.8\sigma$.

4.1.2. Defining Regions of Interest

First the whole Galactic plane survey region was divided into regions of interest, so called ROIs. This is mainly necessary to limit the number of simultaneous fitted parameters and the number of pixels involved in the fit. Given the Gaussian morphology assumption, with the four parameters F, σ, x, and y and a total number of ≈ 70 sources, the total number of parameters to fit is ≈ 300. This large number of free parameters would not yield any stable and reliable fit results in a reasonable time. Figure 4.1 shows the boundaries of the 18 finally defined ROIs.

The 18 ROIs were selected manually according to the following criteria:

(a) Every significant emission in the survey region above 5σ should be contained in at least one ROI

(b) Every ROI should not contain any significant emission at the edges of the ROI

(c) The width of every ROI should not exceed $6^\circ - 10^\circ$ to limit the number of pixels involved in the fit

(d) Every ROI should cover the full survey latitude range of -5° to 5°

Assumption (a) assures that every source or source candidate is at least contained in one ROI. Assumption (b) assures that all the significant emission is fully enclosed in the ROI, to prevent boundary effects. If this was not possible to fulfil, the corresponding emission was excluded from the fit data and assigned to a different, overlapping ROI. Assumption (c) limits the total number of pixels and of the fitted parameters to keep the time, that is needed for the fit, in the order of a few minutes. The ROI names were defined according to the scheme *GLON_LLL.ll*, where *LLL.ll* denotes the Galactic longitude of the center of the ROI.

Table D.1 (p. 76) shows an overview with the sizes and positions of the ROIs. Additionally for every ROI the maximal significance value in a small stripe of width 0.1° from the ROI boundary is given on the 0.1°, 0.2° and 0.4° scale. For most ROIs the maximum is well below 5σ. For *GLON_008.5*, *GLON_022* and *GLON_026* there is significant emission on the 0.4° scale, which is most likely unresolved emission along the Galactic plane, which becomes significant for large correlation radii.

Shell Type Supernova Remnants

The H.E.S.S. survey region contains three identified shell-type SNRs: *Vela Junior*, *HESS J1731-347* and *RX 1713.7-3946*. As the morphology of these objects is very complex, with a distinct shell structure, these SNRs were excluded from the data and not modelled. Table 4.1 shows the corresponding parameters of the cut out regions.

SNR Name	$l[^\circ]$	$b[^\circ]$	Radius $[^\circ]$
Vela Junior	266.284	−1.241	1.3
RX 1713.7-3946	347.336	−0.473	0.9
HESS J1731-347	353.565	−0.622	0.4

Table 4.1.: Centre and radius of exclusion circles of the three cut out shell-type SNRs.

4.1.3. Fitting procedure

Every ROI was fitted with a combined maximum likelihood procedure (see Section 3.2.1 for details) according to the following model:

$$\boxed{\text{Counts} = \text{Background} + \text{PSF}(\text{Sources} \cdot \text{Exposure})} \tag{4.2}$$

Where *sources* is given by a sum of Gaussian components. Counts, Background and Exposure are given by the standard survey maps described in Section 2.3. The PSF was assumed to be constant across the ROI and modelled by the sum of three Gaussian functions (see for 2.4 for details). The parameters for the PSF were taken at the the position of the brightest source in the ROI. Table D.1 (p.76) also lists the containment radii R_{68} and R_{95} of the PSF per ROI.

The whole fitting process was conducted manually. As starting point every ROI was modelled with one component, regardless of the number of actual sources in this ROI. After the fit successfully converged the residual significance map of the ROI was computed with 0.1°, 0.2° and 0.4° correlation radius. The residual significance was determined using formula 3.6 and including already modelled emission in the background model.

At the position of maximal significance a new Gaussian component was added to the model. The width of this component was chosen similar to the correlation radius of the residual significance, where the maximum was found. The model with the new added Gaussian component was fitted again to the data. If the fit did not converge different starting values were tested. If the fit converged, the difference in test statistics to the best model with one component less was computed. If the difference was larger than $TS = 25$ the new component was considered as significant an kept. If the TS difference was smaller than $TS = 25$ a different position and/or starting values for flux and extension were tested. If no new significant component was found the modelling was stopped. The actual challenge of this procedure, consists in testing many different starting values and finding the global best solution of the fit. In many ROIs it was observed that the fit routine was stuck in local minima and by slightly changing the starting values different results were obtained.

This way for every ROI a set of solutions with increasing number of components was obtained. The total number of components was up to 14 in complex regions (e.g Galactic Center). Figure 4.2 illustrates the procedure on an example region modelled with two and three components. The two-component solution shows large residuals of non-modelled emission, whereas the residuals of the three-component solution appear quite flat.

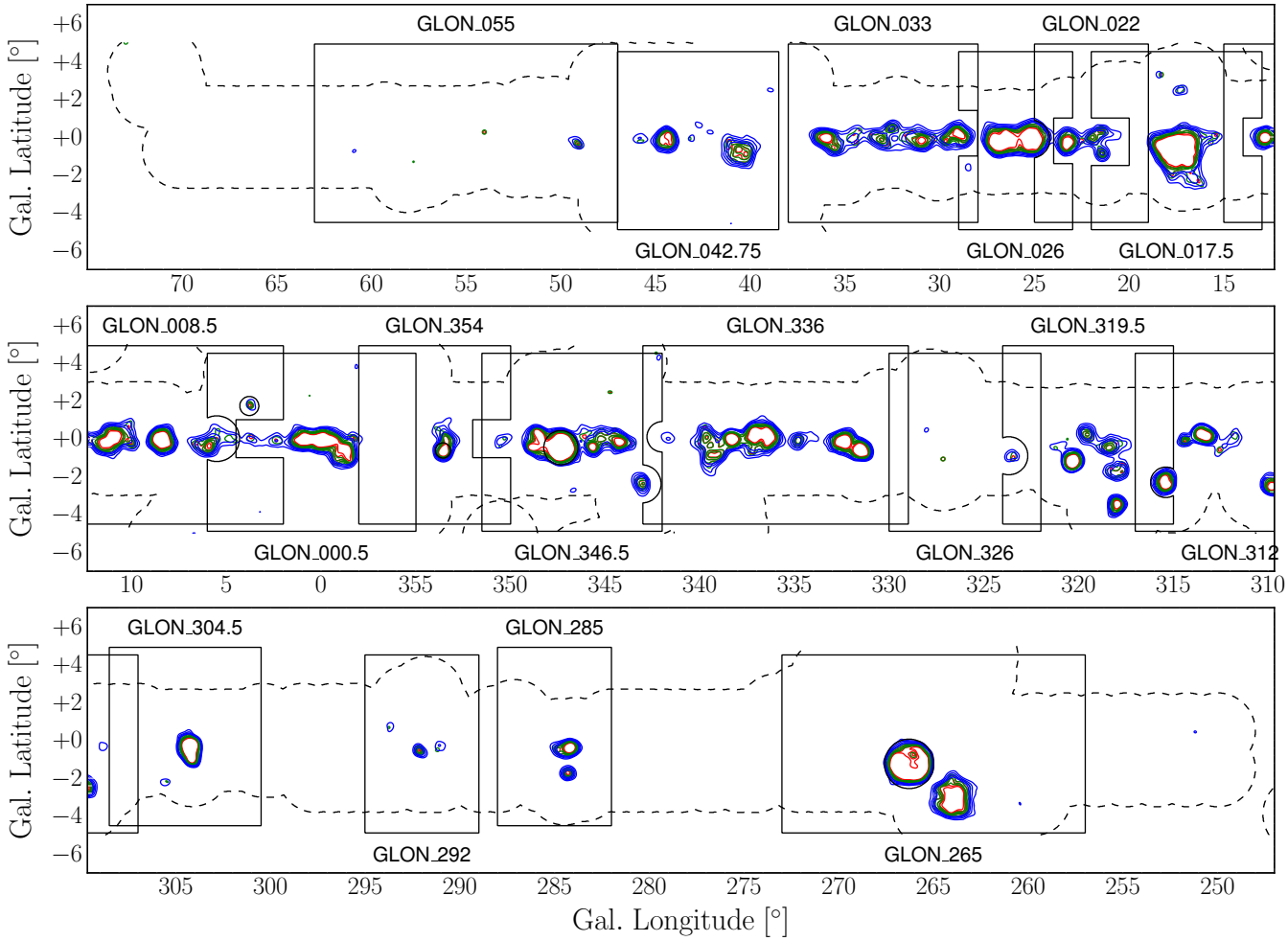

Figure 4.1.: Position and sizes of the 18 defined regions of interest (ROI) for the HGPS survey region. Significance contours are shown on a 3σ, 4σ, 5σ and 6σ level. The colors correspond to the different correlation radii of 0.1° (red), 0.2° (green) and 0.4° (blue). To better distinguish the ROI boundaries they are artificially alternately enlarged to higher and lower latitudes. They are defined to cover the full survey latitude range of b= $-5°$ to b= 5° .

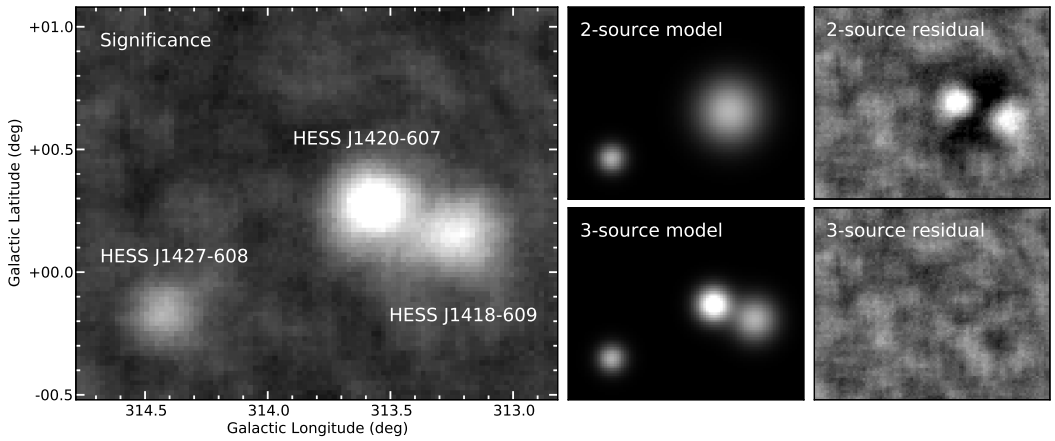

Figure 4.2.: Example residuals of a ROI fitted with two or three Gaussian components. The two-component solution shows large residuals of unmodelled emission, whereas the three-component solution provides a better representation of the emission. From Carrigan et al., 2013.

4.2. Results

The previously described procedure was applied to each of the 18 ROIs. Even if ROIs were modelled down to $TS = 25$ a more conservative detection threshold of $TS = 30$ was applied for the creation of the component list, limiting the number of expected false detections in the whole survey region to one. The total number of found Gaussian components was 112. A Gaussian component either models a whole source, unresolved emission or a part of the morphology of a larger source. All components were named according to the following scheme, which follows the specifications of the international astronomical union IAU [1]

$$\text{HGPSC JHHMM.m} + \text{DDMM.m}$$

Were JHHMM.m denotes the right ascension and DDMM.m the declination of the Gaussian component. In order to avoid duplicate component names it was necessary to specify five digits of right ascension and declination.

As a first overview Table D.2 (p. 77) shows the number of components per ROI and the ratio of the modelled and real excess in the ROI. The ROIs which were modelled with more than 10 components are known to be crowded and complex regions. Among them the Galactic Center (*GLON_000.5*) and the ROI containing *Westerlund 1* (*GLON_336*). In most cases the modelled excess only differs about a few percent from the real excess. The variations are due to deviations from the morphology assumption, random count fluctuations and non-significant unresolved emission along the Galactic plane.

There are two ROIs, where the difference between real and modelled excess is quite sig-

[1] `http://cdsweb.u-strasbg.fr/Dic/iau-spec.html`

nificant. The first one is *GLON_055* where only 26% of the total excess is modelled. This can be explained by the fact that *GLON_055* is the most extended ROI in the survey, but contains only three weak sources in it. Most part of the excess is diffuse and not significant emission (on small scales) and was therefore not modelled. The second ROI with large differences between real and modelled excess is *GLON_326*. Again the ROI only contains two very weak sources and the remaining excess is large scale, not significant emission. Additionally the total real excess in this region is negative, which implies an overestimation of the background in large parts of the ROI.

As a second check the model significances in every ROI were computed. Based on the best-fit model a model flux map was created, which was multiplied with the exposure. The model count map was obtained adding the background estimation to the model excess map. The model significance map was then computed using formula 3.6 with correlation radii of 0.1°, 0.2° and 0.4°. For the check the maximum of the significance in a stripe of 0.1° from the ROI boundary was determined on every scale. All maximal significances are well below 5σ. No significant emission at the edges of the ROIs was modelled.

Figure 4.3 shows the $\sqrt{TS}$ distribution of all the components that were obtained. The five highly significant components with $\sqrt{TS} > 40$ are the Galactic Center source (*HGPSC 1745.6-2900.5*), the main component of *HESS J1825-137* (*HGPSC 1825.4-1350.0*), the binary LS 5039 (*HGPSC J1826.2-1451.1*), the PWN *HGPSC 1303.1-6311.2* and the PWN candidate (*HGPSC 1837.3-0657.2*). Twelve components were found between $TS = 30$ and $TS = 40$.

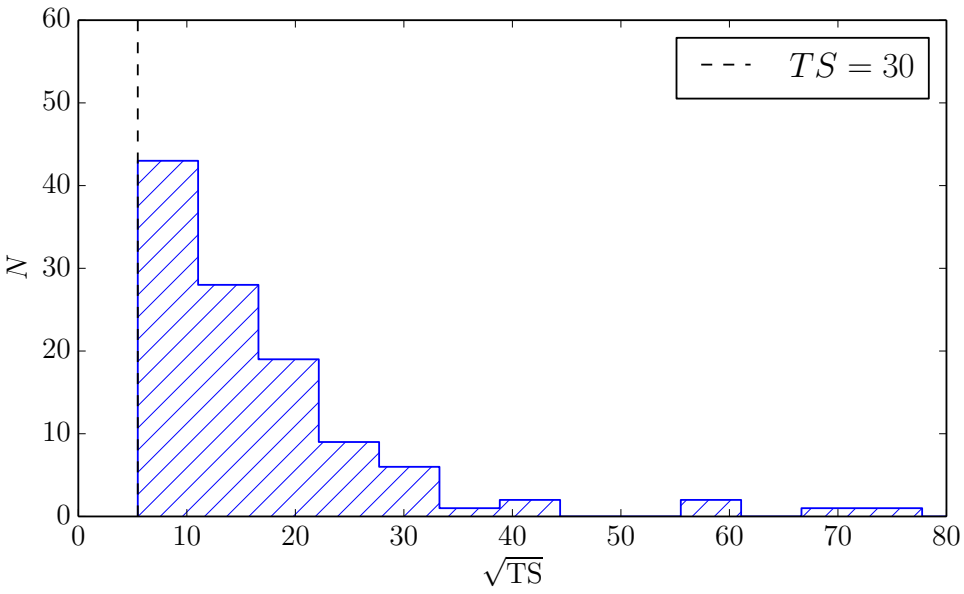

Figure 4.3.: $\sqrt{TS}$ Distribution of source components

4.2.1. Survey Model and Residual Significance Maps

Based on the list of components a survey model excess map was computed, which is shown in Figure C.1. The colors are shown on a square root scale to enhance structure. The transition from blue to red is at 1Count/Pixel. One can see that the morphology of the sources is modelled with great accuracy, e.g. the Galactic Center region with the large scale emission, or Vela X, where the elongation can clearly be recognised. It is noticeable that many source have underlying, large and weak components, which will be addressed in Section 5.2.

By including the excess model map in the background model, the residual significance map was determined using formula (3.5). The residual significance contour map is shown in Figure C.2. Almost no significant features above the 5σ level can be found. The residual significance maps for the $0.1°$ $0.2°$ and $0.4°$ scale are shown in Appendix B. Taking a look at Figure 4.4 confirms that there there is not much significant emission left. The distribution is broadened on the right side, indicating some not modelled emission which is part of complex ROIs or part of sources deviating from the morphology assumption which did not decompose into multiple components.

4.2.2. Checks

Position Check of Known Point-Like Sources

The survey region contains three bright point-like, whose counterparts and thus their locations are known very precisely. Table 4.2 lists the associated catalog components and reference positions, which were taken from the *Simbad* [2] online database. In case of the Galactic Center the association is most likely to be *Sgr A**. The deviation from the reference positions are shown in Figure 4.5. No systematic shift of the positions can be observed. *Sgr A** agrees well within the quoted errors to the reference position. *LS 5039* is shifted by $0.005°$ and shows a significantly larger error in Galactic latitude. This is most likely due to the correlation with another nearby component. *PSR B1259-63* is shifted by $-0.01°$ in latitude, which corresponds to 0.5 pixels, given the binning of $0.02°$/pixel. As the total source region, including *HESS J1303-631* in the north is modelled by four components, the shift could be caused by other nearby components, which model small parts of the emission of *PSR B1259-63*. Nevertheless all shift in position agree with the systematic error of the instrument.

Recovery of Source Parameters

As a further check the recovery of the parameters of simulated test sources was checked. For this purpose a Gaussian model source with known flux and extension was set up at the

[2] `http://simbad.u-strasbg.fr/simbad/`

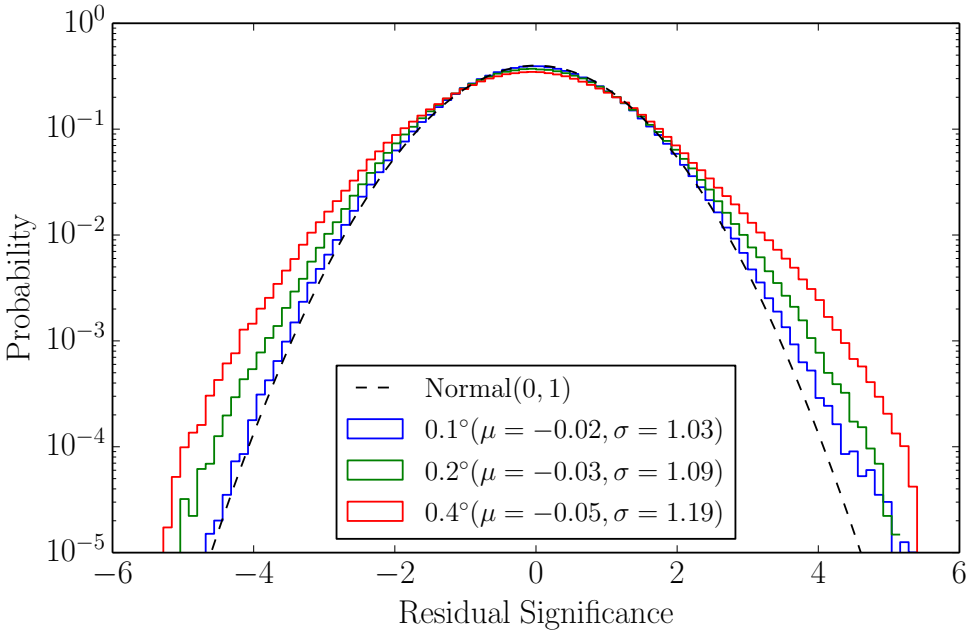

Figure 4.4.: Residual significance distribution of the survey excess model. The residual significance was computed with three different correlation radii 0.1° (blue), 0.2° (green) and 0.4° (red). The distribution is very close to the standard normal distribution (black dashed), which assures that no significant excess was left out and that the survey model is accurate. The broadening of the distribution on the right tail is due to non- modelled emission in complex regions. This can also be seen on Figure C.2.

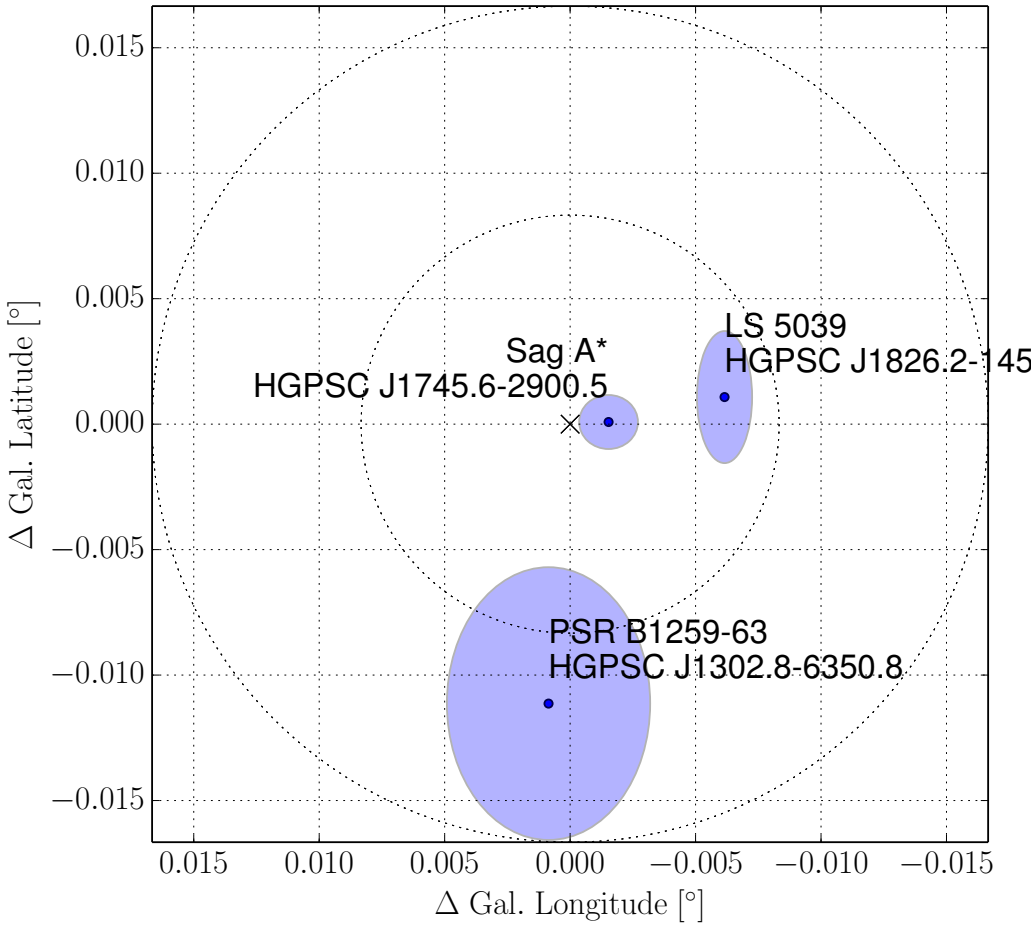

Figure 4.5.: Difference in position of associated catalog components to known Galactic point like sources. The inner dashed circle marks a radius of 30″, which corresponds approximately to the systematic position error of the H.E.S.S. instrument. The blue ellipses show the error on the position of the catalog components projected on the coordinate axis. *Sgr A** agrees well with the reference position. *LS 5039* is shifted by 0.005° and shows a significantly larger error in Galactic latitude. This is most likely due to the correlation with another nearby component. *PSR B1259-63* is shifted significantly by −0.01° in latitude, which corresponds to 0.5 pixels, given the binning of 0.02°/pixel. As the total source region, including *HESS J1303-631* in the north is modelled by four components, the shift could be caused by other nearby components, which model small parts of the emission of *PSR B1259-63*. All deviations from the reference position agree with the systematic error of the H.E.S.S. instrument.

Name	H.E.S.S. Name	l [°]	b [°]	Ra [°]	Dec [°]
Sgr A*	HGPSC J1745.6-2900.5	359.944	−0.046	266.417	−29.008
LS 5039	HGPSC J1826.2-1451.1	16.882	−1.289	276.563	−14.848
PSR B1259-63	HGPSC J1302.8-6350.8	304.190	−0.961	195.699	−63.836

Table 4.2.: Name and reference position of point-like sources in the survey used for the checks of component positions.

position of the Galactic Center. The model flux map was obtained by evaluating the model on a 0.02°pixel grid with ten times oversampling to assure flux conservation, even for sources with small extension. The model map was than multiplied with real H.E.S.S. exposure map of the Galactic Center region and convolved with the H.E.S.S. PSF model, as described in Section 2.4. Finally Poissonian noise was added to simulate a real measurement.

First the flux of the fake source was varied in 10 logarithmic steps between 1% Crab and 100% Crab. This was done for three different sizes $\sigma = 0.01°$, $\sigma = 0.1°$, and $\sigma = 1°$ of the source. In total $N = 1000$ count maps were faked and fitted with pipeline. The mean and standard deviation of the fitted source parameters were computed and plotted against the real flux values. Figure 4.8 shows the result. For any value of the flux and independently of size the flux was recovered properly. No bias or deviation was observed. The error on the recovered flux increases with decreasing flux. The points for $\sigma = 1°$ and $F < 3\%$ Crab show unstable results, because the surface brightness is below the sensitivity limit of H.E.S.S. .

In a second test the size of the source was varied in ten logarithmic steps between $\sigma = 0.01°$ and $\sigma = 1°$. For the flux 1% Crab, 10% Crab and 100% Crab were assumed. Figure 4.6 shows the recovered values vs. the real values. For larger source sizes $\sigma > 0.03°$ the recovered values correspond well to the real ones. For smaller source sizes $\sigma < 0.03°$ and point-like sources a bias can be observed: The size is overestimated. This effect is due to the 0.02°pixel binning of the survey maps and the fact the fitted source model is not integrated over pixels during evaluation of the fit statistics.

As a further check the study was repeated with a binning of the data of 0.01°/pixel. Figure 4.7 shows the resulting curve. The bias was shifted to even smaller source sizes and should be negligible now. In order to obtain correct values for the extension of small ($\sigma < 0.03°$) sources, a map binning of 0.01°pixel or integration over pixel should be used in future versions of the catalog.

4.2.3. Manual and Computational Effort

To finally arrive at an accurate set of ROI models for the survey excess, for each of the 18 ROIs many different models and starting values for the fit were tested. The overall number of tested models for the whole survey region was ~ 200. The net time effort for a single person conducting the whole modelling of the Galactic Plane with Gaussian components is estimated to $\sim$ four weeks. Thereby most of the time is spent finding stable models for

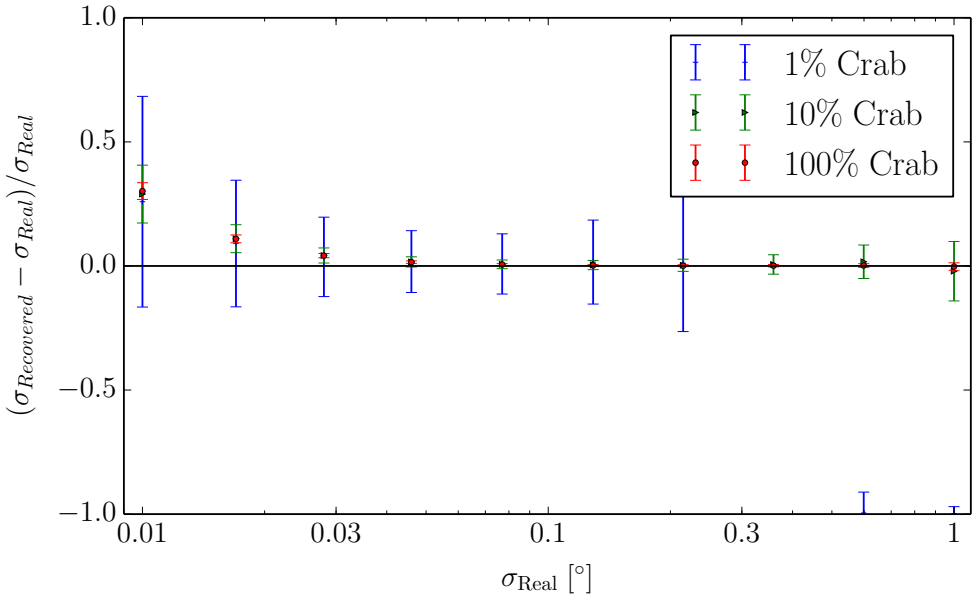

Figure 4.6.: Real vs. recovered size of a simulated source with 0.02°/pixel.

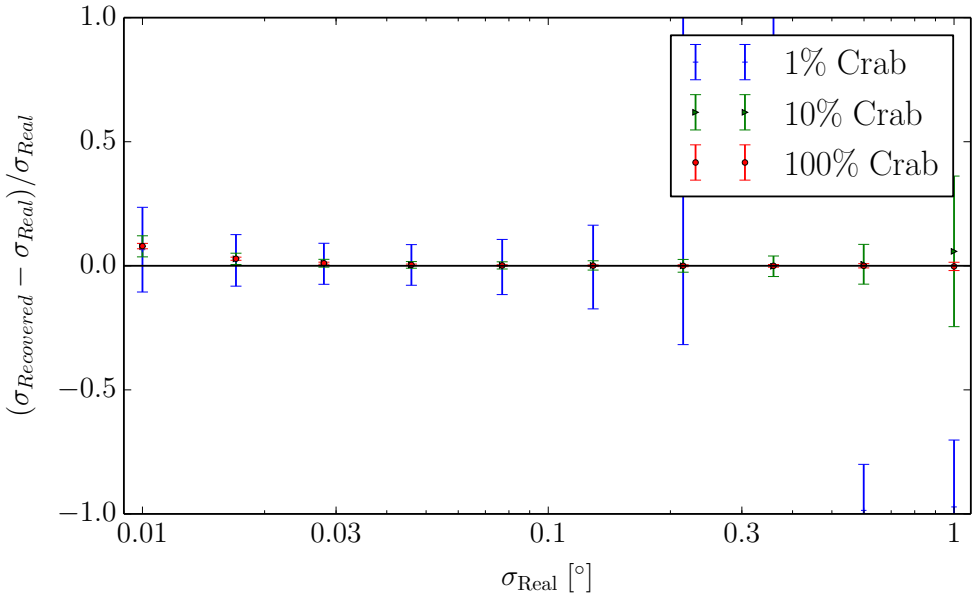

Figure 4.7.: Real vs. recovered size of a simulated source with 0.01°/pixel.

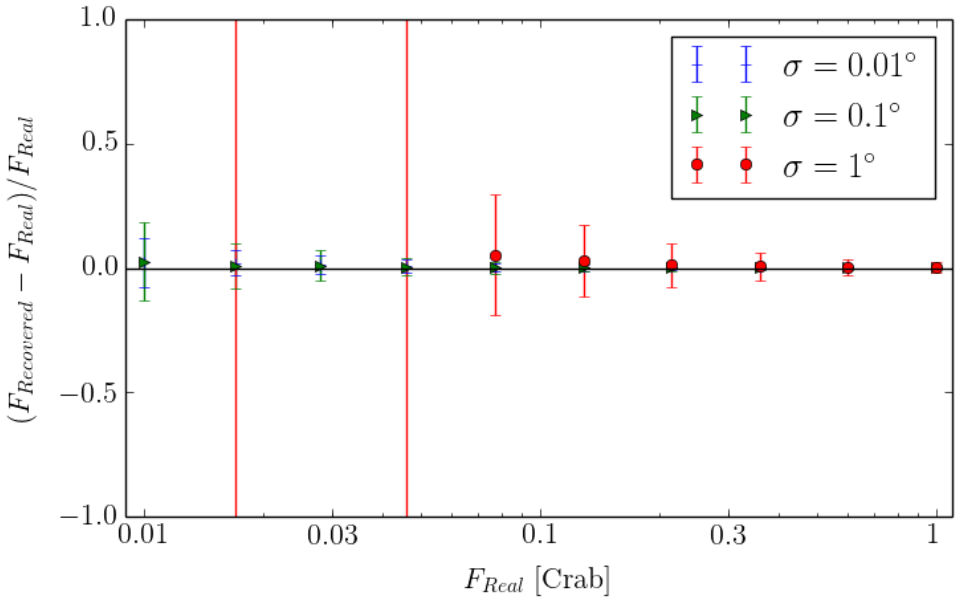

Figure 4.8.: Real vs. recovered flux density of simulated sources: The flux density of was varied in 10 logarithmic steps between 1% Crab and 100% Crab. This was done for three different sizes $\sigma = 0.01°$, $\sigma = 0.1°$, and $\sigma = 1°$. In total $N = 1000$ count maps were simulated and fitted with the pipeline. No significant bias or deviation of the recovered fluxes could be observed.

complex ROIs. Among these ROIs are:

As the model includes PSF convolution and considerably large datasets (in the order of a few 10^5 pixels per ROI) the computational effort also can't be neglected. The processing of a set of models for a single ROI, including the *morph_cutout*, *morph_pre*, *morph_fit* (including covariance computation), *morph_post* and *morph_overlap* steps can take up to four hours, when using a computer cluster. The software was modified, that ROIs can be processed in parallel, that's why the total processing time limits to the processing time of the most time-consuming ROI *GLON_008.5*. A strong correlation between the processing time and the maximal number of components and parameters involved in the fit could be observed. This justifies again the division of the HGPS region into ROIs.

5. Astrophysically Motivated Gamma-Ray Source Catalogs

As seen in the previous chapter extended sources have to be modelled with multiple significant components. This is an effect of the Gaussian morphology assumption, which does not account for elongation, core and halo emission or any other irregular variation of the emission within the source. A prominent example is *Vela X* (see Figure 5.1), where the elongation is modelled with two components and the halo emission with an additional third component. This decomposition of sources is an undesirable effect, but unavoidable when the morphology assumption does not describe the data well enough. The effect was investigated in detail on simulated data. The study and the results are described in Appendix A.

Ideally in a catalog one listed source corresponds to a single astrophysical object, which is obviously not the case for the component list presented in chapter 4. In order to obtain a more meaningful catalog it desirable to group components into sources. In the first section of this chapter a reference catalog is created by manually classifying and associating source components. In the subsequent section automatic methods and simple selection criteria are studied with the goal to reproduce the manually created reference catalog.

5.1. Manual Classification and Merging of Source Components

As the catalog creation already includes a certain amount of manual work, e.g. defining ROIs and the fitting process, it can be justified to merge components also manually. Using additional knowledge about the sources e.g. based on previous H.E.S.S. publication or MWL information, components are grouped into sources. Additionally components can be classified to be *unresolved* if they can not be assigned to any source, e.g. because they are largely extended and lying underneath other known sources. The manual classification and merging of source components was done by a H.E.S.S. expert. The table in Appendix D (p. 81) lists the result.

As the selection of components is done by a single person, it has to be kept in mind, that the result will be strongly biased and depend on the knowledge of the expert. Anyway the resulting catalog will be used as a reference, as the method is expected to yield the most reasonable results.

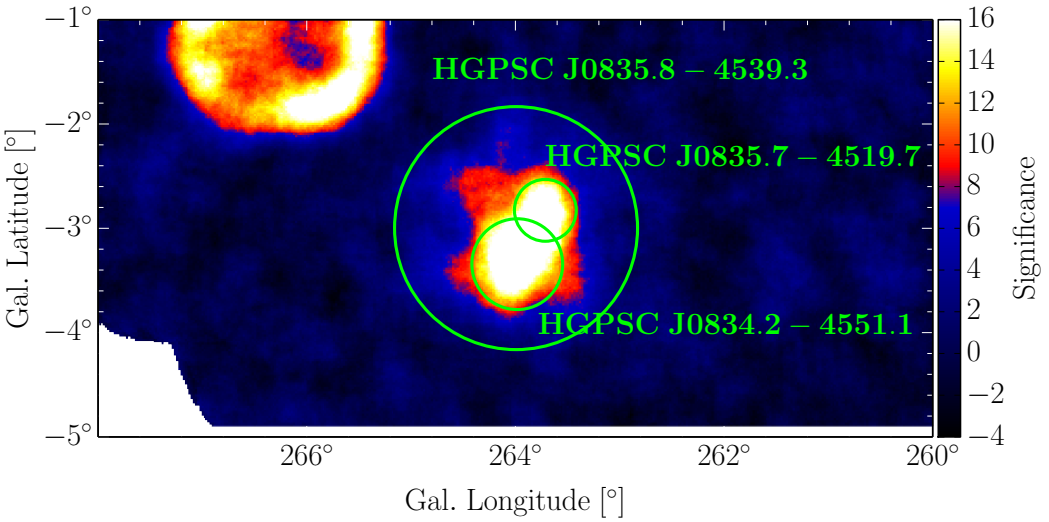

Figure 5.1.: Example of a decomposed source: *Vela X* is modelled by three significant Gaussian components. The two smaller components model a slight elongation of *Vela X*, the third component the underlying and surrounding halo emission. The goal is to assign the components to the same object and merge them into one single catalog source. The contours are at a level of 4σ, 8σ, 12σ and 16σ.

To estimate the characteristics of a sources consisting of a few Gaussian components, the 0th, 1st and 2nd moment of the source's excess model image were computed. As the source components are all Gaussian, this can be done analytically, including the estimation of the error. The formulae and their derivation are given in Section B (p. 65) of the appendix.

5.2. Unresolved Emission Components

In many ROIs it was observed, that tested smaller emission components, were dramatically increased by the fit and resulted in a largely extended component, which was located underneath other sources. This effect of was already reported in C. Deil, 2011, where 6 components were labeled as *diffuse* for this reason. In this work, because of the lower detection threshold of $TS = 30$ and a more detailed modelling of the survey excess, even more of this largely extended, unresolved components were found. In the following the possibility to identify these components by simple cuts in size and significance will be presented and discussed.

In a first step these components were identified manually and separated from components which could be doubtlessly assigned to sources. This was done along with the manual merging of components outlined in the previous section. The estimated total number of this unresolved emission components was 18, which is considerably higher compared to C. Deil, 2011. Seven of this 18 components belong to the ROI *GLON_000.5* and model the

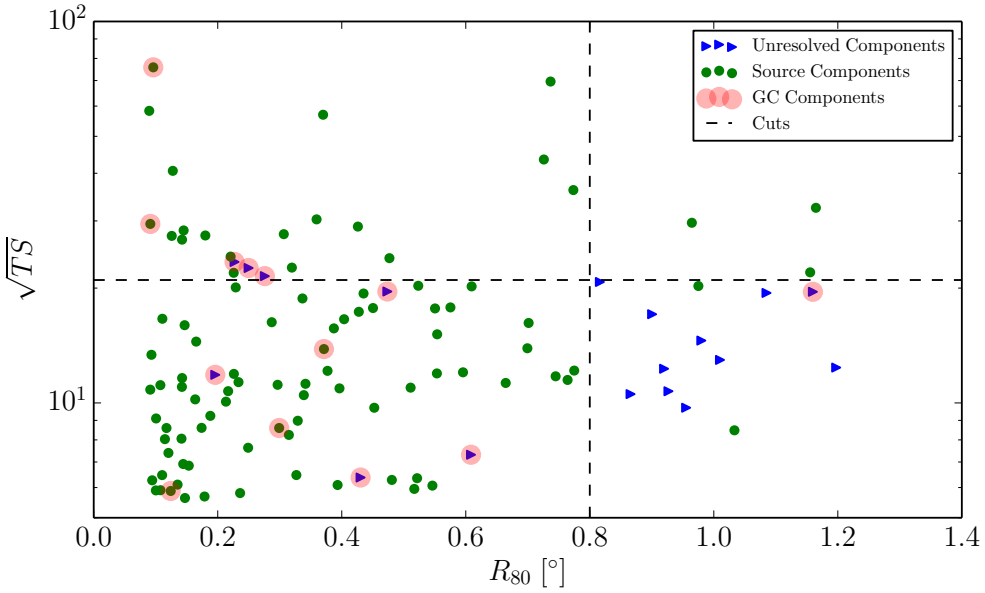

Figure 5.2.: R_{80} vs. $\sqrt{TS}$ scatter plot with empirically defined cuts to separate source and unresolved components. Most of the unresolved components can be found in the lower right of the distribution, because they typically have large extensions, but are not as significant as (known) sources. The largely extended source above the marked $\sqrt{TS}$ threshold are *Vela X*, *HESS J1825-137* and the *Westerlund* region. The Galactic Center includes several smaller unresolved components, but they model known real diffuse emission, which should be treated separately.

Galactic Center ridge emission. This is an effect of the Gaussian morphology assumption, that complex sources decompose into several components if the emission is very significant (compare to the elongated Gaussian morphology model in Appendix A). The remaining 11 largely extended components model underlying unresolved emission of other ROIs.

Figure 5.2 shows the distribution of all components in a $\sqrt{TS}$ vs. R_{80} scatter plot, where $\sqrt{TS}$ is a measure for the significance of a component. The manually selected unresolved emission components are drawn in blue, components that were assigned to sources are shown in green. The components of the Galactic Center are additionally marked by a red circle. Except for the Galactic Center the unresolved components can be mostly found in the lower right of the distribution. They have large extensions typically $R_{80} > 0.8°$ but compared to sources the show less significance, in the shown distribution an empirical separation cut could be made at $\sqrt{TS} = 21$. The value is chosen such that the components of the three known largely extended sources *Vela X*, *HESS J1825-137* and the *Westerlund* region are not affected. Anyway a few borderline case were identified, which shall shortly be discussed. They are shown in Figure 5.3:

- *HGPSC J1908.1-0625.9* is a known isolated source, reported by the H.E.S.S. collaboration in Aharonian et al., 2009. Compared to the value for the extension of $\sigma = 0.34°$ that is quoted in the paper, the value obtained from the catalog pipeline was significantly higher ($\sigma = 0.54°$). Due to a value of $\sqrt{TS} = 20$ it will be classified as unresolved.

- *HGPSC J1409.5-6135.5* models the known hotspots *HESS J1406-613* and *HESS J1414-619* as one single large component.

- *HGPSC J1634.5-4743.5* is a region close to the *Westerlund 1* region it has two other components on top of it and will be classified as unresolved.

- *HGPSC J1715.7-3842.6* is a region in the west of the cut out shell type SNR *HESS J1713-347*. It has three other components on top of it and will be classified as unresolved, but it seems to contain a lot of flux of the three superimposed components.

A model flux image of all components classified as unresolved by the previously defined criteria can be seen in Figure C.6 (p.73). The diffuse emission of the Galactic Center was included. Almost all unresolved components are located near $b = 0°$, except for the one in the south of *HESS J1825-137*. Many of the components have comparable brightness and their size is similar to the the size of the exclusion region. A slight correlation of the unresolved components with high-exposure regions can be observed. The total flux contained in this components is about 260% Crab.

The origin of this largely extended components is not yet known. There could be a connection to true Galactic Diffuse emission and unresolved sources along the Galactic plane, which become significant in high-exposure regions. As studied in Egberts et al., 2013 there is significant excess outside source exclusion regions, which can be assumed to be also underneath source. A different explanation could be systematics in the background. It is known that the adaptive ring background estimation subtracts large scale features from the data and does not yield reliable background estimation for very extended emission. This effect has not yet been investigated in detail.

5.3. Automatic Component Merging Methods

5.3.1. Introducing the Q-factor

For an automatic merging algorithm a quantity is needed which measures the similarity of components in terms of position, size and possibly flux. If several components are similar in this sense they belong more probably to the same source. A suitable quantity for is the Q-factor, which is defined analogue to the correlation coefficient known from signal processing[1].

[1] `http://de.wikipedia.org/wiki/Korrelation_\%28Signalverarbeitung\%29`

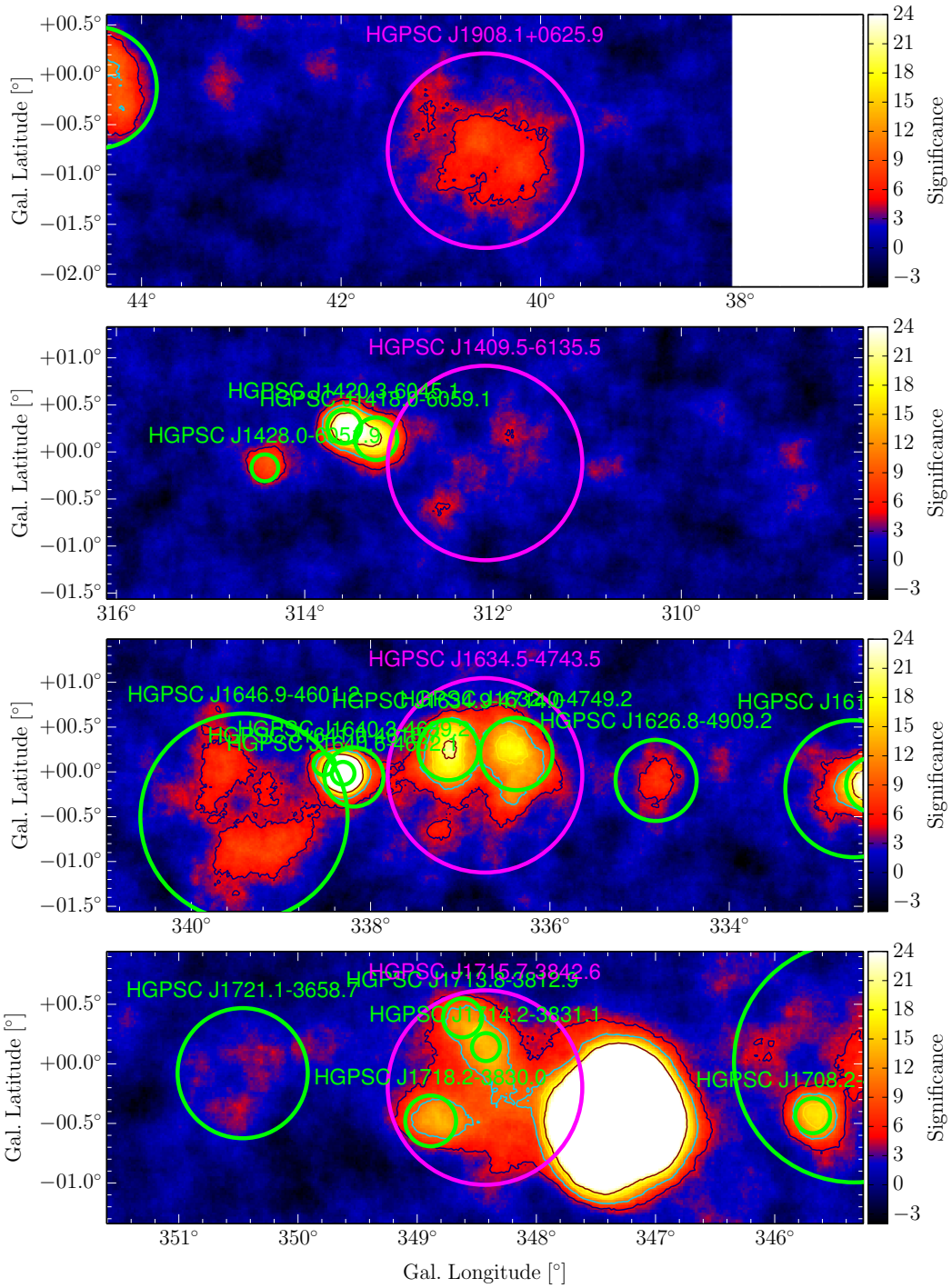

Figure 5.3.: There are mainly four boundary cases where components are either erroneously classified as unresolved (two upper panels) or the decision is not obvious, even by eye (lower two panels). The classification was made using the empirical cuts defined in Section 5.2. Unresolved components are show in magenta, regular source components are shown in green. See text for more detailed annotations.

It measures the similarity of two component models A and B:

$$Q_{AB} = \frac{\int A(\vec{x}) \cdot B(\vec{x}) d^2x}{\sqrt{\int A(\vec{x})^2 d^2x} \cdot \sqrt{\int B(\vec{x})^2 d^2x}} \tag{5.1}$$

Given the assumption that we only have symmetrical Gaussian source components, the overlap factor Q can be derived analytically. This may be useful for a deeper understanding and to save computing time if necessary. A detailed derivation is outlined in Appendix B. Here only the result shall be given:

$$Q_{AB} = \frac{2\sigma_A \sigma_B}{\sigma_A^2 + \sigma_B^2} \exp\left(-\frac{\vec{x}_{AB}^2}{2(\sigma_A^2 + \sigma_B^2)}\right) \tag{5.2}$$

The value of the Q-factor only depends on σ_A, σ_B and the displacement $\vec{x}_{AB}$ of the component's center. By definition the Q-factor is between zero and one and will be given, from now on, in percent. A value of $Q = 100\%$ means identical shape and position of the components, $Q = 0\%$ no similarity between the components. Figure 5.4 shows an illustration. The Q-factor corresponds to the volume under under the red curve which is given by $A \cdot B$. For the catalog creation the Q-factor was computed numerically, based on images of the model components.

Contamination

The Q factor is not sensitive, at least for a single pair of source components, to the brightness of the components (see. formula 5.2). Therefore the overlap of a weak large component and a small but very bright component would be the same as if the smaller component was less bright, compared to the large source. But in the latter case one would more likely consider the small source to be part of the excess of the large one. So it is reasonable to introduce a second overlap criterion, which measures the *contamination* of a source region by another component, which is close by. We call this quantity the C-factor and define it as follows:

$$C_{AB} = \frac{\int_{\mathcal{A}} B(\vec{x}) d^2x}{\int_{\mathcal{A}} A(\vec{x}) d^2x + \int_{\mathcal{A}} B(\vec{x}) d^2x} \tag{5.3}$$

It corresponds to the ratio of the excess of a single source component A and the total excess in a given containment (e.g. 80%) region. The contamination was not further considered but is listed in the component list as an additional quantity.

5.3.2. The Q-forbid Method

The first method to handle the problem of sources decomposing into several components uses the Q-factor to forbid solutions where Gaussian components are overlapping too much. The basic approach is as follows:

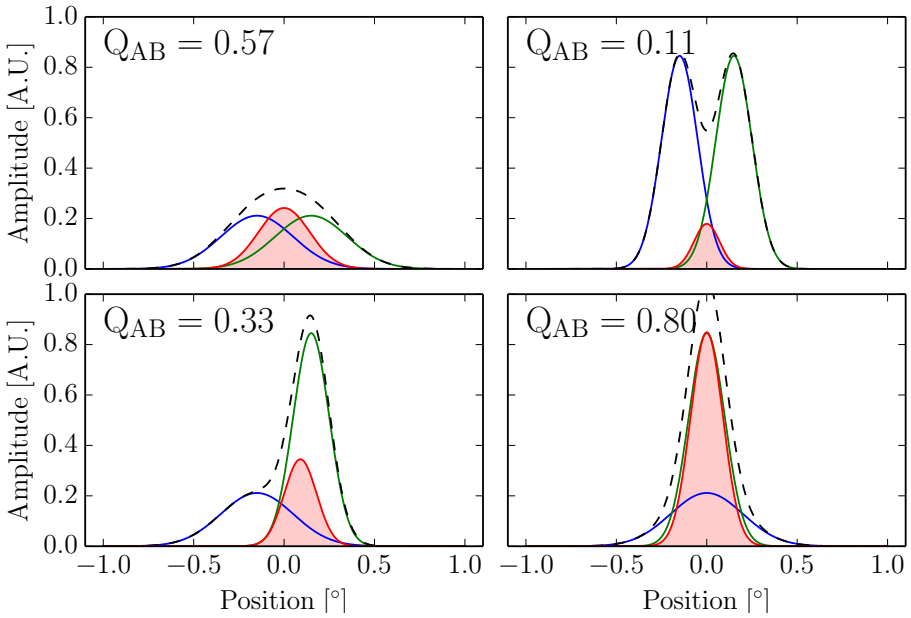

Figure 5.4.: Q-factor between two Gaussian components with different width and distance: The green and blue line show the flux profile of two Gaussian components A and B. The Q-factor corresponds to the area under the red curve $Q_{AB} = \int A \cdot B$. The dashed line shows the total flux profile $A + B$. The plot in the upper left shows the Q-factor for a distance of $\vec{x}_{AB} = 0.3°$ and identical width $\sigma_A = \sigma_B = 0.3°$ of the components. The dashed enveloping curve does not show any dip between the components. In this case both components may be assigned to the same source. In the upper right the width of both components was assumed $\sigma_A = \sigma_B = 0.1°$ which results in much smaller value for the Q-factor. In this case the components would kept as two separate sources. The lower left shows the example of a smaller and a larger source, which are close by. Even if there is no clear separation visible, the Q-factor is rather small, because of the different width of the components. The last example in the lower right shows a source which decomposes into a core and halo component, in this case we have $Q = 0.8$.

(1) Given the solution with the highest TS values and N components, the pairwise Q-factor between all components is computed

(2) If for any pair of components the Q-factor is above a certain threshold Q_{Th} this solution is disallowed and the solution with $N-1$ components is chosen

(3) Iterate the procedure until a solution is found, were no pair of components as an overlap larger than Q_{Th}

The method has the disadvantage that it can only be applied to a whole ROI and may therefore effect components in the ROI, which are actually not part of the problematic region. E.g detections could be lost if a weak source anywhere in the ROI is much less significant than a second component of a strong source in the same ROI. Because the method forbids the solutions with strong overlapping components, details of the morphology of the source may be lost, resulting in larger residuals. Unresolved components, as presented in Section 5.2 are not excluded, because usually they have a strong overlap with other components and will most likely be disallowed. This introduces a further bias of the method because underlying emission is modelled as part of the sources and not separately.

5.3.3. The Q-merge Method

In contrast to the *Q-forbid* method the overlap factor is now used to merge components. Starting from the list of Gaussian component, the unresolved components are excluded, by making a combined cut at $R_{80} = 0.8$ and $\sqrt{TS} = 21$. Then the pairwise overlap of source components is computed numerically using formula 5.4. The integral is replaced by the sum over the component's model excess image, which was saved separately for every component during the fit. The model images were computed by evaluating the model with the final fitted parameters, multiplying with the exposure and convolving the image with the PSF model. The subsequent merging process is done as follows:

(1) Given a solution with N sources the pairwise Q-factor between all components is computed.

(2) Sort out diffuse components manually based on the selection cuts of Section 5.2.

(3) Search for connected components, where the connection of two components A and B is defined by $Q_{AB} > Q_{Th}$.

(4) Merge the connected components by computing the 0th, 1st and 2nd moment of the summed flux distribution, as described in Section B.

In this approach Q_{Th} defines the maximal allowed overlap, before components are merged. A smaller value of Q_{Th} means less sources, because more components are merged. This method has the advantage, that all components are kept, but grouped into sources. No detections and details of the modelling are lost. It is is an automatic approach for the

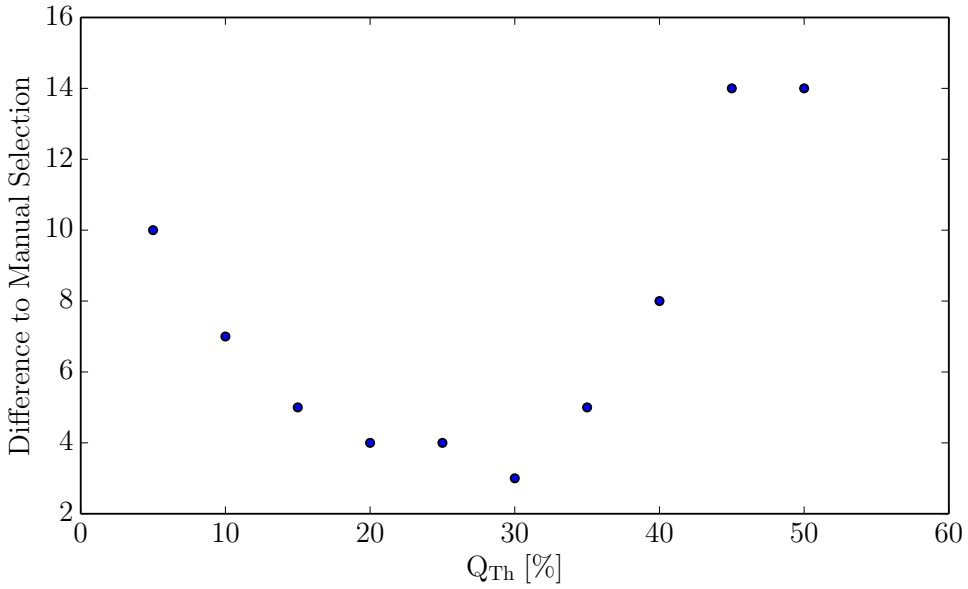

Figure 5.5.: Difference between Q-factor merging method and Manual Selection of components to merge. A well defined minimum could be found for $Q_{Th} \approx 30\%$, where only three components were different. The differences could be identified in two regions, which are shown Figure 5.6. For $Q_{Th} > 45\%$ no components are merged at all.

manual merging process. In a first try this method was applied to the full component list, which led to wrong results, because the large underlying resolved components connected components which did not belong together. In a second, improved version the unresolved components were excluded as described above. The search for connected components was done with a standard graph-theory algorithm [2].

5.4. Results

5.4.1. Reproduction of the Reference Catalog

As a first step it was necessary to find an appropriate maximal value Q_{Th} for the Q-factor. Therefore the catalog based on the manual selection and merging of the components was used as a reference. Based on the component list presented in Chapter 4 with a TS threshold of $\Delta TS = 30$ and excluded unresolved components, the Q-factor for the Q-merge method was varied between $Q_{Th} = 5\% - 50\%$ and the number of different components to the manually

[2] `http://en.wikipedia.org/wiki/Connected_component_\%28graph_theory\%29`

Q_{Th}	20%	30%	40%	50%
Q-forbid	59	69	81	94
Q-merge	75	76	80	83

Table 5.1.: Total Number of Sources for different values of Q_{Th} for the Q-merge and Q-forbid method. The total number of sources in the reference catalog is 78

created catalog was computed. Figure 5.5 shows the result. A well defined minimum could be found for $Q_{Th} \approx 30\%$, where only 3 components were different.

The differences are restricted to two regions, which are illustrated in Figure 5.6. The manually selected source components for merging are shown as green circles, the result of the Q-merge algorithm is shown in white. One difference was found in the Galactic Center region, where the Q-merge algorithm kept the components *HGPSC J1746.3-3049.4* and *HGPSC J1744.7-3022.7* separated, whereas the H.E.S.S. expert decided to define only one source, confirming in private communication that it was without strong reasoning. The second difference was identified in the region of *HGPSC J1834.5-0844.8*, where an additional halo component *HGPSC J1834.7-0843.7* was merged by the automatic algorithm, whereas the H.E.S.S. expert classified the halo component as *unresolved*. All results which are shown later will be using $Q_{Th} = 30\%$ for the Q-merge method.

Finding an appropriate Q_{Th} for the Q-forbid method turned out to be considerably complex, as for different values of Q_{Th} a different model for the ROI is chosen. This is in contrast to the manual selection method and the Q-merge algorithm, which are based on the same model for the survey excess, presented in Chapter 4. As the Q-forbid approach disallows models for ROIs with to much overlapping components, the level of modelled morphology and excess details is much lower. To find out whether the obtained results are acceptable, Q_{Th} was varied in steps of 10% from 20% to 50% and the residual significance distribution for every value of Q_{Th} was determined on a 0.2° scale. The result is shown in Figure 5.7. Additionally the total number of found sources is shown in Table 5.1. From the total number of sources one concludes that a value of $Q_{Th} = 30\% - 40\%$ would be suitable, but taking a look at the residual significance distribution reveals that for $Q_{Th} = 30\% - 40\%$ a lot of significant excess is left unmodelled. The corresponding residual significance contours are shown in Appendix C.7 (p. 74). Significant residuals can be found in complex regions such as the Galactic Center or around *HESS J1825-137*. Furthermore some isolated, weakly significant sources were missed e.g. *HESS J1747-248* and *HESS J1626-490*, because they were only included in a more detailed model, which was disallowed due to strongly overlapping components in other parts of the ROI. Because of the mentioned disadvantages i.e. too much significant residuals and missed detections, the Q-forbid method was rejected.

5.4.2. Comparison of Source Parameter Distributions

Starting from the component list with $\Delta TS = 30$ catalogs were created by merging components into sources with the Q-merge algorithm with $Q_{Th} = 30\%$. Sources were named

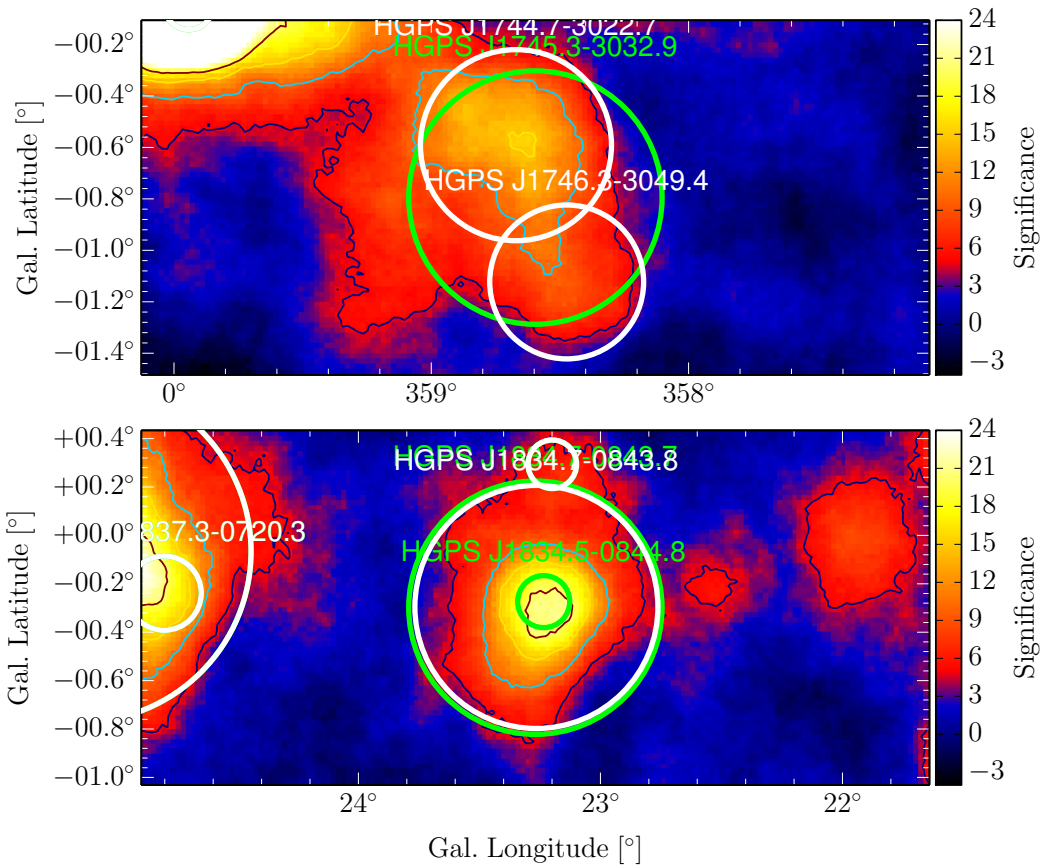

Figure 5.6.: Only two regions with differences between Q-factor merging method and Manual Selection of components could be identified. One difference was found in the Galactic Center region, where the Q-merge algorithm kept the components *HGPSC J1746.3-3049.4* and *HGPSC J1744.7-3022.7* separated, whereas the H.E.S.S. expert decided to define only one source. The second difference was identified in the region of *HGPSC J1834.5-0844.8*, where an additional halo component *HGPSC J1834.7-0843.7* was merged by the automatic algorithm, whereas the H.E.S.S. expert classified the halo component as *unresolved*.

according to the following scheme:

$$\text{HGPS JHHMM.m} + \text{DDMM.m}$$

Were JHHMM.m denotes the right ascension and DDMM.m the declination of the Gaussian component. In order to avoid duplication of component names it was necessary to specify 5 digits of right ascension and declination.

For the reference catalog a total number of 78 source was obtained, 76 for the Q-merge catalog. The difference is due to the two known H.E.S.S. sources classified as unresolved

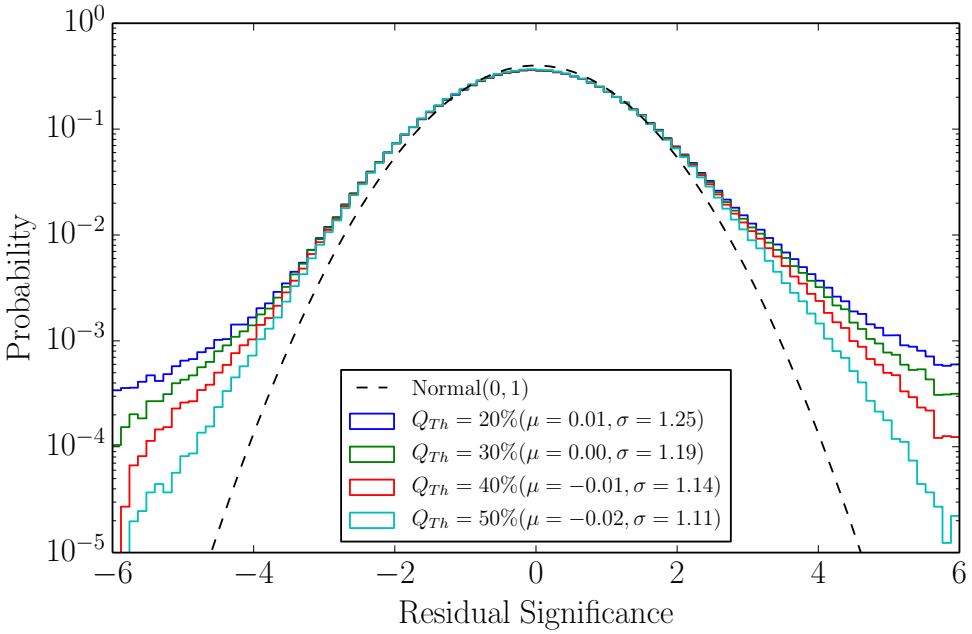

Figure 5.7.: Residual significance distribution of the Q-forbid method for different values of Q_{Th}. The distribution shows large significant residuals, indicating that many regions are not modelled accurately. Most of the residuals can be found in complex regions, where multiple overlapping components are needed to obtain an appropriate representation of the excess in this region. The corresponding residual map, which shows the correlation with complex regions, can be seen in Figure C.7 (p. 74).

by the cuts in size and significance. As a first overview Figure 5.8 shows the fraction of sources in both catalogs with 1, 2 or 3 components. Most of the catalog sources (83%) consist of only one Gaussian component and did not decompose. A fraction of 13% consists of two components and only 4% decomposed into 3 components. The sources modelled with three components are *Vela X*, *HESS J1825-137* and *HESS J1514-591*. In the best-fit model, the emission of *HESS J1825-137* is actually described by 5 components, but one large component in the south was classified as unresolved and a second component in the north-east of *HESS J1825-137*, was classified as an own source. A total fraction of 17% of the sources in the HGPS region decompose into multiple components.

Figure 5.9 shows the distribution of the Galactic longitude of all sources and components respectively. The main differences between the component list and the merged catalogs can be observed in the range from $l = 40°$ to $l = -20°$, which is the part of the Galactic Plane with a higher source density. The catalog created with the Q-merge method only slightly deviates from the manually created reference catalog.

The histogram of the Galactic Latitude is shown in Figure 5.10. The largest differences

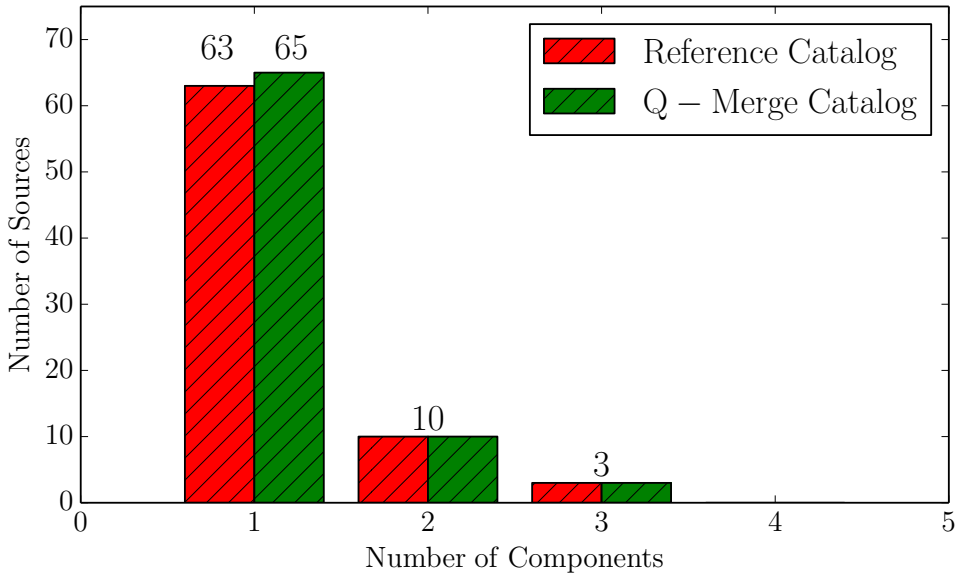

Figure 5.8.: Distribution of the number of components per source in the catalog. The difference in the one component sources is due to the different classification of *HGPS J1908.1-0625.9* and *HGPS J1409.5-6135.5*. A fraction of 10 of 76 sources consists of two components and only three decomposed into three components. The sources modelled with three components are *Vela X*, *HESS J1825-137* and *HESS J1514-591*.

between the components list and the merged catalogs can be noticed in the range $b = -0.5°$ to $b = 0.5°$. The differences include excluded unresolved and merged components. The two sources at high Galactic latitudes are two hotspots *HGPS J1812.3-1128.4* and *HGPS J1813.3-1241.5* and the source close to *Terzan 5* (*HGPS J1747.8-2449.1*). The source at low Galactic Latitudes are *HGPS J1506.8-6218.3* and a component right next to it *HGPS J1510.0-6235.6*, which was kept as an own source, but could also be part of the emission of *HGPS J1506.8-6218.3*. The other sources are *Vela X*, *HGPS J1355.8-6430.4*, *HGPS J1708.0-4416.8* and *HGPS J1442.8-6226.2*.

Figure 5.11 shows the distribution of sizes for the reference catalog, the Q-merge catalog and the component list. The component list features a bias to large sources ($\sigma > 0.4°$), which can be explained by the existence of the large unresolved components, which where excluded in the other catalogs. A second bias is noticed for smaller source sizes ($\sigma < 0.2°$), which is due to the fact that larger sources decompose into smaller components. For the reference catalog and the Q-merge catalog the highest number of sources can be found in the range $\sigma < 0.1$. For both catalogs the number of sources with larger extensions decreases almost linearly to only three very large sources with $\sigma > 0.5°$. These sources are *HESS J1825-136*, *Vela X* and the *Westerlund 1* region.

The histogram of the source fluxes (Figure 5.12) shows for all catalogs a bimodal distribution of the sources. One peak is found slightly above 10% Crab, another peak approximately at 3% Crab. Again a bias in the component list is observed, where less very bright sources are observed, because they decompose into smaller less bright components. The three sources above 50% Crab are *HESS J1825-136*, *Vela X* and *HGPS 1837.4-065.7*. The weakest source found in the catalog was *HGPS J1741.2-3032.8* with a flux level of 0.7 ± 0.2% Crab.

As a summarizing plot a cumulative *Log N - Log F* distribution is shown in Figure 5.13. For a complete comparison of all catalogs, the *Q-merge* method was included again. The total number of sources in the catalogs and the component list differ by the excluded unresolved components. The component list again features a bias at higher fluxes, because bright sources decompose into multiple components, which is reflected in a steeper increase of the curve for the component list in the range 10% - 20% Crab. In general it can be concluded, that the creation method has a strong influence on the final shape of the *Log N - Log F* distribution. A simple interpolation of the distribution to estimate the number of sources, which fall below the current sensitivity of H.E.S.S. , will be biased by the method, the catalog is created with.

As an additional check Figure 5.14 shows the variation of the total flux contained in sources and components above a given flux threshold, whcih corresponds to an integral *Log N - Log F* distribution, where each counted source is weighted with its flux. The total flux for all components, including unresolved components, is $\sim$ 11 Crab. After excluding unresolved components, the total emission contained in the *Q-merge* catalog is $\sim$ 8.5 Crab, for the reference catalog it is $\sim$ 9 Crab. The difference is due to the sources *HGPS J1908.1-0625.9* and *HGPS J1409.5-6135.5*, which were classified as unresolved by the automatic method (see Section 5.2).

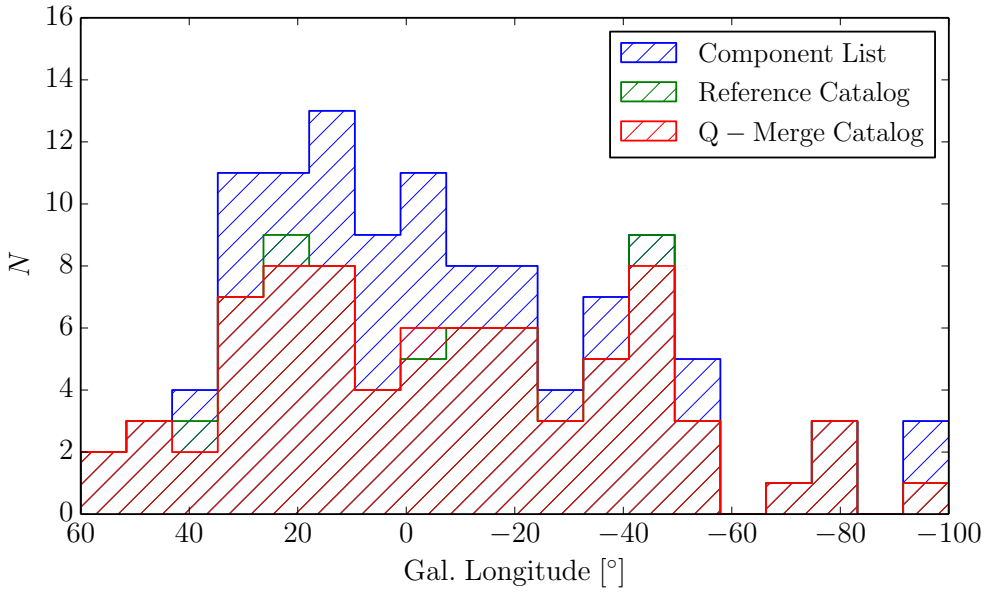

Figure 5.9.: Distribution of the Galactic longitude of catalog sources and components.

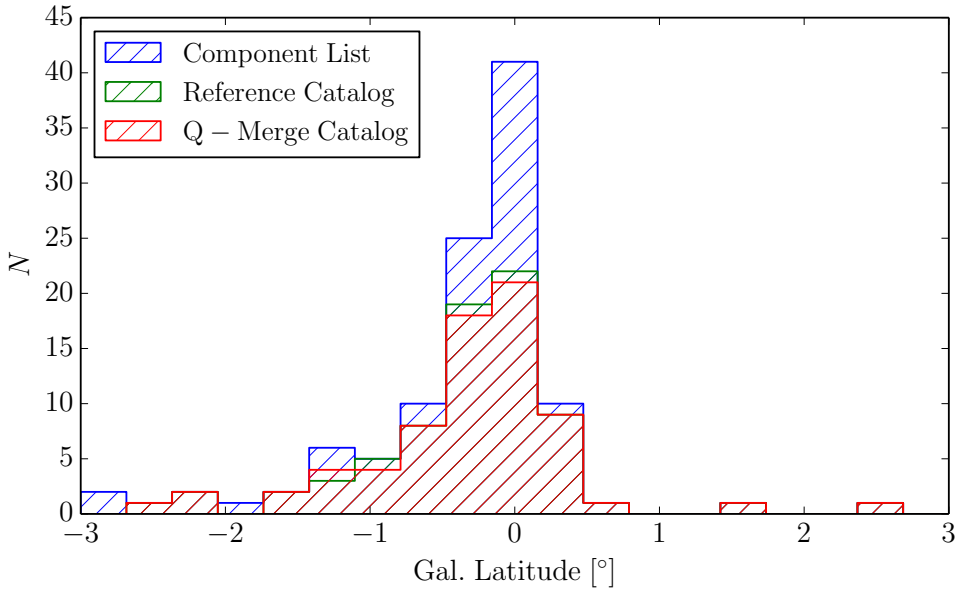

Figure 5.10.: Distribution of the galactic latitude of catalog sources and components.

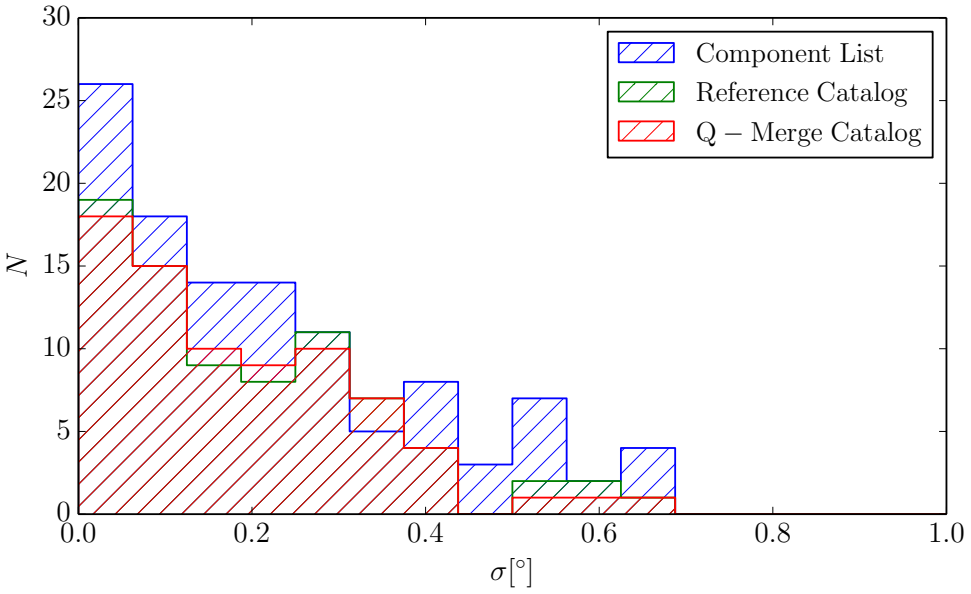

Figure 5.11.: Distribution of the size, given as the Gaussian width σ.

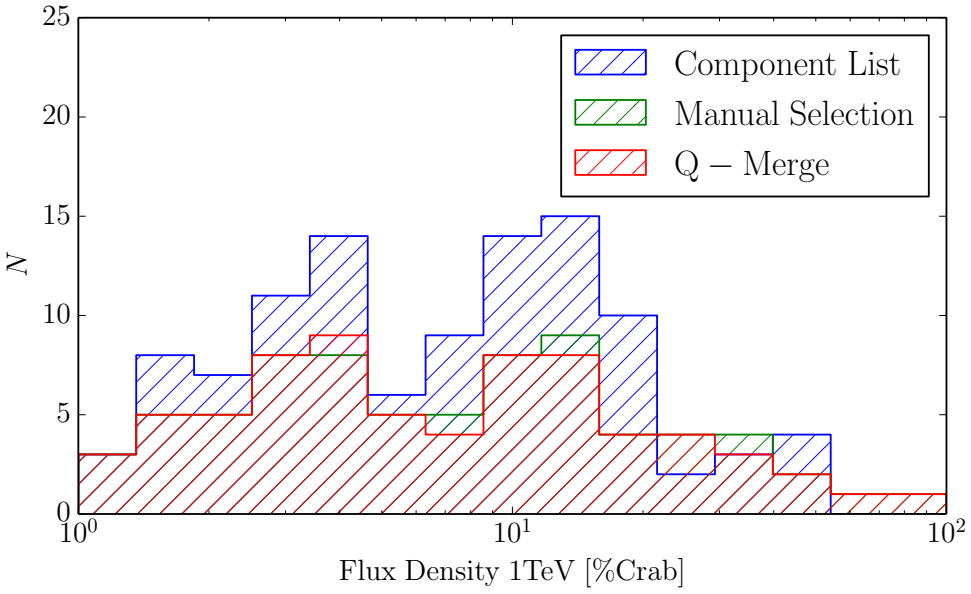

Figure 5.12.: Distribution of differential flux densities. The differential flux density is given at 1 TeV. As reference for the Crab flux Meyer, Horns and Zechlin, 2010 was used.

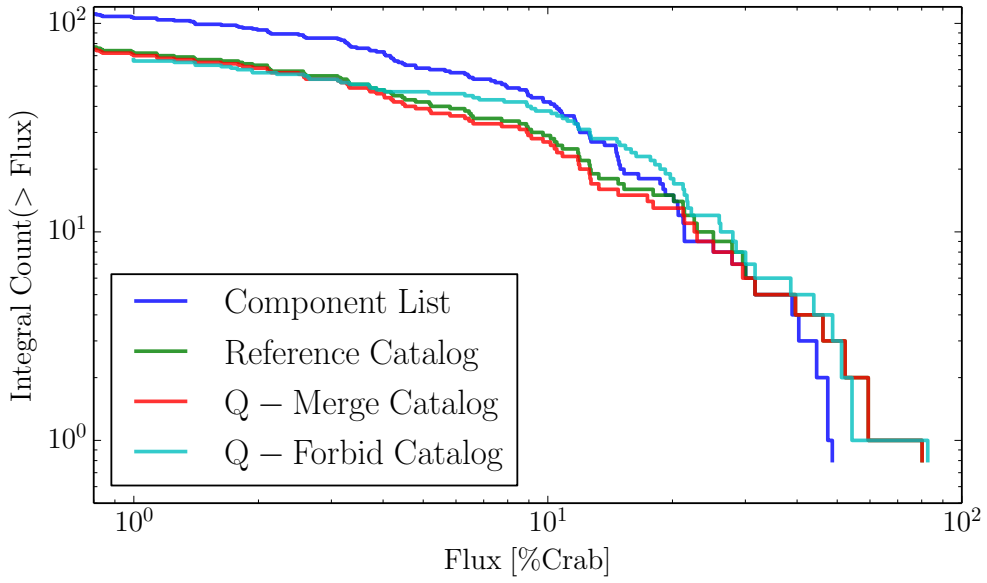

Figure 5.13.: Integral Log N - Log F distribution

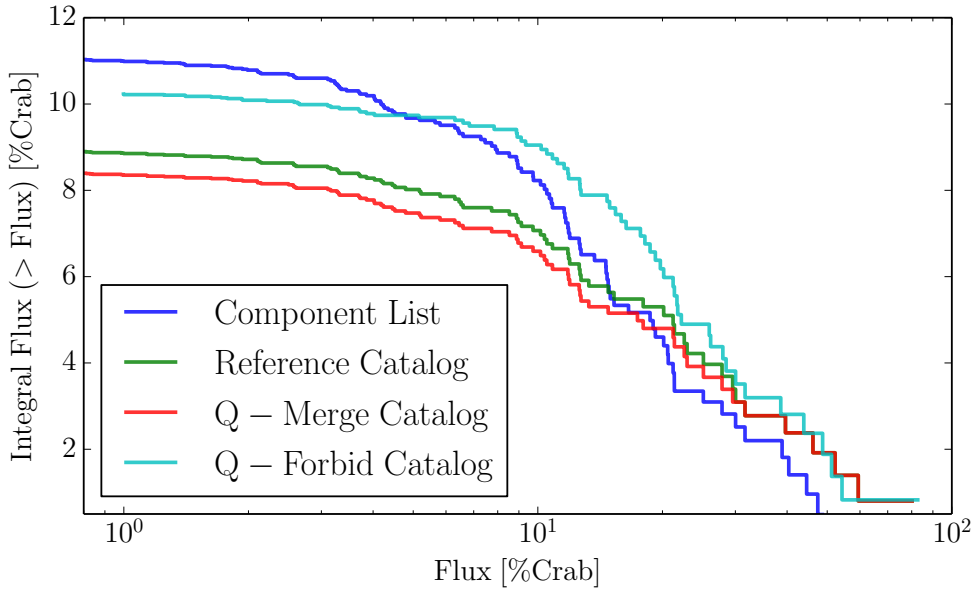

Figure 5.14.: Integral Log N - Log F distribution, weighted with the flux of each counted source.

6. Summary and Discussion

Based on the ten year HGPS dataset, the gamma-ray emission of the Galactic Plane was fitted. The Galactic plane was divided into 18 regions of interest (ROI), where each one was modelled in detail with a Likelihood-Fit procedure, assuming a Gaussian morphology of the sources. A lot of effort was put into varying start parameters to finally arrive at a global best model for the ROI. Applying a detection threshold of $TS = 30$ a total number of 112 source components was found.

The fitted positions were checked with the point-like sources *Sag A**, *HESS J1302-638* and *HESS J1826-148*. No significant deviations from the reference positions could be found. The recovery of source parameters was checked on simulated data. An overestimation of source sizes $< 0.04°$ was observed for maps with a binning of $0.02°$/pixel. It could be shown that for maps with a resolution of $0.01°$/pixel the bias was negligible. The recovery of the flux was not affected.

Creating the source component list two important observations could be made:

- In many ROIs it was hard to reproduce smaller, previously detected sources by H.E.S.S. in the first try. Even with carefully chosen starting values, the Gaussian converged to a largely extended component, which was located underneath the other sources in the ROI. Only by including this large-scale *unresolved emission* component in the model, also smaller known H.E.S.S. sources could be modelled stably.

- Bright extended sources decomposed into multiple components, because the Gaussian morphology assumption does not match the real morphology of the Galactic gamma-ray sources well enough. Mostly sources decomposed into a core and a halo component or into two components side by side, modelling elongation of sources.

To correct for the bias that is introduced by both effects, a reference catalog was created by manually classifying unresolved emission components and merging components of decomposed sources. In total 18 unresolved components were found, where seven of them belonged to the Galactic Center region, modelling the ridge emission around *Sag A**.

An automatic criterion for the identification of largely extended underlying components was defined using cuts in size and significance of $R_{80} = 0.8°$ and $\sqrt{TS} = 21$. Except for the components *HGPSC J1908.1-0625.9* and *HGPSC J1409.5-6135.5*, the result was identical to the classification in the reference catalog. By defining a quantity to measure the overlap of source components, the *Q-factor*, an automatic merging algorithm was developed, which was able to deliver very similar results as the reference catalog. The only deviations were

found in the regions of *HESS J1745-303* and *HESS J1834-087*.

In total the reference catalog contained 78 sources of which ten consisted of two components and three sources of three components (*Vela X*, *HESS J1514-591* and *HESS J1825-137*). The remaining sources were modelled by a single Gaussian. For all sources position, size and flux, including uncertainties were measured. The largest sources in the catalog were *HESS J1825-136*, *Vela X* and the *Westerlund 1* region, with extensions $\sigma > 0.5°$. The brightest sources with fluxes above 50% Crab are *HESS J1825-136*, *Vela X* and *HESS J1837-069*. The faintest source found in the HGPS region was *HESS J1741-302* with a flux level of $0.7 \pm 0.2\%$ Crab.

After C. Deil, 2011, a second improved version of the H.E.S.S. Galactic gamma-ray catalog was presented in this thesis. Issues like reliable multi-scale detection, source confusion in the Galactic plane, decomposition of sources and underlying unresolved emission could be handled to a satisfying degree. This marks an important step towards a publication-ready version of the catalog. The finding of degree scale significant components underneath sources in regions of deep exposure strongly suggests that large-scale unresolved emission has to be considered in more detail in future H.E.S.S. and CTA analyses of Galactic sources. The influence of this unresolved emission on the estimation of source size, flux and spectrum is not well studied, but it can be expected that the effect on weak, extended sources is very strong. In general this shows the need for improved background and unresolved emission modelling in the future.

The usefulness of the catalog for future source population and diffuse emission studies can only roughly be assessed. In the current state the catalog represents a uniform dataset of Galactic gamma-ray sources with estimated position, size and flux. As shown in the last chapter, the shape of the *Log N - Log F* distribution is strongly biased by the method the catalog is created with. Extrapolating the *Log N - Log F* distribution to estimate the fraction of undiscovered sources, as it could be useful for diffuse emission studies, will only allow weak conclusions. In order to be useful for a future Galactic TeV source population studies, the catalog should include spectral parameters for sources. The main difficulties in measuring spectra is the definition of reliable source regions. Due to the high source density in the Galactic plane and the existence of underlying large scale emission, source regions are strongly contaminated by other emission. For which fraction of the Galactic sources a reliable estimation of spectral parameters is possible is not yet known.

7. Outlook

In the following section the next steps towards a publication-ready catalog will be described. Additionally a few long-term objectives are outlined.

Better Modeling of Unresolved Emission

Throughout this work the unresolved emission was modelled with symmetrical Gaussian shaped components. Even if the origin of this emission is not yet known, a relation to true Galactic diffuse emission and unresolved source along the Galactic plane is likely. For this reason the unresolved emission is expected to be rather distributed in an elongated band along the Galactic plane. For the next version of the catalog, it is planned to include a band of diffuse emission in the background model, with the goal that the very extended components described in Section 5.2 are not longer significant anymore. It was shown in recent studies by Regis Terrier, that by adding such a band model the overall likelihood of the model is considerably increased. Currently no detailed physical models for TeV Galactic diffuse emission exist and also the flux level and spatial distribution of unresolved sources is not known. For this reason a band model for unresolved emission can only be extracted from the data itself. Different approaches have been suggested. E.g. the model could be created by assuming a Gaussian profile in latitude and a constant amplitude in longitude. The normalization could be obtained by fitting this model in boxes of width $l = 10°$ or $l = 20°$ to the data outside exclusion regions. However this introduces new difficulties. As the model is not determined globally, it depends on the choice of the size of these boxes. Alternatively a more simple version of a band model could be created by assuming a constant amplitude in longitude across the survey region and a Gaussian shape in latitude. The normalization and width of the Gaussian could be estimated from Egberts et al., 2013. As the band model is not fitted along with the sources, the effect of this band on the sizes and fluxes of the sources has to be studied in detail, to obtain reasonable estimates for the error on the source properties.

Fully Automatic Catalog Creation

The method to create a gamma-ray source catalog, which was presented in this thesis, involves a lot of manual work. In a first step ROIs have to be defined and for every ROI many different models have to be tested to obtain stable results. Finally a manual classification

and merging of components has to be carried out, based on the knowledge of an expert. The large amount of manual work slows down the creation process and does not allow parametric studies and the quick creation of new catalogs on different maps. An application to simulated Galaxies, e.g. as part of population studies, is also not possible. Furthermore the manual work also introduces a subjective bias on the final catalog result, which could be reduced by automatizing the creation process.

A first step in this direction was taken with the automatic classification and merging methods presented in this thesis. One possibility to automatize the fitting procedure, would be to use so called *seed catalogs*. Source detection tools could be used to define a variety of preliminary source detections, which are given as *seeds* to the fitting pipeline. The goal is to have many different seed catalogs in order to replace the manual procedure of trying many different starting values. An alternative approach could use an iterative procedure to add new source components, based on residual TS maps to successively improve the model until a certain threshold is reached. A long term goal, e.g. for a future CTA Galactic Plane Survey, would be the global analysis of the whole Galactic plane using overlapping and "communicating" ROIs and a large scale emission model.

Spectra and Multiband Analysis

The analysis of the HGPS data presented in this thesis, consisted only of a fit of the morphology of sources. Spectral properties of the sources other than the flux were not considered. To also obtain spectra for the sources, the source sizes or equivalent quantities like containment radii R_{80} or R_{50} that are listed in the catalog can be used to define spectral regions. By running a H.E.S.S. standard analysis using aperture photometry, the parameters of the spectra can be estimated.

A better way to determine the property of sources is a combined morphological and spectral fit to the data. One of the main advantages is that close by sources can be separated not only based on spatial but also on spectral information. Furthermore the overall sensitivity is also increased by the combined morphological and spectral analysis. An additional step could include high energy Fermi data in the spectral analysis to reach a much better constraint of spectral energy distribution of sources.

A. Decomposition Study

For this study count maps were simulated assuming different *real* source morphologies. The count maps were fitted again with a Gaussian model, following the procedure described in Section 4.1.3. First the different source morphology models shall be introduced.

Morphology Models

The first model is a simple disk type model with no tails, where constant brightness is assumed within a circular region of radius r_0. This model can be applied to SNRs that show now significant shell structure. F denotes the total flux, x_0 and y_0 the position of the center of the disk:

$$f(r) = \begin{cases} F\frac{1}{\pi r_0^2} & \text{for } r^2 < r_0^2 \\ 0 & \text{else} \end{cases} \tag{A.1}$$

For this model the 80% containment radius is given by $R_{80} = r_0\sqrt{0.8} \approx 0.9R_0$.

Furthermore we consider an elongated Gaussian model, as several H.E.S.S. PWNs show significant elongation. This model is described by:

$$f(x,y) = F\frac{1}{2\pi\sigma_x\sigma_y}\exp\left(-\frac{(x-x_0)^2}{2\sigma_x^2} - \frac{(y-y_0)^2}{2\sigma_y^2}\right) \tag{A.2}$$

Assuming only a slight elongation ($\sigma_x \approx \sigma_y$) we have $R_{80} \approx \sqrt{\sigma_x\sigma_y}\sqrt{2\log(5)} \approx 1.8\sqrt{\sigma_x\sigma_y}$

For several H.E.S.S. sources we observe a significant core and halo component indicating significant emission towards the tails of the source. This can be modelled by a beta function, where the radial brightness follows:

$$f(r) = F\frac{\alpha-1}{\pi r_0^2}\left(1+\frac{r^2}{r_0^2}\right)^{-\alpha} \quad , \text{ for } \alpha > 1 \tag{A.3}$$

The beta model has a 80% containment radius of $R_{80} = r_0\sqrt{5^{1/(\alpha-1)}-1}$. The parameter α controls how fast the brightness decreases towards the tails of the source. During the following study $\alpha = 2$ was assumed, to ensure a significant deviation from the Gaussian model. For $\alpha \to \infty$ the beta model approximates a Gaussian shape.

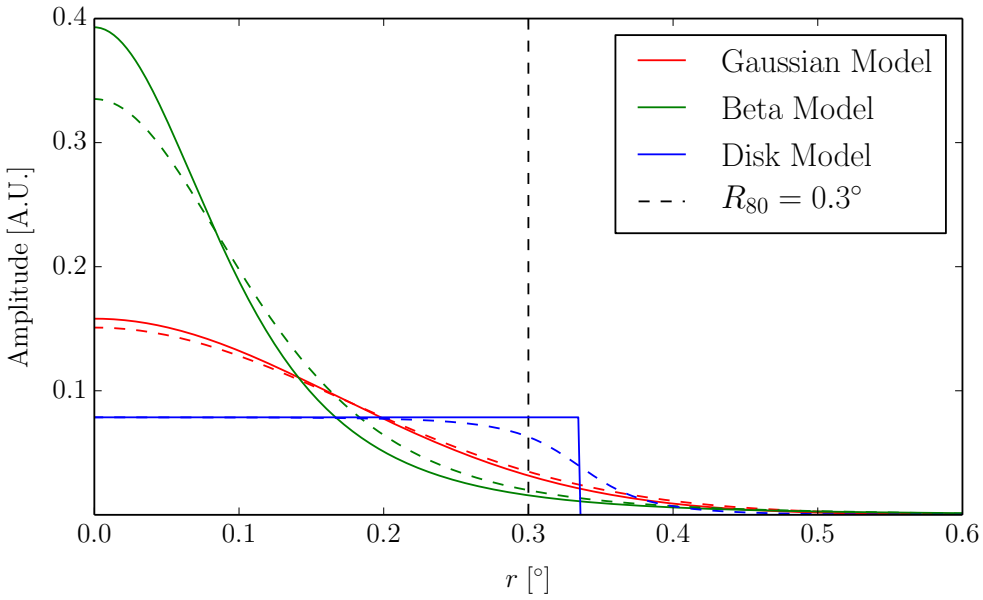

Figure A.1.: Radial profiles of the different source morphology models. All models have the same 80% containment radius of $R_{80} = 0.3°$ and the same total flux, which is normalized to unity. The brightness of the Gaussian model is smoothly distributed. The beta model shows a more distinct emission peak in the center and larger tails. The emission of the Disk model is confined to a well defined region. The dashed line shows the corresponding profiles but convolved with the PSF model of the Galactic Center. The differences between the models are equalised.

Results

For the study all source models were set up with the same 80% containment radius and the same total (integrated) flux. The position was fixed to the Galactic Center and the models were evaluated on a grid with 0.02°/pix using an oversampling of 10 to assure flux conservation, even on small scales. These flux images were multiplied with the real H.E.S.S. exposure of the Galactic center region and convolved with the corresponding H.E.S.S. PSF. After adding the Galactic Center background model to the excess map, the data was fluctuated with Poissonian noise to fake a measured counts map. Finally the fitting procedure described in section 4.1 was applied to the faked counts data.

Fixed size, varying flux

First the containment radius was fixed to $R_{80} = 0.3°$, which roughly corresponds to the size of a typical H.E.S.S. source. The flux of the model sources was varied between 3% Crab, 10% Crab, 30% Crab and 100% Crab. For the elongated Gaussian model a ratio of $\sigma_x/\sigma_y = 2$ was assumed, which models a quite significant elongation in x direction. The parameter α of the beta source model was fixed to $\alpha = 2$, which accounts for distinct peak emission in the center and also sufficient emission in the tails.

Figure A.2 shows the result. For every simulated source morphology the total number and R_{80} of the fitted components are drawn as green circles. The Gaussian source model behaves as expected. As it is fitted with the correct morphology assumption, it does not decompose and gives prefect residuals on any flux scale. The corresponding residual significances are show in Figure A.3. Structures above 5σ would appear red.

The second source model, the elongated Gaussian, already decomposes for the smallest flux value of 3% Crab. The significance of the second component was $\Delta\mathrm{TS} = 25.4$ which is only slightly above the threshold of $\Delta\mathrm{TS} = 25$. At a 10% Crab flux level no significant third component was found, which is confirmed by the residual map, which does not show any significant featues. At 30% Crab and 100% Crab a third and even a fourth and fifth component are necessary to model the elongated morphology properly. But as the residuals show, the overall morphology can be modelled well enough with the multiple Gaussian model.

On the smallest flux scale of 3% Crab no significant second component was found for the beta model. Again this changes with increasing flux. At a level 10% Crab and 30% Crab the source is modelled best with a small "core" component for the peak emission at the center and a second, larger "halo" component to account for the emission from the tails of the source. With a model flux of 100% Crab an additional a third component was found. But again the total excess is modelled quite well by the multiple Gaussian model.

The Disk model does not decompose on the 3% Crab level. At 10% Crab there are already four significant components and even six components for 30% Crab. It turned out that the

disk model, with very steep and well defined edges can only be badly modelled by the sum of a few smooth Gaussian components. No further effort was put into modelling the the disk morphology at 100% Crab, that is why the residual significance map shows large features.

Fixed flux, varying size

In the second part of the study the total flux of the modelled source was fixed to 10% Crab and the size (R_{80}) was varied between $R_{80} = 0.03°$, $0.1°$, $0.3°$ and $1.0°$. The index of the beta model was again assumed to be $\alpha = 2$ and the elongation of the Gaussian was again $\sigma_x/\sigma_y = 2$. The models were again fitted down to a TS threshold of $\Delta\mathrm{TS} = 25$. FigureA.4 shows the result.

At $R_{80} = 0.03°$, which is below the scale of the PSF, none of the models decomposes because the morphology information is smoothed out by the PSF and or hidden by the $0.02°$/Pixel sampling of the survey maps. The flux is mostly contained in the central pixel.

With increasing radius $R_{80} = 0.1°$ the models start to decompose. For the elongated Gaussian three significant components of similar size were obtained. The beta morphology is again modelled best with a small core and a larger halo component. The Disk morphology finally consist of four components.

At a size of $R_{80} = 0.3°$ the number of components is the same as for $R_{80} = 0.1°$, but the components increase in size. As the total integrated flux of the source models was kept constant, the surface brightness and significance decrease with larger size.

On the largest size scale $R_{80} = 1.0°$ only one Gaussian component is obtained for each of the models. This effect is due to the low surface brightness of the sources, where the morphology is statistically not defined well enough. Fitting a single Gaussian component does not leave any significant residuals. Anyhow one can see, that the size of the beta model is underestimated, because only the peak emission is significant. For the disk model the size is overestimated, because the Gaussian morphology assigns more emission to the larger tails, compared to the (real) disk type morphology.

Conclusion

For low surface brightness and small sizes sources do not decompose into several components. For larger surface brightness the sources decompose into components, where the number and distribution depends on the shape of the source. In terms of flat residuals almost any of the assumed real source morphology could be modelled well by the sum of Gaussian components. The sizes of beta shaped models are underestimated for low surface brightness, the size of disk shaped sources is overestimated for low surface brightness.

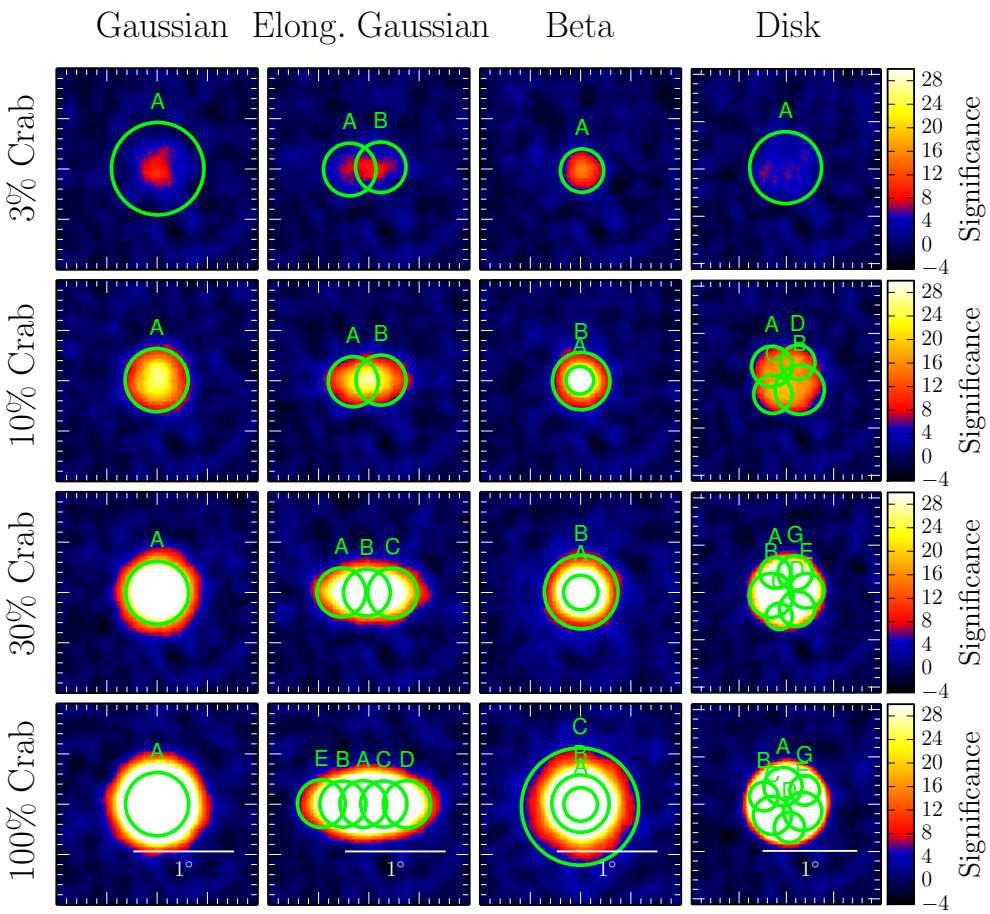

Figure A.2.: Decomposition of different source morphologies with varying flux: The total number and R_{80} of the fitted components are drawn as green circles. The Gaussian source model does not decompose on any flux scale.The elongated Gaussian model already decomposes for the smallest flux value of 3% Crab with $\Delta TS = 25.4$. At 30% Crab and 100% Crab a third and even a fourth and fifth component are found. The beta model decomposes at a level of 10% Crab and 30% into a core and a halo component. The disk model does not decompose on the 3% Crab level. At 10% Crab there are already four significant components and even six components for 30% Crab.

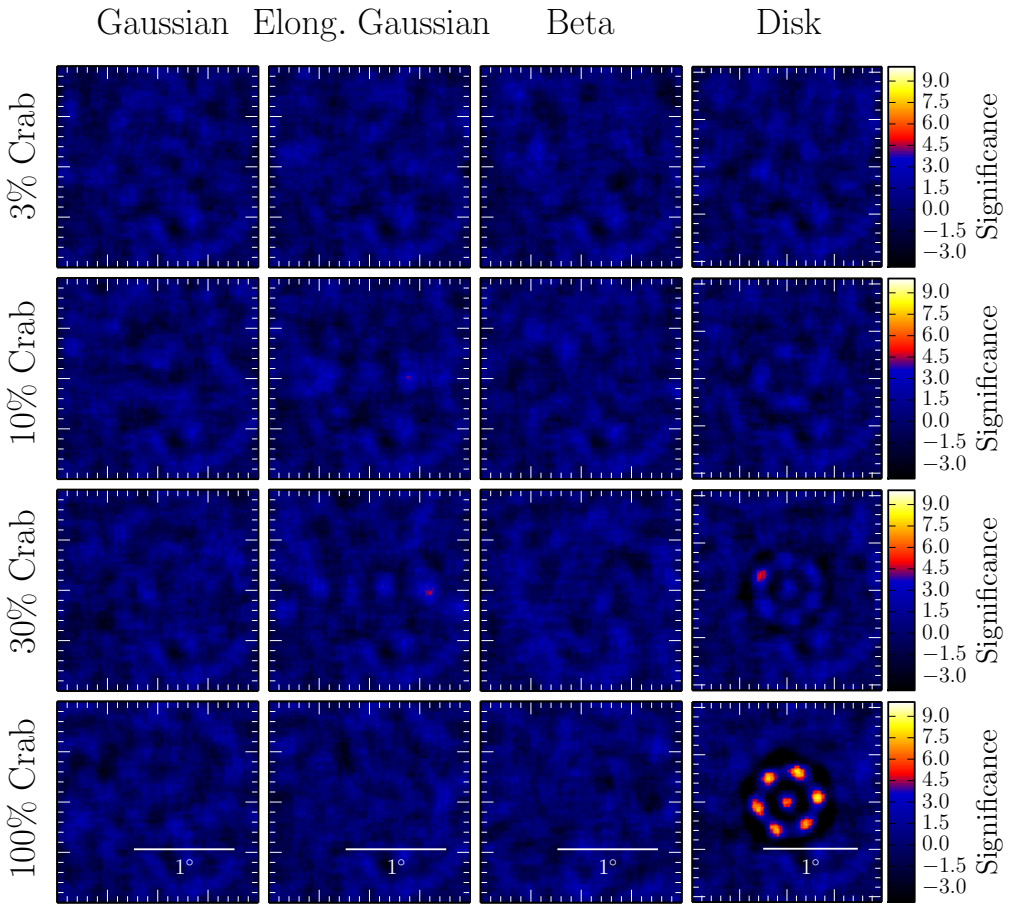

Figure A.3.: Residuals of different source morphologies with varying flux: Except for the disk model, all assumed source models could be modelled well enough by a sum of Gaussian components, that no significant residuals are left over. The disk model shows significant residuals at high fluxes, because of the steep edges of the disk. No further effort was put into modelling the disk morphology at 100% Crab.

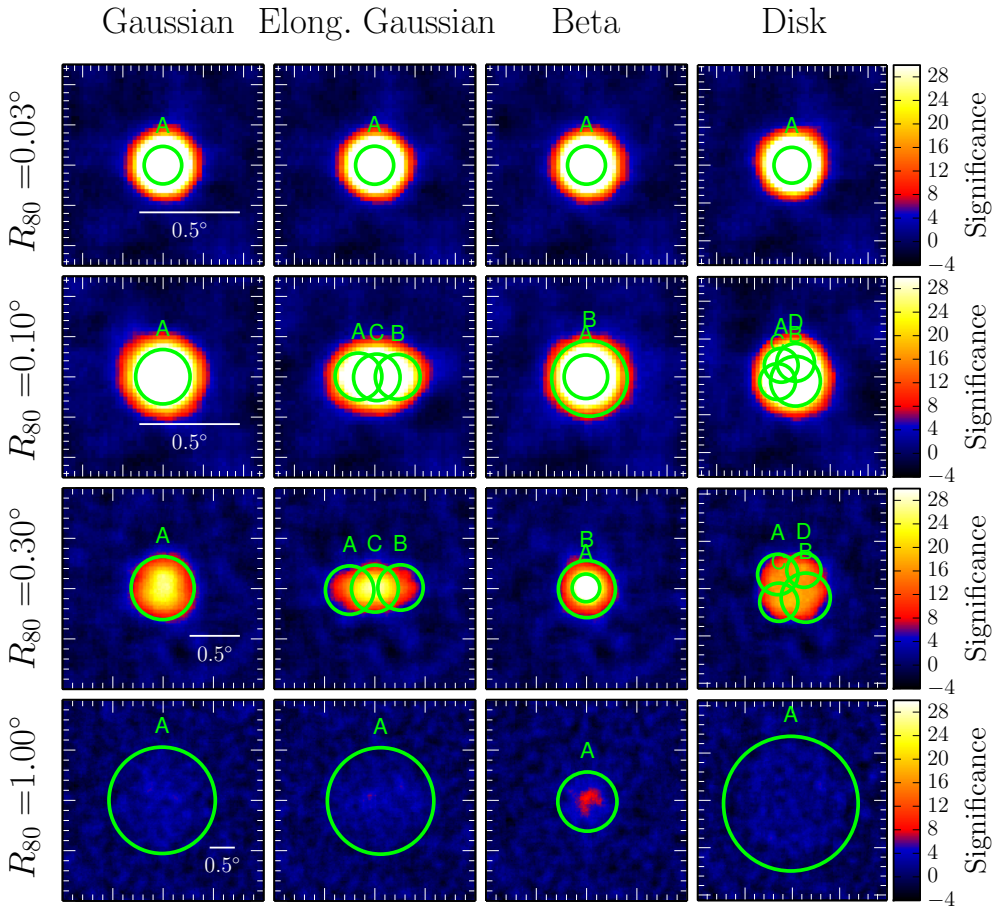

Figure A.4.: Decomposition of different source morphologies with varying size: At $R_{80} = 0.03°$, the scale of the PSF, none of the models decomposes because the morphology information is smoothed out by the PSF and or hidden by the 0.02°/Pixel sampling of the survey maps. For $R_{80} = 0.1°$ the models start to decompose. At a size of $R_{80} = 0.3°$ the number of components is the same as for $R_{80} = 0.1°$, but the components increase in size. On the largest size scale $R_{80} = 1.0°$ only one Gaussian component is obtained for each of the models. This effect is due to the low surface brightness of the sources, where the morphology is statistically not defined well enough. The size of the beta model is underestimated, because the emission is more peaked in the center. For the disk model the size is overestimated, because the Gaussian morphology assigns more emission to the tails, compared to the (real) disk type morphology.

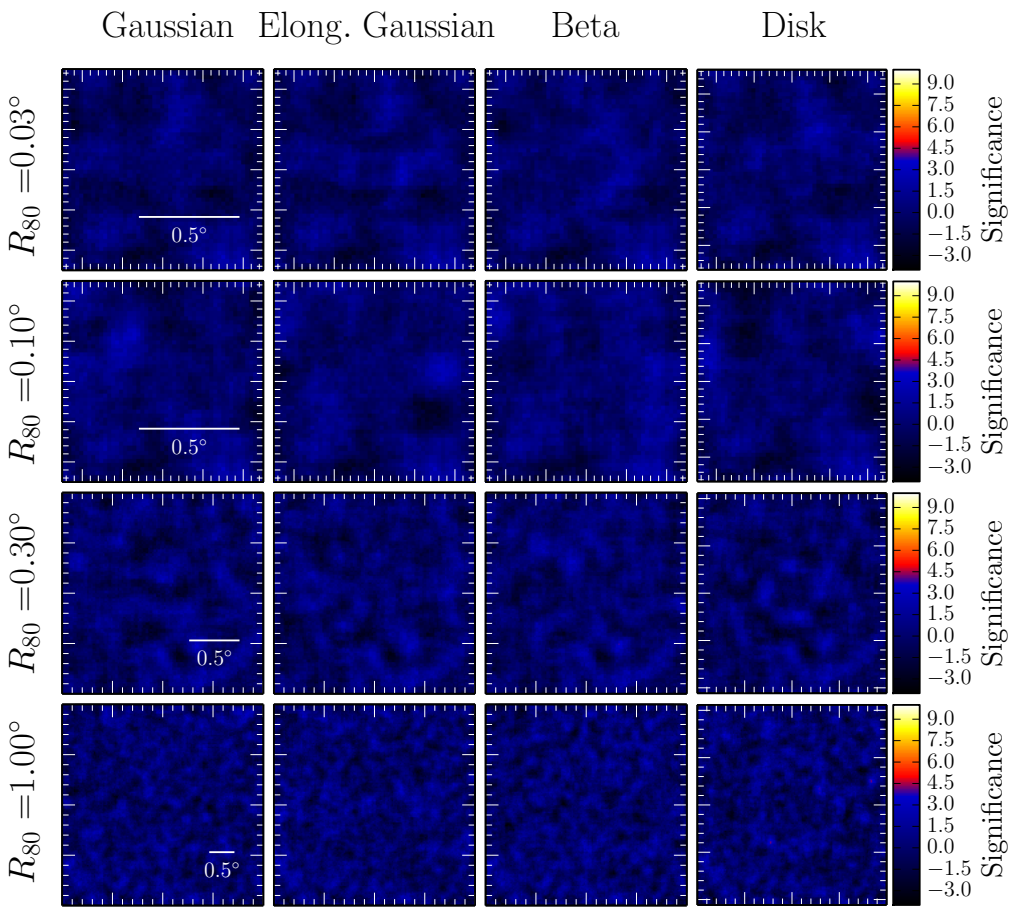

Figure A.5.: Residuals of different source morphologies with varying containment radius R_{80}: All assumed source models could be modelled well enough by a sum of Gaussian components, that no significant residuals are left over.

B. Analytical Solutions for Catalog Quantities assuming Gaussian Morphology

Computing Moments for Model Flux Distributions

In Chapter 5 source components are merged to sources. In case the spatial flux distribution is given by the sum of Gaussians, analytical solutions can be derived to compute the parameters of the merged source. The flux distribution is given by the sum of N Gaussian components, with each of them having the parameters F_i, σ_i, x_i and y_i:

$$f_\Sigma(x,y) = \sum_i^N F_i \frac{1}{2\pi\sigma^2} \exp\left(-\frac{(x-x_i)^2+(y-y_i)^2}{2\sigma_i^2}\right) \tag{B.1}$$

Total Flux As the Gaussian components are normalized the total flux is just given by the sum of the individual fluxes:

$$F_\Sigma = \sum_i^N F_i \tag{B.2}$$

Position The position is determined by weighting the single component positions with the corresponding flux. For the total x and y coordinates of the position we compute:

$$x_\Sigma = \frac{1}{F_\Sigma}\sum_i^N x_i F_i \qquad \text{and} \qquad y_\Sigma = \frac{1}{F_\Sigma}\sum_i^N y_i F_i \tag{B.3}$$

Extension The extension in x and y direction is obtained from the second moment of the sum of the components:

$$\sigma^2_{\Sigma_x} = \frac{1}{F_\Sigma}\sum_i^N F_i\cdot(\sigma_i^2+x_i^2) - x_\Sigma^2 \qquad \text{and} \qquad \sigma^2_{\Sigma_y} = \frac{1}{F_\Sigma}\sum_i^N F_i\cdot(\sigma_i^2+y_i^2) - y_\Sigma^2 \tag{B.4}$$

Where we additionally define the average circular extension by:

$$\sigma_\Sigma = \sqrt{\sigma_{\Sigma_x}\sigma_{\Sigma_y}} \tag{B.5}$$

Estimating Uncertainties

The analytical solution for flux, position and extension of the source can be used to also estimate uncertainties on this quantities. During the fit a covariance matrix is computed, which contains errors and correlation of all parameters of the components which are part of a certain solution. Given the formulae above, the variance on the merged quantities are given by:

$$V_\Sigma = J(x,y) \cdot V_{A\sigma xy} \cdot J^T(x,y) \tag{B.6}$$

Where J denotes the Jacobian matrix of the corresponding function for the merged quantity and $V_{A\sigma xy}$ the covariance of the involved component parameters.

Determining the Pairwise Q-factor

We assume two Gaussian sources with σ_A and σ_B, where the centers are displaced by $\vec{x}_{AB}$:

$$A(\vec{x}) = N_A \exp\left(-\frac{\vec{x}^2}{2\sigma_A^2}\right) \text{ and } B(\vec{x}) = N_B \exp\left(-\frac{(\vec{x}-\vec{x}_{AB})^2}{2\sigma_B^2}\right) \tag{B.7}$$

In the Q factor formula the term above the fraction line is technically a convolution of A and B evaluated at $\vec{x} = 0$. Convolution is most easily done in Fourier space. The FT of a Gaussian can be looked up[1]. Note that we have a 2D-transform where the pre factor is squared. After back transforming one obtains the result of the convolution:

$$A(\vec{x}) * B(\vec{x}) = \int A(\vec{x}')B(\vec{x}-\vec{x}')d^2x' = 2\pi N_A N_B \frac{\sigma_A^2\sigma_B^2}{\sigma_A^2+\sigma_B^2} \exp\left(-\frac{(\vec{x}-\vec{x}_{AB})^2}{2(\sigma_A^2+\sigma_B^2)}\right) \tag{B.8}$$

Now we have to evaluate the denominator which is a usual 2D Gaussian integral, which is also known[2].

$$\int A(\vec{x})^2 d^2x = N_A^2 \int \exp\left(-\frac{\vec{x}^2}{\sigma_A^2}\right) d^2x = \pi N_A^2 \sigma_A^2 \tag{B.9}$$

The same is obtained for B. Taking all together and setting $\vec{x} = 0$ we have for the Q-factor of two Gaussian source components the following expression, only depending on σ_A, σ_B and $\vec{x}_{AB}$:

$$\boxed{Q_{AB} = \frac{2\sigma_A\sigma_B}{\sigma_A^2+\sigma_B^2} \exp\left(-\frac{\vec{x}_{AB}^2}{2(\sigma_A^2+\sigma_B^2)}\right)} \tag{B.10}$$

[1] `http://mathworld.wolfram.com/FourierTransformGaussian.html`
[2] `http://mathworld.wolfram.com/GaussianIntegral.html`

C. Survey Maps

FITS Header

The following specification in the *FITS*-Header were used for all survey maps:

```
XTENSION= 'IMAGE   '           / IMAGE extension
BITPIX  =                   -32 / number of bits per data pixel
NAXIS   =                     2 / number of data axes
NAXIS1  =                  9400 / length of data axis 1
NAXIS2  =                   500 / length of data axis 2
PCOUNT  =                     0 / required keyword; must = 0
GCOUNT  =                     1 / required keyword; must = 1
EXTNAME = 'ExpGammaMap'
HDUNAME = 'ExpGammaMap'
CTYPE1  = 'GLON-CAR'           / Type of co-ordinate on axis 1
CTYPE2  = 'GLAT-CAR'           / Type of co-ordinate on axis 2
EQUINOX =                2000. / [yr] Epoch of reference equinox
CRPIX1  =                4700. / Reference pixel on axis 1
CRPIX2  =     250.500000465662 / Reference pixel on axis 2
CRVAL1  =     341.010000228882 / Value at ref. pixel on axis 1
CRVAL2  =                   0. / Value at ref. pixel on axis 2
CDELT1  =  -0.0199966430664062 / Pixel size on axis 1
CDELT2  =   0.0199999809265146 / Pixel size on axis 2
CUNIT1  = 'deg     '           / units of  CRVAL1 and  CDELT1
CUNIT2  = 'deg     '           / units of  CRVAL2 and  CDELT2
BUNIT   = 'Count   '
BSCALE  =                   1.
BZERO   =                   0.
TELESCOP= 'H.E.S.S.'           / name of telescope
ORIGIN  = 'The H.E.S.S. Collaboration' / organization responsible for the data
CREATOR = 'HESS Plotters::FITSTools $Revision: 1.30 $' / software configuration
OBJECT  = 'ra252.651304 dec-44.480656' / name of observed object
DATE    = '2013-10-17T22:32:12' / file creation date (YYYY-MM-DDThh:mm:ss UT)
HISTORY Created by klages with FITSTools.C $Revision: 1.30 $  on 2013-10-17T22:3
END
```

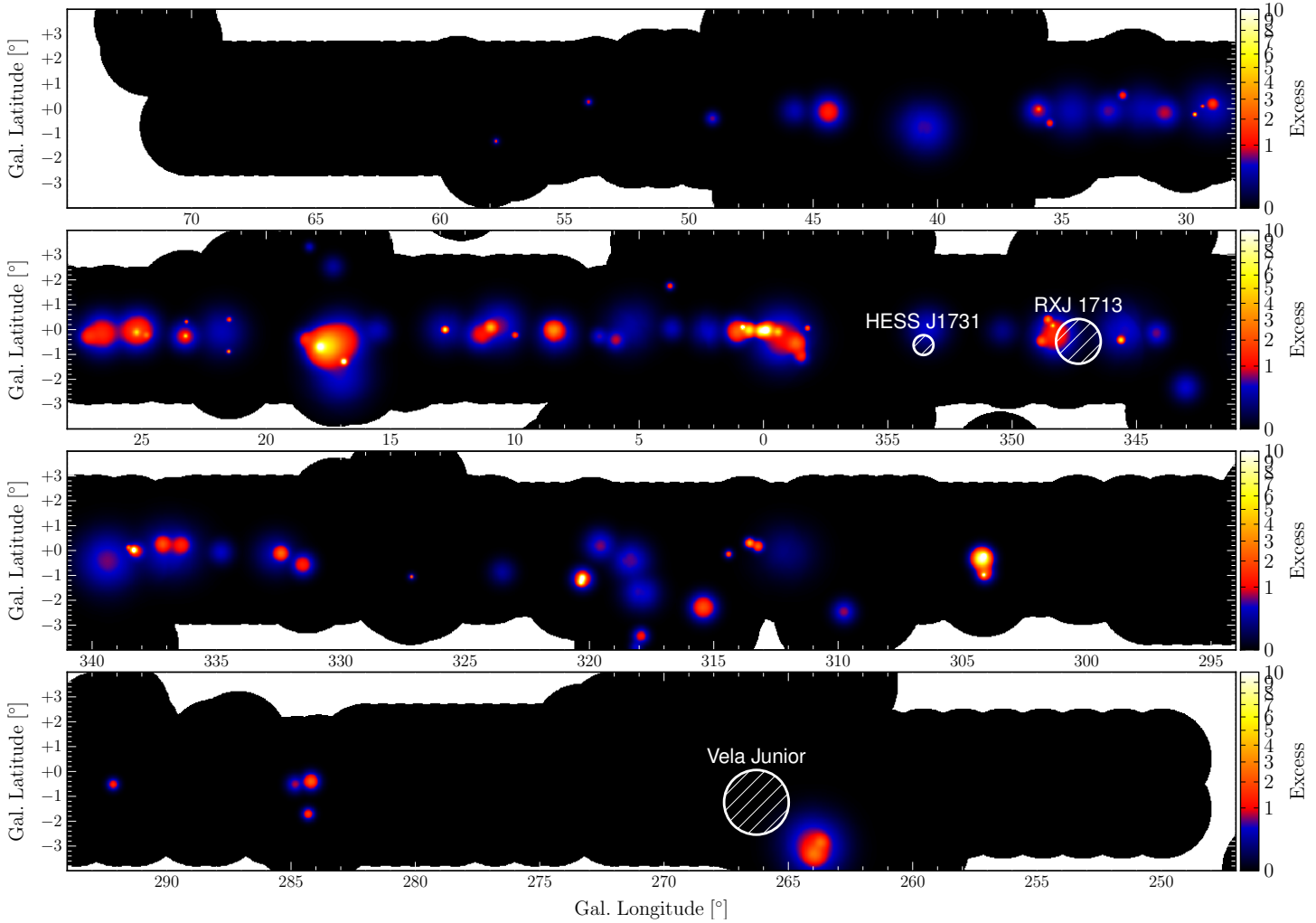

Figure C.1.: Survey model excess map

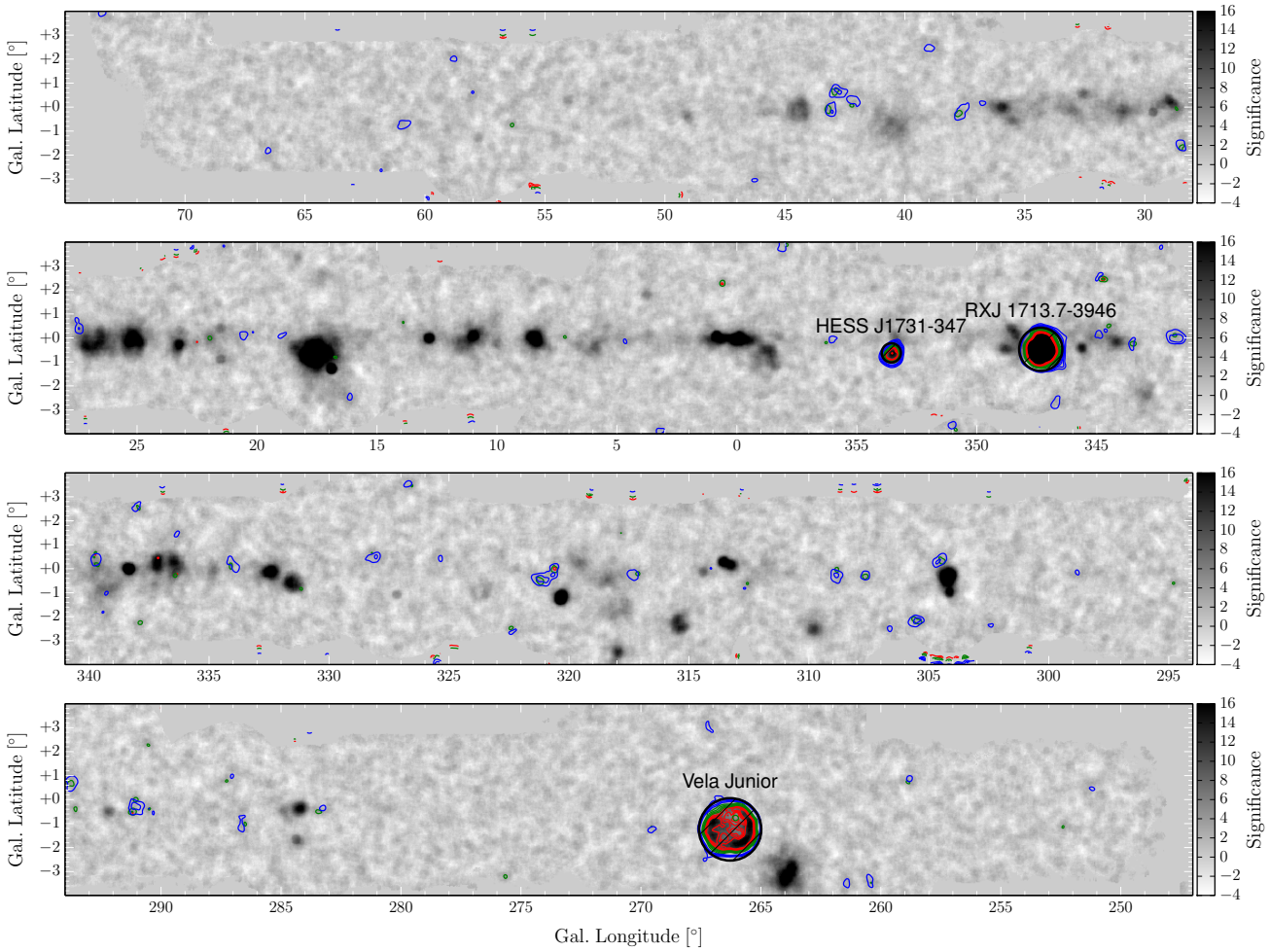

Figure C.2.: Survey residual significance contours plotted on top of a survey significance map with 0.2° correlation radius. The contours are shown for the 3σ, 4σ, 5σ and 6σ level. The colors correspond to the three different correlation radii 0.1° (red), 0.2° (green) and 0.4° (blue).

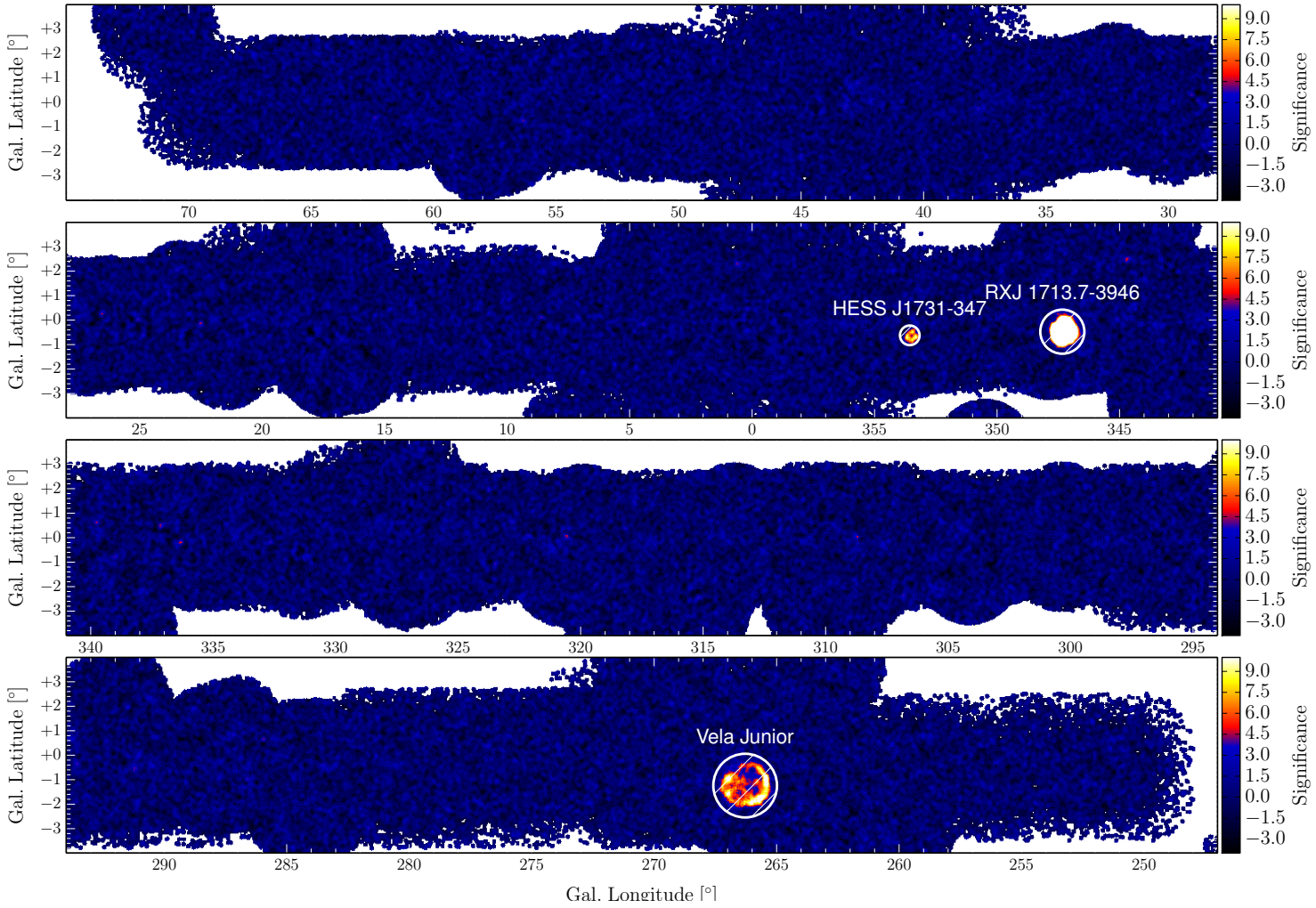

Figure C.3.: Survey map: residual significance with 0.1° correlation radius.

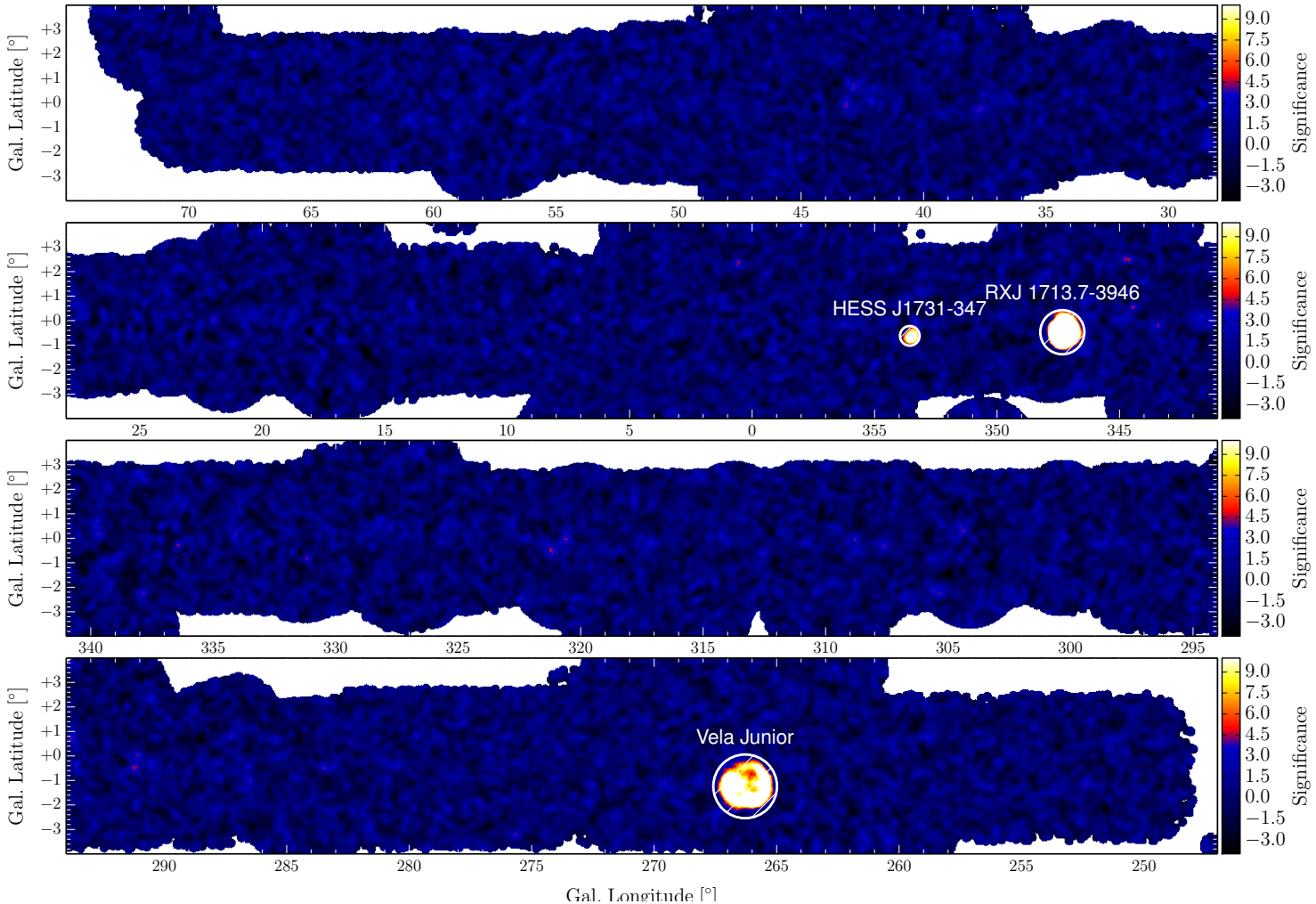

Figure C.4.: Survey map: residual significance map 0.2° correlation radius.

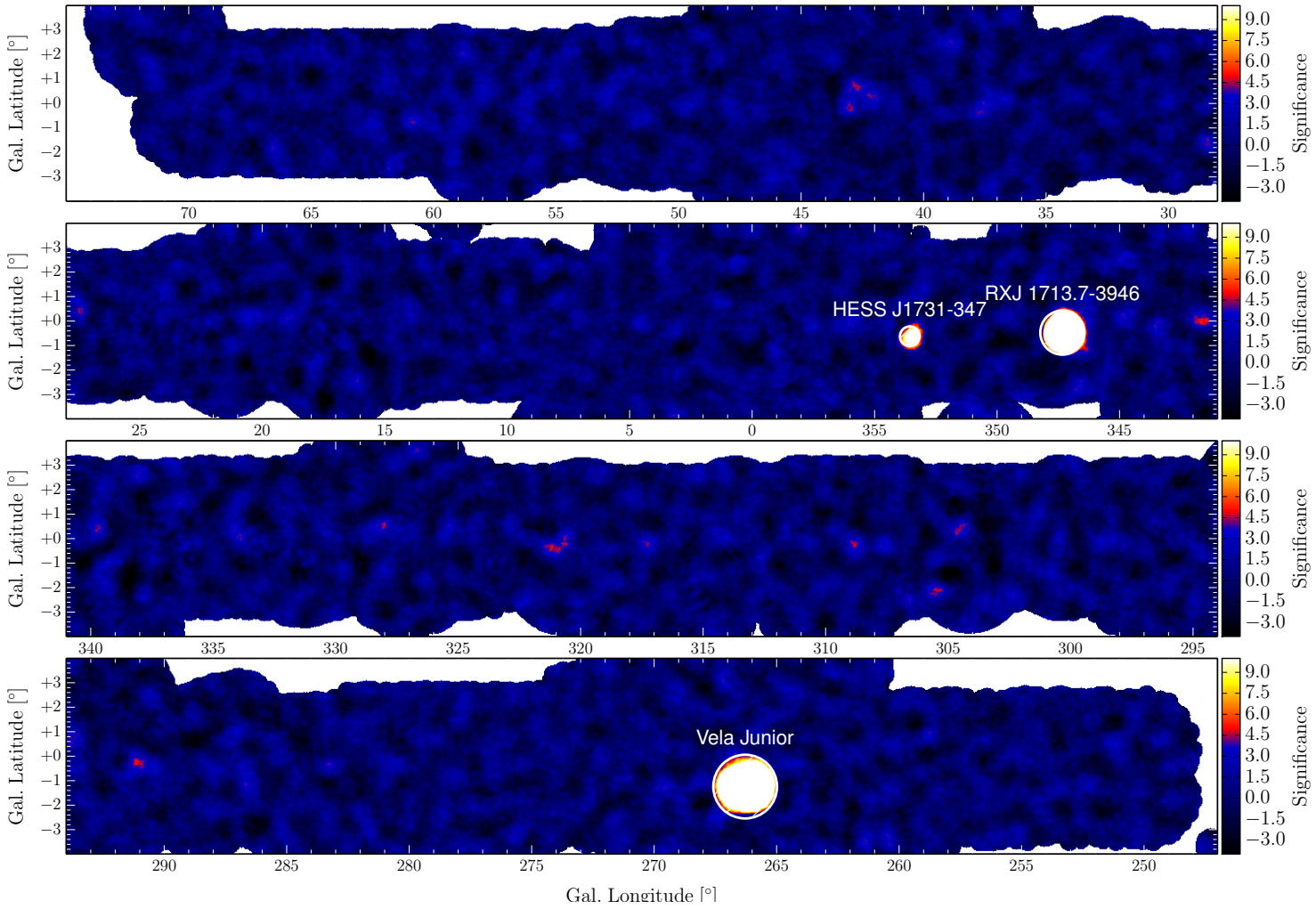

Figure C.5.: Survey map: residual significance with 0.4° correlation radius.

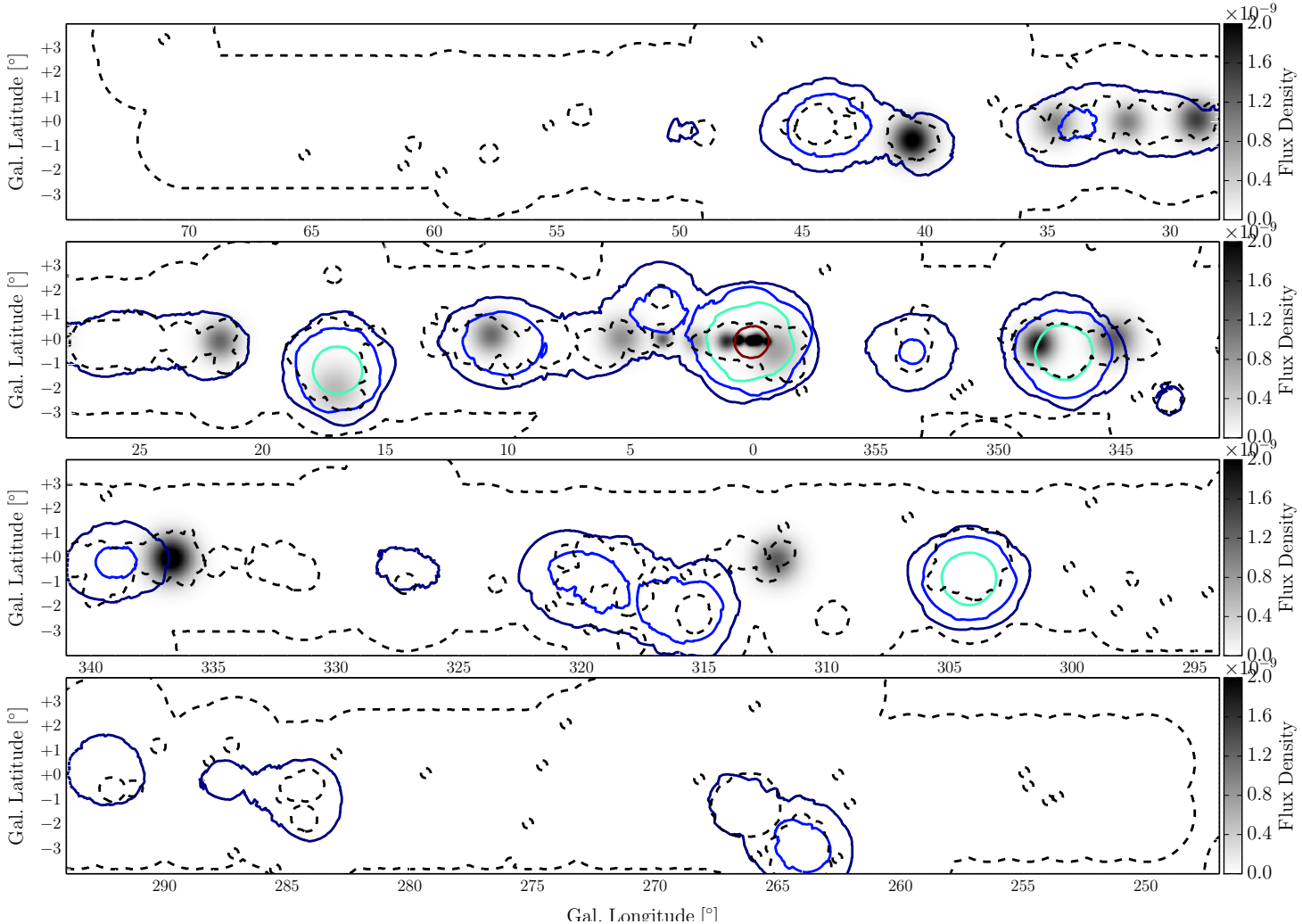

Figure C.6.: Model flux image of the components classified as unresolved by cuts in size and significance. The white dashed line indicates the boundaries of the exclusion regions. Contours of the exposure are drawn at a level of 2, 4, 8, and 16 · 10^{10} m^{-2} s^{-1} TeV^{-1}. The unit of the flux is ph m^{-2} s^{-1} TeV^{-1}.

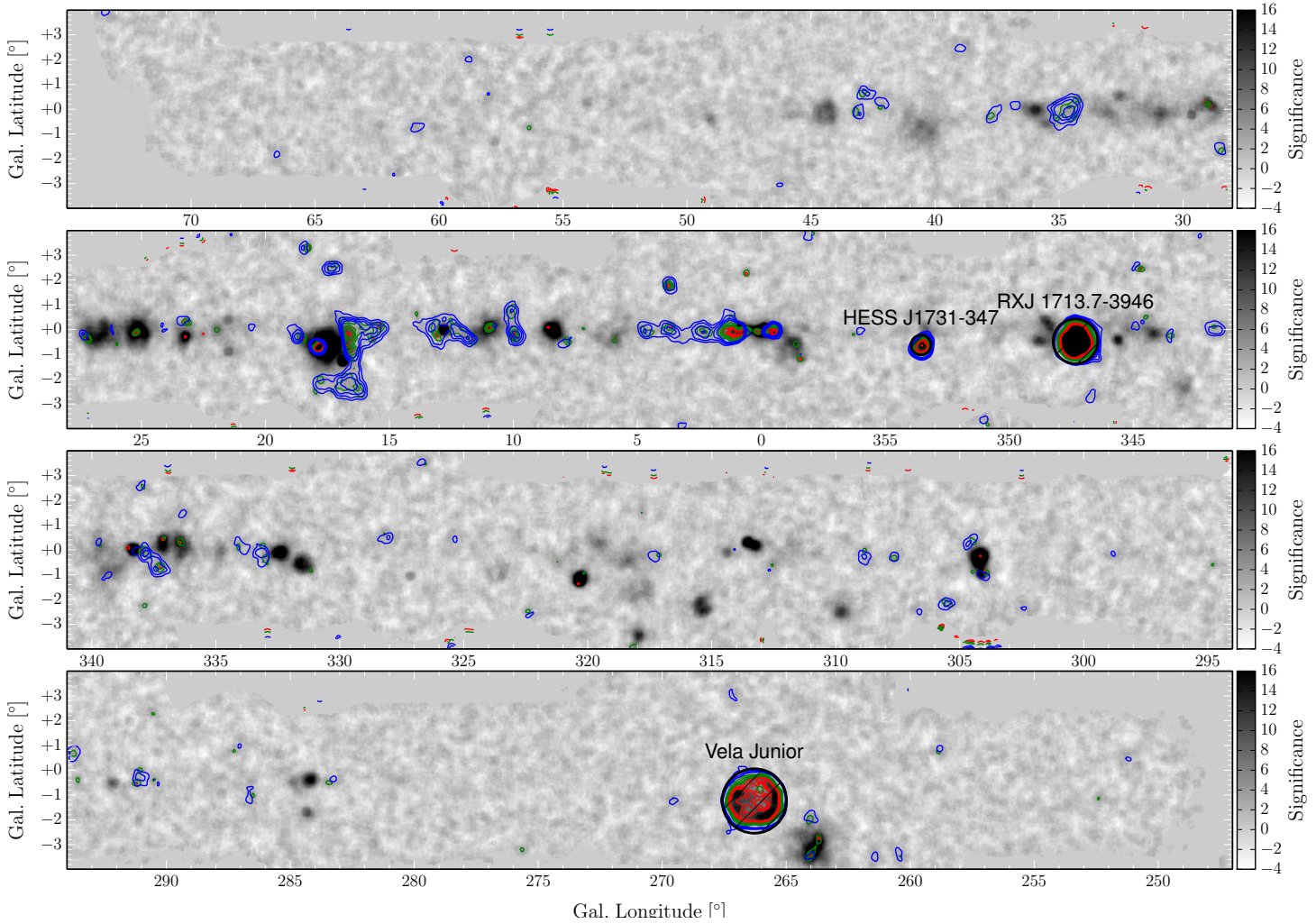

Figure C.7.: Survey residual significance contours for the *Q-forbid* method drawn on a survey significance map with 0.2° correlation radius. $Q_{Th} = 30\%$ was assumed. The contours are shown for the 3σ, 4σ, 5σ and 6σ level. The colors correspond to the three different correlation radii 0.1° (red), 0.2° (green) and 0.4° (blue).

D. Catalog Tables

ROI Name	l_{Min} [°]	l_{Max} [°]	Area [(°)^2]	PSF_{68} [°]	PSF_{95} [°]	Max.$\sigma_{0.1}$	Max.$\sigma_{0.2}$	Max.$\sigma_{0.4}$
GLON_000.5	355.0	6.0	95	0.070	0.173	3.7	4.0	4.3
GLON_008.5	2.0	15.0	112	0.068	0.172	4.3	5.0	6.8
GLON_017.5	13.0	22.0	74	0.069	0.176	3.7	3.3	4.2
GLON_022	19.0	25.0	53	0.071	0.187	4.1	4.1	7.0
GLON_026	23.0	29.0	49	0.072	0.193	4.3	4.0	7.0
GLON_033	28.0	38.0	90	0.072	0.198	4.1	4.4	4.7
GLON_042.7	38.5	47.0	76	0.073	0.203	3.2	3.7	4.4
GLON_055	47.0	63.0	144	0.074	0.207	3.1	2.5	3.1
GLON_265	257.0	273.0	139	0.072	0.185	3.5	3.1	2.8
GLON_285	282.0	288.0	54	0.078	0.216	3.5	3.2	3.3
GLON_292	289.0	295.0	54	0.079	0.219	3.7	4.0	3.1
GLON_304.5	300.5	308.5	72	0.087	0.241	3.7	3.6	3.4
GLON_312	307.0	317.0	90	0.083	0.231	3.6	3.8	3.6
GLON_319.5	315.0	324.0	77	0.081	0.217	3.1	3.8	3.7
GLON_326	322.0	330.0	72	0.075	0.201	4.1	4.3	3.6
GLON_336	329.0	343.0	125	0.076	0.199	4.7	4.9	4.5
GLON_346.5	342.0	351.5	82	0.081	0.230	4.7	4.9	4.5
GLON_354	350.0	358.0	67	0.066	0.162	3.7	4.2	5.2

Table D.1.: Name, position and sizes of the 18 defined ROIs. The number in the ROI name denotes the position of the center of the ROI. All ROIs cover the latitude range of b= 5° to b= 5°. The column area lists the area of the pixels that are actually used in the fit. The last three columns show the maximal significance value on the 0.1°, 0.2° and 0.4° scale, within a stripe of width 0.1° from the boundary of the ROI.

ROI Name	E_{Real}	E_{Model}	E_{Model}/E_{Real}	B_{Real}	$Max.\ \mathcal{E}$	$N_{Gaussian}$	Max.$\sigma_{0.1}$	Max.$\sigma_{0.2}$	Max.$\sigma_{0.4}$
GLON_000.5	22558	22879	1.01	336434	1.78e+11	13	0.72	1.45	2.89
GLON_008.5	12390	12602	1.02	223965	9.47e+10	12	0.86	1.67	3.17
GLON_017.5	24818	25678	1.03	178394	9.99e+10	9	0.00	0.00	0.00
GLON_022	3553	3452	0.97	81582	4.53e+10	6	0.37	0.86	2.60
GLON_026	10259	10116	0.99	89201	3.53e+10	5	0.74	1.58	4.07
GLON_033	8603	8879	1.03	135387	4.52e+10	12	0.91	1.80	3.63
GLON_042.7	5132	5328	1.04	170684	6.55e+10	3	0.01	0.03	0.10
GLON_055	1416	371	0.26	136521	2.29e+10	3	0.00	0.00	0.00
GLON_265	8388	8716	1.04	167641	5.18e+10	3	0.61	1.25	2.94
GLON_285	1841	1983	1.08	98376	3.68e+10	3	0.00	0.00	0.00
GLON_292	273	338	1.24	85051	3.16e+10	1	0.00	0.00	0.00
GLON_304.5	8247	8906	1.08	226397	1.02e+11	4	0.00	0.00	0.00
GLON_312	5049	5176	1.03	184297	6.03e+10	6	0.00	0.00	0.00
GLON_319.5	7939	8139	1.03	238399	6.03e+10	9	0.05	0.22	1.79
GLON_326	-52	378	-7.21	86409	3.66e+10	2	0.00	0.00	0.00
GLON_336	13239	13865	1.05	173894	4.43e+10	11	0.00	0.00	0.00
GLON_346.5	8241	8370	1.02	260726	1.05e+11	9	0.05	0.11	0.43
GLON_354	1206	1138	0.94	99732	8.55e+10	1	0.04	0.10	0.31

Table D.2.: The table lists the ratio of the modelled and real excess in every ROI. The last three columns of the table show the maximal significance of the model significance maps in a stripe of width 0.1° from the ROI boundary on the 0.1°, 0.2° and 0.4° scale.

Table D.3.: Manual classification and H.E.S.S. source associations of source components. The classification and association to known H.E.S.S. was carried out by Vincent Marandon.

#	Component Name	l [°]	b [°]	σ [°]	F [%Crab]	$\sqrt{TS}$	Classification	H.E.S.S. Name
1	HGPSC J1754.2-2545.2	3.711	-0.006	0.234	3.343	6.4	unresolved	-
2	HGPSC J1751.5-2657.6	2.364	-0.099	0.335	4.258	7.3	unresolved	-
3	HGPSC J1747.3-2809.4	0.864	0.077	0.012	1.789	29.5		HESS J1747-281
4	HGPSC J1745.6-2900.5	359.943	-0.046	0.020	6.454	75.8		HESS J1745-290
5	HGPSC J1745.4-2904.2	359.866	-0.040	0.144	4.055	21.5	unresolved	-
6	HGPSC J1747.2-2826.5	0.602	-0.040	0.129	3.230	22.6	unresolved	-
7	HGPSC J1746.2-2851.0	0.146	-0.076	0.115	3.237	23.4	unresolved	-
8	HGPSC J1745.1-2954.8	359.115	-0.428	0.644	14.619	19.6	unresolved	-
9	HGPSC J1748.6-2801.8	1.115	-0.092	0.258	5.647	19.6	unresolved	-
10	HGPSC J1744.7-2927.9	359.445	-0.107	0.096	1.368	11.8	unresolved	-
11	HGPSC J1741.2-3023.8	358.255	0.044	0.047	0.659	5.9		HESS J1741-302
12	HGPSC J1746.3-3049.4	358.474	-1.123	0.158	2.500	8.6		HESS J1745-303
13	HGPSC J1744.7-3022.7	358.671	-0.591	0.200	4.025	13.8		HESS J1745-303
14	HGPSC J1813.5-1750.3	12.812	-0.026	0.049	7.975	27.4		HESS J1813-178
15	HGPSC J1813.7-1744.8	12.905	-0.004	0.412	14.960	11.7		HESS J1813-178
16	HGPSC J1809.5-1924.0	10.977	0.071	0.117	4.791	20.1		HESS J1809-193
17	HGPSC J1811.6-1907.6	11.464	-0.245	0.316	10.374	17.8		-
18	HGPSC J1808.5-1936.6	10.685	0.166	0.499	13.704	17.1	unresolved	-
19	HGPSC J1808.6-2024.5	9.999	-0.244	0.063	0.840	6.9		HESS J1808-204
20	HGPSC J1804.5-2139.9	8.434	-0.018	0.193	14.858	30.3		HESS J1804-216
21	HGPSC J1801.7-2323.0	6.616	-0.297	0.174	2.567	6.5		HESS J1801-233
22	HGPSC J1800.8-2402.0	5.954	-0.446	0.215	5.805	10.9		HESS J1800-240
23	HGPSC J1804.8-2152.1	8.292	-0.180	0.387	14.697	16.2		HESS J1804-216
24	HGPSC J1757.7-2417.4	5.376	0.044	0.530	11.623	9.7	unresolved	-
25	HGPSC J1747.8-2449.1	3.776	1.715	0.061	1.139	8.1		HESS J1747-248
26	HGPSC J1822.9-1419.8	16.964	-0.339	0.535	25.104	29.7		HESS J1825-137
27	HGPSC J1825.9-1344.1	17.832	-0.706	0.111	6.411	24.2		HESS J1825-137
28	HGPSC J1825.9-1259.5	18.491	-0.360	0.181	4.453	10.5		-

#	Component Name	l [°]	b [°]	σ [°]	F [%Crab]	$\sqrt{TS}$	Classification	H.E.S.S. Name
29	HGPSC J1829.2-1503.0	17.044	-2.034	0.665	11.576	12.4	unresolved	-
30	HGPSC J1826.2-1451.1	16.876	-1.288	0.008	5.179	58.3		HESS J1826-148
31	HGPSC J1825.4-1350.0	17.692	-0.653	0.407	48.658	69.6		HESS J1825-137
32	HGPSC J1812.3-1128.4	18.262	3.280	0.085	2.602	5.7		-
33	HGPSC J1818.7-1527.9	15.485	0.023	0.286	4.235	6.3		HESS J1818-155
34	HGPSC J1813.3-1241.5	17.303	2.490	0.213	4.183	6.1		HESS J1813-127
35	HGPSC J1834.5-0844.8	23.234	-0.274	0.032	2.125	11.1		HESS J1834-087
36	HGPSC J1832.4-0831.0	23.199	0.294	0.024	0.830	5.9		HESS J1832-084
37	HGPSC J1834.7-0843.7	23.269	-0.299	0.286	15.276	20.3		HESS J1834-087
38	HGPSC J1833.5-1034.7	21.495	-0.898	0.006	3.299	10.8		HESS J1833-105
39	HGPSC J1831.1-0959.9	21.728	-0.090	0.510	14.597	12.3	unresolved	-
40	HGPSC J1828.9-1000.0	21.481	0.381	0.038	1.395	8.0		HOTS J1829-100
41	HGPSC J1840.4-0541.8	26.615	-0.171	0.427	38.905	36.1		HESS J1841-055
42	HGPSC J1841.9-0515.9	27.168	-0.301	0.203	7.280	12.1		HESS J1841-055
43	HGPSC J1837.3-0657.2	25.143	-0.060	0.401	47.447	43.5		HESS J1837-069
44	HGPSC J1837.7-0656.0	25.201	-0.128	0.075	4.800	14.5		HESS J1837-069
45	HGPSC J1837.3-0720.3	24.803	-0.239	0.067	1.831	6.8		-
46	HGPSC J1857.3+0245.1	36.058	-0.062	0.302	16.561	17.7		HESS J1857+026
47	HGPSC J1857.0+0242.0	35.979	-0.025	0.033	1.405	6.5		HESS J1857+026
48	HGPSC J1858.2+0202.7	35.530	-0.582	0.080	2.144	8.6		HESS J1858+020
49	HGPSC J1854.9+0132.5	34.708	-0.083	0.514	11.681	10.7	unresolved	-
50	HGPSC J1852.1+0008.2	33.136	-0.096	0.327	7.734	12.0		HESS J1852-000
51	HGPSC J1848.9-0002.9	32.603	0.535	0.090	2.102	9.2		HESS J1849-000
52	HGPSC J1848.3-0154.5	30.879	-0.181	0.304	10.151	15.1		HESS J1848-018
53	HGPSC J1849.4-0101.1	31.799	-0.025	0.479	10.782	10.5	unresolved	-
54	HGPSC J1846.4-0258.6	29.708	-0.239	0.007	2.103	13.4		HESS J1846-023
55	HGPSC J1844.6-0306.2	29.398	0.089	0.011	0.812	6.3		HESS J1844-031
56	HGPSC J1843.5-0325.5	28.982	0.195	0.118	4.514	11.3		HESS J1843-033
57	HGPSC J1843.9-0328.8	28.982	0.075	0.543	21.357	14.6	unresolved	-
58	HGPSC J1915.6+1126.0	45.850	-0.091	0.283	4.030	6.0		-
59	HGPSC J1908.1+0625.9	40.557	-0.762	0.541	30.038	20.3		HESS J1908+063
60	HGPSC J1913.1+1010.8	44.456	-0.130	0.335	11.820	20.2		HESS J1912+101

#	Component Name	l [°]	b [°]	σ [°]	F [%Crab]	$\sqrt{TS}$	Classification	H.E.S.S. Name
61	HGPSC J1930.4+1849.7	54.048	0.266	0.052	1.625	6.1		HESS J1930+186
62	HGPSC J1922.9+1408.3	49.074	-0.394	0.127	3.315	7.6		HESS J1923+141
63	HGPSC J1943.9+2118.1	57.763	-1.301	0.027	1.251	5.9		HESS J1943+213
64	HGPSC J0835.8-4539.3	263.994	-2.998	0.647	44.597	32.5		HESS J0835-455
65	HGPSC J0834.2-4551.1	263.982	-3.344	0.236	10.665	19.4		HESS J0835-455
66	HGPSC J0835.7-4519.7	263.713	-2.828	0.156	4.168	11.2		HESS J0835-455
67	HGPSC J1018.5-5856.1	284.306	-1.708	0.112	3.855	11.9		HESS J1018-589
68	HGPSC J1023.2-5746.5	284.198	-0.397	0.168	10.512	22.6		HESS J1023-575
69	HGPSC J1026.9-5813.0	284.844	-0.513	0.165	3.693	8.2		HESS J1026-582
70	HGPSC J1119.1-6127.1	292.141	-0.528	0.105	3.717	10.7		HESS J1119-614
71	HGPSC J1302.3-6305.8	304.168	-0.253	0.050	1.988	11.6		HESS J1303-631
72	HGPSC J1303.1-6311.2	304.255	-0.346	0.196	20.589	56.9		HESS J1303-631
73	HGPSC J1302.8-6350.8	304.185	-1.003	0.008	1.769	16.6		HESS J1302-638
74	HGPSC J1302.4-6346.3	304.144	-0.927	0.179	3.452	11.2		HESS J1302-638
75	HGPSC J1442.8-6226.2	315.428	-2.301	0.258	12.713	24.0		HESS J1442-624
76	HGPSC J1428.0-6051.9	314.424	-0.169	0.052	3.108	11.0		HESS J1427-608
77	HGPSC J1420.3-6045.1	313.580	0.269	0.080	12.643	27.5		HESS J1420-607
78	HGPSC J1418.0-6059.1	313.243	0.140	0.110	11.865	21.9		HESS J1418-609
79	HGPSC J1409.5-6135.5	312.085	-0.118	0.572	20.136	8.5		HESS J1406-613 / HESS J1414-619
80	HGPSC J1355.8-6430.4	309.799	-2.498	0.230	21.372	17.3		HESS J1356-645
81	HGPSC J1513.6-5906.5	320.306	-1.122	0.056	7.901	28.3		HESS J1514-591
82	HGPSC J1513.7-5909.0	320.299	-1.167	0.207	9.755	15.7		HESS J1514-591
83	HGPSC J1514.6-5913.2	320.354	-1.283	0.054	7.460	26.8		HESS J1514-591
84	HGPSC J1503.5-5817.8	319.573	0.241	0.302	8.536	11.9		HESS J1503-582
85	HGPSC J1457.2-5926.0	318.321	-0.376	0.385	12.589	13.9		HESS J1457-593
86	HGPSC J1459.7-6047.5	317.954	-1.718	0.365	9.125	11.3		HESS J1459-608
87	HGPSC J1506.8-6218.3	317.961	-3.451	0.148	9.735	16.3		HESS J1507-622
88	HGPSC J1510.0-6235.6	318.139	-3.889	0.117	3.273	5.8		HESS J1507-622
89	HGPSC J1511.0-5759.4	320.587	0.013	0.058	0.986	5.6		HOTS J1511-579
90	HGPSC J1554.6-5505.3	327.158	-1.078	0.017	1.406	9.1		HESS J1554-550
91	HGPSC J1533.3-5710.5	323.537	-0.929	0.262	6.598	6.3		HESS J1534-571
92	HGPSC J1646.9-4601.2	339.412	-0.504	0.641	31.654	22.0		HESS J1646-458

#	Component Name	l [°]	b [°]	σ [°]	F [%Crab]	$\sqrt{TS}$	Classification	H.E.S.S. Name
93	HGPSC J1641.0-4618.7	338.517	0.084	0.039	1.135	7.4		HESS J1641-462
94	HGPSC J1640.6-4632.1	338.307	-0.016	0.045	8.927	40.6		HESS J1640-465
95	HGPSC J1640.3-4639.2	338.185	-0.058	0.174	4.350	9.0		HESS J1640-465
96	HGPSC J1634.9-4714.0	337.133	0.244	0.179	11.936	18.8		HESS J1634-472
97	HGPSC J1632.0-4749.2	336.374	0.200	0.217	14.788	16.6		HESS J1632-478
98	HGPSC J1634.5-4743.5	336.724	-0.038	0.602	40.377	19.4	unresolved	-
99	HGPSC J1626.8-4909.2	334.815	-0.095	0.245	8.953	9.7		HESS J1626-490
100	HGPSC J1616.4-5054.0	332.390	-0.143	0.161	20.653	27.7		HESS J1616-508
101	HGPSC J1617.6-5046.8	332.610	-0.188	0.422	18.988	11.5		HESS J1616-508
102	HGPSC J1614.4-5150.4	331.517	-0.609	0.230	27.857	29.0		HESS J1614-518
103	HGPSC J1721.1-3658.7	350.464	-0.078	0.298	6.302	6.1		-
104	HGPSC J1713.8-3812.9	348.620	0.386	0.070	1.934	10.2		HESS J1713-397
105	HGPSC J1715.7-3842.6	348.431	-0.199	0.451	18.667	20.8	unresolved	-
106	HGPSC J1714.2-3831.1	348.423	0.141	0.031	0.998	8.6		HESS J1714-385
107	HGPSC J1718.2-3830.0	348.887	-0.479	0.103	2.575	10.1		HESS J1718-385
108	HGPSC J1708.2-4104.2	345.681	-0.436	0.057	3.160	16.0		HESS J1708-410
109	HGPSC J1705.2-4104.7	345.331	0.015	0.560	19.225	13.0	unresolved	-
110	HGPSC J1702.4-4202.6	344.251	-0.162	0.243	21.220	17.7		HESS J1702-420
111	HGPSC J1708.0-4416.8	343.083	-2.322	0.278	8.882	11.0		HESS J1708-443
112	HGPSC J1728.6-3425.8	353.429	0.091	0.429	10.846	12.2		HESS J1729-345 / HOTS J1727-340

Table D.4.: Catalog based on the manual classification and merging of components. The given flux F is the differential flux at 1 TeV given in percent Crab. As reference Meyer, Horns and Zechlin, 2010 was used.

#	Source Name	l [°]	Δl [°]	b [°]	Δb [°]	σ [°]	$\Delta\sigma$ [°]	F [%Crab]	ΔF [%Crab]	$\sqrt{TS}$
1	HGPS J1747.3-2809.4	0.864	0.002	0.077	0.003	0.012	0.005	1.8	0.1	29.5
2	HGPS J1745.6-2900.5	359.943	0.001	-0.046	0.001	0.020	0.002	6.5	0.2	75.8
3	HGPS J1741.2-3023.8	358.255	0.023	0.044	0.015	0.047	0.019	0.7	0.2	5.9
4	HGPS J1745.3-3032.9	358.595	0.028	-0.795	0.036	0.257	0.034	6.5	1.0	16.3
5	HGPS J1813.6-1746.7	12.873	0.038	-0.012	0.031	0.335	0.097	22.9	2.1	29.8
6	HGPS J1809.5-1924.0	10.977	0.011	0.071	0.010	0.117	0.011	4.8	0.6	20.1
7	HGPS J1811.6-1907.6	11.464	0.045	-0.245	0.034	0.316	0.035	10.4	2.2	17.8
8	HGPS J1808.6-2024.5	9.999	0.021	-0.244	0.015	0.063	0.016	0.8	0.2	6.9
9	HGPS J1800.8-2402.0	5.954	0.035	-0.446	0.035	0.215	0.034	5.8	1.4	10.9
10	HGPS J1801.7-2323.0	6.616	0.046	-0.297	0.048	0.174	0.069	2.6	1.1	6.5
11	HGPS J1804.7-2145.9	8.363	0.019	-0.098	0.019	0.315	0.068	29.6	1.4	34.3
12	HGPS J1747.8-2449.1	3.776	0.015	1.715	0.015	0.061	0.012	1.1	0.2	8.1
13	HGPS J1824.7-1358.9	17.476	0.016	-0.559	0.013	0.508	0.029	80.2	2.3	79.4
14	HGPS J1825.9-1259.5	18.491	0.036	-0.360	0.032	0.181	0.032	4.5	1.1	10.5
15	HGPS J1826.2-1451.1	16.876	0.001	-1.288	0.003	0.008	0.002	5.2	0.4	58.3
16	HGPS J1812.3-1128.4	18.262	0.024	3.280	0.031	0.085	0.018	2.6	0.6	5.7
17	HGPS J1818.7-1527.9	15.485	0.078	0.023	0.064	0.286	0.047	4.2	1.0	6.3
18	HGPS J1813.3-1241.5	17.303	0.059	2.490	0.052	0.213	0.032	4.2	0.9	6.1
19	HGPS J1834.5-0844.8	23.234	0.008	-0.274	0.010	0.032	0.014	2.1	0.5	11.1
20	HGPS J1832.4-0831.0	23.199	0.015	0.294	0.010	0.024	0.012	0.8	0.2	5.9
21	HGPS J1834.7-0843.7	23.269	0.021	-0.299	0.024	0.286	0.026	15.3	1.3	20.3
22	HGPS J1833.5-1034.7	21.495	0.003	-0.898	0.002	0.006	0.002	3.3	4.4	10.8
23	HGPS J1828.9-1000.0	21.481	0.012	0.381	0.012	0.038	0.012	1.4	0.3	8.0
24	HGPS J1840.7-0537.7	26.702	0.021	-0.191	0.016	0.425	0.032	46.2	1.8	38.1
25	HGPS J1837.4-0657.1	25.149	0.015	-0.066	0.013	0.383	0.033	52.2	1.9	45.8
26	HGPS J1837.3-0720.3	24.803	0.016	-0.239	0.023	0.067	0.011	1.8	0.4	6.8
27	HGPS J1857.3+0244.9	36.052	0.031	-0.059	0.023	0.290	0.058	18.0	1.7	18.8
28	HGPS J1858.2+0202.7	35.530	0.022	-0.582	0.015	0.080	0.016	2.1	0.4	8.6

#	Source Name	l [°]	Δl [°]	b [°]	Δb [°]	σ [°]	$\Delta\sigma$ [°]	F [%Crab]	ΔF [%Crab]	$\sqrt{TS}$
29	HGPS J1852.1+0008.2	33.136	0.053	-0.096	0.042	0.327	0.035	7.7	1.2	12.0
30	HGPS J1848.9-0002.9	32.603	0.019	0.535	0.016	0.090	0.015	2.1	0.4	9.2
31	HGPS J1848.3-0154.5	30.879	0.042	-0.181	0.031	0.304	0.033	10.2	1.8	15.1
32	HGPS J1846.4-0258.6	29.708	0.005	-0.239	0.003	0.007	0.004	2.1	1.9	13.4
33	HGPS J1844.6-0306.2	29.398	0.009	0.089	0.011	0.011	nan	0.8	0.2	6.3
34	HGPS J1843.5-0325.5	28.982	0.023	0.195	0.020	0.118	0.014	4.5	0.8	11.3
35	HGPS J1915.6+1126.0	45.850	0.079	-0.091	0.072	0.283	0.047	4.0	1.0	6.0
36	HGPS J1908.1+0625.9	40.557	0.040	-0.762	0.040	0.541	0.029	30.0	2.2	20.3
37	HGPS J1913.1+1010.8	44.456	0.025	-0.130	0.025	0.335	0.016	11.8	0.8	20.2
38	HGPS J1930.4+1849.7	54.048	0.016	0.266	0.021	0.052	0.026	1.6	0.5	6.1
39	HGPS J1922.9+1408.3	49.074	0.026	-0.394	0.030	0.127	0.020	3.3	0.6	7.6
40	HGPS J1943.9+2118.1	57.763	0.012	-1.301	0.015	0.027	0.023	1.3	0.4	5.9
41	HGPS J0835.5-4540.1	263.972	0.023	-3.048	0.027	0.582	0.051	59.4	2.1	39.4
42	HGPS J1018.5-5856.1	284.306	0.017	-1.708	0.019	0.112	0.018	3.9	0.6	11.9
43	HGPS J1023.2-5746.5	284.198	0.015	-0.397	0.012	0.168	0.009	10.5	0.8	22.6
44	HGPS J1026.9-5813.0	284.844	0.045	-0.513	0.035	0.165	0.050	3.7	1.1	8.2
45	HGPS J1119.1-6127.1	292.141	0.019	-0.528	0.016	0.105	0.015	3.7	0.5	10.7
46	HGPS J1303.1-6310.8	304.247	0.005	-0.338	0.007	0.189	0.013	22.6	0.7	58.1
47	HGPS J1302.5-6347.8	304.157	0.020	-0.952	0.028	0.149	0.052	5.2	1.9	20.1
48	HGPS J1442.8-6226.2	315.428	0.016	-2.301	0.017	0.258	0.011	12.7	0.8	24.0
49	HGPS J1428.0-6051.9	314.424	0.010	-0.169	0.011	0.052	0.010	3.1	0.4	11.0
50	HGPS J1420.3-6045.1	313.580	0.007	0.269	0.007	0.080	0.006	12.6	1.0	27.5
51	HGPS J1418.0-6059.1	313.243	0.012	0.140	0.009	0.110	0.011	11.9	1.2	21.9
52	HGPS J1409.5-6135.5	312.085	0.130	-0.118	0.095	0.572	0.079	20.1	3.7	8.5
53	HGPS J1355.8-6430.4	309.799	0.022	-2.498	0.022	0.230	0.019	21.4	2.1	17.3
54	HGPS J1514.0-5909.5	320.317	0.007	-1.187	0.007	0.144	0.026	25.1	0.8	42.0
55	HGPS J1503.5-5817.8	319.573	0.038	0.241	0.040	0.302	0.033	8.5	1.2	11.9
56	HGPS J1457.2-5926.0	318.321	0.052	-0.376	0.039	0.385	0.043	12.6	1.7	13.9
57	HGPS J1459.7-6047.5	317.954	0.053	-1.718	0.047	0.365	0.030	9.1	1.1	11.3
58	HGPS J1506.8-6218.3	317.961	0.015	-3.451	0.017	0.148	0.013	9.7	1.0	16.3
59	HGPS J1510.0-6235.6	318.139	0.039	-3.889	0.036	0.117	0.022	3.3	0.8	5.8
60	HGPS J1511.0-5759.4	320.587	0.021	0.013	0.023	0.058	0.017	1.0	0.2	5.6

#	Source Name	l [°]	Δl [°]	b [°]	Δb [°]	σ [°]	$\Delta\sigma$ [°]	F [%Crab]	ΔF [%Crab]	$\sqrt{TS}$
61	HGPS J1554.6-5505.3	327.158	0.007	-1.078	0.008	0.017	0.009	1.4	0.2	9.1
62	HGPS J1533.3-5710.5	323.537	0.075	-0.929	0.061	0.262	0.042	6.6	1.5	6.3
63	HGPS J1646.9-4601.2	339.412	0.044	-0.504	0.049	0.641	0.031	31.7	2.3	22.0
64	HGPS J1641.0-4618.7	338.517	0.014	0.084	0.014	0.039	0.014	1.1	0.3	7.4
65	HGPS J1640.5-4634.4	338.267	0.014	-0.029	0.009	0.114	0.034	13.3	0.8	41.6
66	HGPS J1634.9-4714.0	337.133	0.015	0.244	0.019	0.179	0.013	11.9	1.5	18.8
67	HGPS J1632.0-4749.2	336.374	0.021	0.200	0.029	0.217	0.022	14.8	2.7	16.6
68	HGPS J1626.8-4909.2	334.815	0.038	-0.095	0.041	0.245	0.044	9.0	1.8	9.7
69	HGPS J1616.9-5050.6	332.496	0.040	-0.164	0.023	0.324	0.082	39.6	2.7	30.0
70	HGPS J1614.4-5150.4	331.517	0.015	-0.609	0.013	0.230	0.009	27.9	1.6	29.0
71	HGPS J1721.1-3658.7	350.464	0.090	-0.078	0.077	0.298	0.040	6.3	1.3	6.1
72	HGPS J1713.8-3812.9	348.620	0.014	0.386	0.013	0.070	0.015	1.9	0.4	10.2
73	HGPS J1714.2-3831.1	348.423	0.011	0.141	0.009	0.031	0.010	1.0	0.2	8.6
74	HGPS J1718.2-3830.0	348.887	0.022	-0.479	0.016	0.103	0.015	2.6	0.5	10.1
75	HGPS J1708.2-4104.2	345.681	0.008	-0.436	0.007	0.057	0.006	3.2	0.3	16.0
76	HGPS J1702.4-4202.6	344.251	0.025	-0.162	0.021	0.243	0.024	21.2	2.5	17.7
77	HGPS J1708.0-4416.8	343.083	0.038	-2.322	0.042	0.278	0.031	8.9	1.3	11.0
78	HGPS J1728.6-3425.8	353.429	0.057	0.091	0.069	0.429	0.060	10.8	1.9	12.2

Bibliography

[1] F. Aharonian et al. "Detection of very high energy radiation from HESS J1908+063 confirms the Milagro unidentified source MGRO J1908+06". In: *aap* 499 (June 2009), pp. 723–728. DOI: 10.1051/0004-6361/200811357. arXiv:0904.3409 [astro-ph.HE].

[2] F. Aharonian et al. "The H.E.S.S. Survey of the Inner Galaxy in Very High Energy Gamma Rays". In: *apj* 636 (Jan. 2006), pp. 777–797. DOI: 10.1086/498013. eprint: astro-ph/0510397.

[3] Astropy Collaboration et al. "Astropy: A community Python package for astronomy". In: *aap* 558, A33 (Oct. 2013), A33. DOI: 10.1051/0004-6361/201322068. arXiv:1307.6212 [astro-ph.IM].

[4] D. Berge, S. Funk and J. Hinton. "Background modelling in very-high-energy γ-ray astronomy". In: *aap* 466 (May 2007), pp. 1219–1229. DOI: 10.1051/0004-6361:20066674. eprint: astro-ph/0610959.

[5] E. Bertin and S. Arnouts. "SExtractor: Software for source extraction." In: *aaps* 117 (June 1996), pp. 393–404.

[6] C. Deil. "HESS and Fermi Surveys of the Galactic Gamma-ray source population". PhD thesis. Universität Heidelberg, Dec. 2011.

[7] S. Carrigan et al. "The H.E.S.S. Galactic Plane Survey - maps, source catalog and source population". In: *ArXiv e-prints* (July 2013). arXiv:1307.4690 [astro-ph.HE].

[8] W. Cash. "Parameter estimation in astronomy through application of the likelihood ratio". In: *apj* 228 (Mar. 1979), pp. 939–947. DOI: 10.1086/156922.

[9] K. Egberts et al. *Diffuse TeV Gamma-Ray Emission in the H.E.S.S. Galactic Plane Survey*. 2013. eprint: arXiv:1308.0161.

[10] P. Freeman et al. *Sherpa: CIAO Modeling and Fitting Package*. Astrophysics Source Code Library. July 2011. ascl: 1107.005.

[11] P. E. Freeman et al. "A Wavelet-Based Algorithm for the Spatial Analysis of Poisson Data". In: *apjs* 138 (Jan. 2002), pp. 185–218. DOI: 10.1086/324017. eprint: astro-ph/0108429.

[12] T.-P. Li and Y.-Q. Ma. "Analysis methods for results in gamma-ray astronomy". In: *apj* 272 (Sept. 1983), pp. 317–324. DOI: 10.1086/161295.

[13] M. Meyer, D. Horns and H.-S. Zechlin. "The Crab Nebula as a standard candle in very high-energy astrophysics". In: *aap* 523, A2 (Nov. 2010), A2. DOI: 10.1051/0004-6361/201014108. arXiv:1008.4524 [astro-ph.HE].

[14] T. C. Weekes et al. “Observation of TeV gamma rays from the Crab nebula using the atmospheric Cerenkov imaging technique”. In: *apj* 342 (July 1989), pp. 379–395. DOI: 10.1086/167599.

Acknowledgements

I would first like to thank Prof. Werner Hofmann for giving me the opportunity to work on such an interesting and relevant project. His experimental physics tutorial I attended in the first and second semester were a great inspiration and motivation for the subsequent years of my studies.

Especially I would like to thank Christoph Deil for the supervision of this thesis, for many interesting and fruitful discussions. His numerous ideas and critical comments greatly improved the quality of the work presented in this thesis. Additionally I would like to thank him for many instructive lessons in proper Python software development and the effort he put into carefully proofreading and commenting this thesis in the last few weeks.

I would also like to thank Vincent Marandon for his expert knowledge on many Galactic gamma-ray sources and for creating the manual reference catalog.

I would like to thank Svenja Carrigan and Francois Brun for the production and carefully checking of the survey maps, on which the analysis in this thesis was based on.

Furthermore I would like to thank Ellis Owen for proofreading.

I would like to thank the whole H.E.S.S. working group at the MPIK for a very pleasant working atmosphere, especially my office mates Quirin Weitzel and Alison Mitchell. I would also like to thank Ruth Crespo for her support in administrative issues.

Finally I would like to thank Anna for her moral support and inspiration. I would have never managed to finish such a "Rambo-Project" without her. I would also like to thank my parents and sister for encouraging and supporting me throughout my whole studies. Many thanks also go to Jonas, Marcel, Freya and Max for many memorable and future hiking, climbing, cooking, biking, handicraft and physics adventures.

This research made use of Astropy, a community-developed core Python package for Astronomy (Astropy Collaboration et al., 2013).

Erklärung:

Hiermit versichere ich, dass ich diese Arbeit selbständig verfasst und keine anderen als die angegebenen Quellen und Hilfsmittel benutzt habe.

Heidelberg, den ....
(*Unterschrift*)